UNDERSTANDING STRUCTURE-PROPERTY RELATIONSHIPS IN CATALYSTS USING CLUSTER EXPANSIONS

by

Chenyang Li

A dissertation submitted to Johns Hopkins University in conformity with the requirements for the degree of Doctor of Philosophy

Baltimore, Maryland

October 2020

Abstract

Density functional theory (DFT) is widely used to predict the structures and properties of nanoparticles (up to about 3 nm wide), but its direct applications to nanocatalysts of experimentally relevant sizes can be prohibitively expensive. It has been demonstrated that this problem can be addressed through the use of cluster expansion models trained by DFT. In this dissertation, four projects of using cluster expansions to better understand structure-property relationships in catalysts, from 0D nanoparticles to 1D nanorods and 2D surfaces, are presented. In the first project, the predicted Pt-Cu nanoparticle structures are compared with experimental characterization. It is demonstrated that the best agreement is achieved by constructing a novel cluster expansion for alloy nanoparticles of varying shape and size that explicitly includes adsorbates, enabling the prediction of nanoparticle structures in an oxidizing environment. In the second project, a transition-state cluster expansion that explicitly includes a sublattice of sites is constructed to predict the activation energies and study atomic diffusion in Pt-Ni nanoparticles. This model is systematically improvable through the generation of training data to a point at which the prediction error is about half of that of commonly-used simpler models, with a comparable overall execution speed in kinetic Monte Carlo simulations. In the third project, a study of the CO_2 reduction reaction on Au nanorods is presented. Nanostructures with the 4H phase show enhanced activity and selectivity relative to fcc nanorods experimentally. Cluster expansions are used to predict the equilibrium structures of fcc and 4H nanorods and further DFT calculations and kinetic models are used to identify the catalytically active sites. The enhanced activity of

the 4H nanostructures is ascribed to their unique surface structures with undercoordinated sites, which may provide new design strategies for experimental research. Lastly, a study of the hydrogen evolution reaction on transition metal phosphides and Pt surfaces is presented. Cluster expansions are used to predict structures and energetics of adsorbed hydrogen as a function of temperature and applied potential, allowing for the determination of the potential-dependent activity of different sites while fully accounting for the coverage effect. The challenge of using a simple descriptor for catalytic activity is discussed.

Thesis Advisor: Prof. Tim Mueller

Thesis Committee:

- Prof. Jonah Erlebacher
- Prof. Chao Wang
- Prof. Paulette Clancy
- Prof. Thomas Kempa
- Prof. Tim Mueller

Acknowledgements

I would like to express my deepest gratitude to my advisor, Professor Tim Mueller. Without his unparalleled guidance and support, the achievements in the past five years would not have been made possible. I am very grateful to him for his trust in me taking charge of multiple projects and for his patience when I made mistakes.

I would like to extend my thanks to all the members of the Mueller group, especially to Dr. Liang Cao, Dr. Pandu Wisesa, Dr. Fenglin Yuan, Dr. Sukriti Manna, Dr. Shanping Liu, Dr. Tanmoy Chakraborty, Alberto Hernandez-Valle, Chuhong Wang, Yunzhe (Phil) Wang, Koutarou Aoyagi, Peter Lile, Thomas Nilson, Hao Gao, Wan Wan, Sam Norwood, and Abigail Park. My friends and collaborators at Johns Hopkins and other places are also greatly acknowledged. Moreover, I appreciate the assistance and help that I received from Jeanine Majewski and Ellen Libao, who are amazing staff members of the department.

My appreciation also goes to the thesis committee members, Prof. Jonah Erlebacher, Prof. Chao Wang, Prof. Paulette Clancy, Prof. Thomas Kempa, and Prof. Tim Mueller, for their time and willingness to serve, and for all their constructive feedback.

I would also like to acknowledge the funding that made this thesis possible, especially from the National Science Foundation (CHE-1437396 and DMR-140068) and the Office of Naval Research (ONR MURI N00014-15-1-2681 and N00014-16-1-2355).

Lastly and most importantly, I would like to thank my parents for their unconditional love and support, and my fiancée Flora for all her love and companion.

Table of Contents

List of Tables

List of Figures

1. Overview

This dissertation is divided into six chapters. The first chapter contains an overview of the dissertation. The second chapter contains a brief introduction and review of the cluster expansion method, which is the core methodology used in the following chapters. The rest of the chapters make up the bulk of this dissertation, with each chapter having a unique focus and problem to address.

The bulk research contains four projects of using cluster expansions to better understand structure-property relationships in catalysts, from 0D nanoparticles to 1D nanorods and 2D surfaces. Chapter 3 and 4 focus on developing methods, with model systems being Pt-based nanoparticles, which are promising electrocatalysts for oxygen reduction reaction (ORR). Previous works on cluster expansions of nanoparticles have either assumed the particle exists in vacuum, used very small particles of fixed size and shape, or estimated the effects of adsorbates by using correction terms. In Chapter 3, the above problem is addressed by developing a novel nanoparticle cluster expansion that explicitly includes surface adsorbate to study nanoparticles of varying size, shape, and composition, enabling direct comparisons with experimental characterizations. While the cluster expansion has become a valuable tool for studying atomic order and structure-property relationships in nanoalloys, it is rarely used for modeling diffusion. In Chapter 4, a transition-state cluster expansion model is developed for predicting activation energies for diffusion in nanoalloys by explicitly including sites representing saddle points on the potential energy surface. This approach allows for the calculation of activation energies using a single cluster expansion and is systematically improvable with additional training data.

Chapters 5 and 6 focus on understanding of structure-property-performance relationships in catalysts directly, with model systems being Au nanorods for the CO_2 reduction reaction (CRR) and transition metal phosphide and Pt surfaces for the hydrogen evolution reaction (HER). Cluster expansion models are used to predict surface structures and subsequently catalytic activities of the underlying systems, highlighting the key importance and need of predicting structures before calculating property values (e.g. catalytic activities).

This dissertation is of significance in that it demonstrates that the structure-property relationships can be better understood by constructing novel cluster expansion models, directly comparing with experimental characterizations, and further refining the models for the rational design of surfaces and nanoscale materials.

2. Cluster Expansion

Cluster expansions are generalized Ising models[1-2] that account for many-body interactions, and the general formalism of the configurational cluster expansions was developed by Sanchez *et al*.[2] Prior to this, Baal[3] studied the order-disorder transformation in an fcc binary alloy using the generalized Ising-type model. In the following years, cluster expansions have been successfully used to study a variety of bulk materials[3-26], surfaces and nanostructured materials.[24, 27-63] Recently, there has been particularly growing interest in understanding structure-property relationships in low-dimensional materials owing to the increase of computing power and advance in machine learning.

In this chapter the cluster expansion formalism is briefly reviewed as well as the current progress of implementing cluster expansions in materials research, with the focus on i) machine learning approach to fitting the cluster expansion and ii) application to surfaces and nanostructured materials.

2.1 Formalism of cluster expansion

Cluster expansions are generalized Ising models,[1-2] in which the magnetic spin variables for each site in an Ising model are replaced by "site" variables that represent the atomic species occupied at each site. For example for a binary A-B alloy, the occupancy of the j^{th} site can be represented by a site variable s_j, where $s_j = 1$ if species "A" is present, $s_j = -1$ if species "B" is present. Higher-order cluster expansions, usually for surfaces and nanoparticles where translational symmetry is lost in one or more dimensions as opposed

to bulk periodic lattices, contain "vacancy" as an extra species for the site variables. Figure 1 is a schematic of a ternary A-B-vacancy cluster expansion for an A-B alloy nanoparticle. In this case site variable (s_j) values of 0, 1, and 2 can be assigned to A, B, and vacancy, respectively. In the following sections the notations for the cluster expansion are adopted from the work by Mueller and Ceder.[2, 64]

For each of the site variable, an orthonormal single-site basis is defined, such that:[2, 64]

$$\frac{\sum_{s_j=0}^{N_j-1} \Theta_b(s_j)\Theta_{b'}(s_j)}{N_j} = \delta_{bb'}, \tag{1}$$

where s_j is the site variable for the j^{th} site, N_j is the number of values this variable may take, $\Theta_b(s_j)$ is the b^{th} basis function for that site, and $\delta_{bb'}$ is the Kronecker delta. The tensor product of all single-site bases produces a basis of "cluster functions", $\Phi_{\mathbf{b}}(\mathbf{s})$. Each cluster function can be defined by a vector $\mathbf{b}$,

$$\Phi_{\mathbf{b}}(\mathbf{s}) = \prod_j \Theta_{b_j}(s_j), \tag{2}$$

where $\mathbf{s}$ is the set of all site variables and b_j is the index of the basis function used at site j. A property such as formation energy of the material can be expressed as a linear expansion of cluster functions,

$$F(\mathbf{s}) = V_0 + \sum_{\mathbf{b}} V_{\mathbf{b}} \Phi_{\mathbf{b}}(\mathbf{s}), \tag{3}$$

where the unknown coefficients $V_{\mathbf{b}}$ are effective cluster interactions (ECI) and V_0 is a constant term representing the "empty" cluster. If all possible cluster functions are included

in the cluster expansion, the above equation is exact. However, in practice, the ECIs for clusters that contain a large number of sites or the sites that are far apart are usually negligible. Therefore, the cluster expansion can be truncated to a sum over finite numbers of clusters functions with little loss of accuracy.

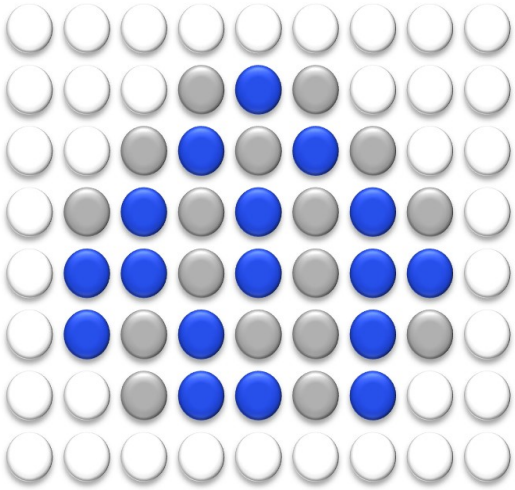

Figure 1. A schematic of how the structure of a binary A-B nanoparticle can be mapped to a lattice in a ternary A-B-vacancy cluster expansion. Gray, blue, and white spheres represent A, B, and vacancy, and site variables can be assigned 0, 1, and 2, respectively.

It is usually convenient to use $\Theta_0(s_j)=1$ for all s_j. For a binary cluster expansion, e.g. A-B bulk alloy, the following orthonormal basis is commonly used:

$$\begin{aligned}\Theta_0(s_j) &= 1,\\ \Theta_1(s_j) &= \cos(\pi s_j) = \pm 1.\end{aligned} \tag{4}$$

Thus, for a binary cluster expansion sometimes the notation of $s_j = \pm 1$ is used, and it becomes equivalent to express the product over s_j for equation (2). (This notation will be used particularly in Chapter 5 and 6).

For higher-order cluster expansions, a discrete cosine basis can be used to generate the cluster functions. For example a quaternary cluster expansion, in which the site variable values take 0, 1, 2, and 3, the b^{th} basis function is given by:

$$\Theta_b(s) = \begin{cases} 1, & b = 0 \\ \sqrt{2}\cos(\pi b(2s+1)/2n), & b > 0 \end{cases} \tag{5}$$

where n is the number of allowed values for the site variable s. Specifically,

$$\Theta_0(0) = \Theta_0(1) = \Theta_0(2) = \Theta_0(3) = 1, \tag{6}$$

$$\Theta_1(0) = \sqrt{2}\cos\frac{\pi}{8}, \Theta_1(1) = \sqrt{2}\cos\frac{3\pi}{8}, \Theta_1(2) = \sqrt{2}\cos\frac{5\pi}{8}, \Theta_1(3) = \sqrt{2}\cos\frac{7\pi}{8}, \tag{7}$$

$$\Theta_2(0) = \sqrt{2}\cos\frac{\pi}{4}, \Theta_2(1) = \sqrt{2}\cos\frac{3\pi}{4}, \Theta_2(2) = \sqrt{2}\cos\frac{5\pi}{4}, \Theta_2(3) = \sqrt{2}\cos\frac{7\pi}{4}, \tag{8}$$

$$\Theta_3(0) = \sqrt{2}\cos\frac{3\pi}{8}, \Theta_3(1) = \sqrt{2}\cos\frac{9\pi}{8}, \Theta_3(2) = \sqrt{2}\cos\frac{15\pi}{8}, \Theta_3(3) = \sqrt{2}\cos\frac{21\pi}{8}, \tag{9}$$

It is straightforward to show that equation (5) meets the orthonormal condition in equation (1). When $b = b' = 0,$ it is obvious that $\frac{1}{N_j}\sum_{s_j=0}^{N_j-1}\Theta_b(s_j)\Theta_{b'}(s_j) = 1.$ When $b \neq 0$ and $b' = 0$, it is reduced to $\frac{1}{N_j}\sum_{s_j=0}^{N_j-1}\Theta_b(s_j) = 0.$ A brief proof for $b > 0$ and $b' > 0$ is shown below.

$$\frac{\sum_{s_j=0}^{N_j-1}\Theta_b(s_j)\Theta_{b'}(s_j)}{N_j}=\frac{\Theta_b(0)\Theta_{b'}(0)+\Theta_b(1)\Theta_{b'}(1)+\Theta_b(2)\Theta_{b'}(2)+\Theta_b(3)\Theta_{b'}(3)}{4}$$
$$=\frac{\cos(\frac{b\pi}{8})\cos(\frac{b'\pi}{8})+\cos(\frac{3b\pi}{8})\cos(\frac{3b'\pi}{8})+\cos(\frac{5b\pi}{8})\cos(\frac{5b'\pi}{8})+\cos(\frac{7b\pi}{8})\cos(\frac{7b'\pi}{8})}{2}$$
$$=\frac{1}{4}\left[\begin{array}{l}\cos(\frac{(b-b')\pi}{8})+\cos(\frac{(b+b')\pi}{8})+\cos(\frac{3(b-b')\pi}{8})+\cos(\frac{3(b+b')\pi}{8})\\+\cos(\frac{5(b-b')\pi}{8})+\cos(\frac{5(b+b')\pi}{8})+\cos(\frac{7(b-b')\pi}{8})+\cos(\frac{(b+b')\pi}{8})\end{array}\right],$$

(10)

When $b'=b$, equation (10) becomes:

$$\frac{\sum_{s_j=0}^{N_j-1}\Theta_b(s_j)\Theta_{b'}(s_j)}{N_j}=\frac{1}{4}\left[4+\cos(\frac{b\pi}{4})+\cos(\frac{3b\pi}{4})+\cos(\frac{5b\pi}{4})+\cos(\frac{7b\pi}{4})\right]$$
$$=\frac{1}{4}\left[4+\cos(\frac{b\pi}{4})+\cos(\frac{3b\pi}{4})+\cos(2b\pi-\frac{3b\pi}{4})+\cos(2b\pi-\frac{b\pi}{4})\right] \quad (11)$$
$$=1.$$

When $b'=b+n$, (n may take the value of 1, 2, or 3)

$$\frac{\sum_{s_j=0}^{N_j-1}\Theta_b(s_j)\Theta_{b'}(s_j)}{N_j}=\frac{1}{4}\left[\begin{array}{l}\cos(\frac{n\pi}{8})+\cos(\frac{3n\pi}{8})+\cos(\frac{5n\pi}{8})+\cos(\frac{7n\pi}{8})\\+\cos\left(\frac{(2b+n)\pi}{8}\right)+\cos\left(\frac{3(2b+n)\pi}{8}\right)+\cos\left(\frac{5(2b+n)\pi}{8}\right)+\cos\left(\frac{7(2b+n)\pi}{8}\right)\end{array}\right]$$
$$=\frac{1}{4}\left[\begin{array}{l}\cos(\frac{n\pi}{8})+\cos(\frac{3n\pi}{8})+\cos(n\pi-\frac{3n\pi}{8})+\cos(n\pi-\frac{n\pi}{8})\\+\cos\left(\frac{(2b+n)\pi}{8}\right)+\cos\left(\frac{3(2b+n)\pi}{8}\right)+\cos\left((2b+n)\pi-\frac{3(2b+n)\pi}{8}\right)+\cos\left((2b+n)\pi-\frac{(2b+n)\pi}{8}\right)\end{array}\right]$$
$$=0.$$

(12)

Typically, the property value F is normalized per unit cell for fitting the cluster expansion, and symmetry can be used to reduce the cluster expansion:

$$f(\mathbf{s}) = \sum_{\alpha} V_{\alpha} m_{\alpha} \varphi_{\alpha}(\mathbf{s}), \tag{13}$$

where $f(\mathbf{s})$ is the property value $F(\mathbf{s})$ per unit cell, α is an "orbit" of symmetrically equivalent cluster functions, *m* is the multiplicity (number of cluster functions in α per unit cell), and $\varphi_{\alpha}(\mathbf{s})$ is called a "correlation", which is the average value of all cluster functions in α :

$$\varphi_{\alpha}(\mathbf{s}) = \frac{\sum_{\mathbf{b} \in \alpha} \Phi_{\mathbf{b}}(\mathbf{s})}{N_{\alpha}}. \tag{14}$$

To determine the unknown ECI of the cluster expansion, training data from high-fidelity calculations (e.g. *ab initio* method) is used. The training data can be represented by a set of (**X, y**) where **X** is a matrix of $n \times p$ with $X_{i\alpha} = \varphi_{\alpha}(\mathbf{s}_i)$ and **y** is a column vector of $n \times 1$ with $\mathbf{y} = \left[y_0, y_1, ..., y_n \right]^{\mathrm{T}}$. Here, *n* is the number of entries, e.g. structures or energies, in the training set and *p* is the number of symmetrically distinct cluster functions (orbits). Then the ECI can be estimated using a least-squares fit:

$$\hat{\mathbf{V}} = (\mathbf{X}^{\mathrm{T}}\mathbf{X})^{-1}\mathbf{X}^{\mathrm{T}}\mathbf{y}, \tag{15}$$

where $\hat{\mathbf{V}}$ is a column vector containing the predicted value of $m_{\alpha}V_{\alpha}$.

Observe that if $n < p$, i.e. the number of training data is less than the number of cluster functions generated, the above ($\mathbf{X}^{\mathrm{T}}\mathbf{X}$) is singular. This is a problem especially for surface cluster expansions and nanoparticle cluster expansions in which there are typically more symmetrically distinct clusters than those of the bulk cluster expansions. Thus, generating

significantly more training data is required, or the use of cluster selection to trim down the number of clusters included in the expansion is needed.

Alternatively, it is shown that using Tikhonov regularization can make the above problem well-posed.[65-66] In the next section, the machine learning (e.g. Bayesian) approach to fitting the cluster expansion is discussed in more detail. For example, in a Bayesian cluster expansion,[67] the predicted ECI can be obtained by:

$$\hat{\mathbf{V}} = (\mathbf{X}^{\mathbf{T}}\mathbf{X} + \boldsymbol{\Lambda})^{-1}\mathbf{X}^{\mathbf{T}}\mathbf{y}, \tag{16}$$

where $\boldsymbol{\Lambda}^{-1}$ is the covariance matrix for a multivariate Gaussian prior probability distribution for the ECI. Equation (16) is one type of the Tikhonov regularization.

2.2 Machine learning approach to cluster expansion

Constructing a cluster expansion for low-dimensional systems can be computationally expensive, because the loss of translational symmetry will typically increase the number of ECI to be fit in the cluster expansion, and as a result the number of training set structures (by *ab initio* calculations) for reaching a given level of accuracy will also increase.

Thus, significant effort has been put into developing approaches to generating cluster expansions in a way that minimizes prediction error for a given training set size. Machine learning approaches such as

- cross-validation,[6]
- active learning,[6, 64, 68]

- feature selection,[48, 50-51, 67, 69-71]
- regularization,[17, 67, 69]

are all well established in this field and commonly used to address this problem.[72] In this dissertation, the use of regularization and cross-validation will be particularly highlighted.

In 2009, Mueller and Ceder[67] developed a machine-learned Bayesian approach to fitting cluster expansions, which incorporates physical insights explicitly into the ECI values prior to the fitting ($\mathbf{\Lambda}^{-1}$ matrix in equation (16)). For example, the prior probability distribution can be expressed as an exponentially (or other type of) decaying function of the distance between sites in the cluster, which has the physical insight that the interactions between atoms typically become smaller as the separating distance becomes larger (Figure 2c). Additional system-specific insights could be included as well. The exact shape of the prior probability distribution may be determined using cross-validation; the leave-one-out cross-validation (LOOCV) is a relatively good way to determine test set for the Bayesian approach.[67]

Many common forms of fitting cluster expansions can be expressed in the Bayesian framework.[67] For example, for the cluster selection or the simple least-squares fit without regularization (Figure 2a), the prior distributions are constant for cluster functions that are included, meaning that all values of V are equally likely (with no prior knowledge); the prior distributions are delta functions for cluster functions that are excluded, which means the values of V for these cluster functions are effectively forced to be zero.

In the "compressive sensing"[70] and "*lasso*"[71] approaches, a Laplace prior is used (Figure 2b), which is equivalent to ℓ^1 regularization of the ECI. The use of the ℓ^1 norm typically

results in a solution that is sparse (relatively few non-zero ECI)[67, 73] and thus might have the advantage of being less computationally expensive to evaluate the cluster expansion. However, its average prediction error is the largest among various prior shapes/functions, which is possibly due to the discontinuous nature in derivative of the Laplace prior.[73] Recently, Leong and Tan showed that by using a "*group lasso*" with the physical insight that a cluster is selected only after all its subclusters, the prediction errors are consistently smaller than *lasso*'s at every training set size.[74]

Gaussian prior probability distribution, resulting in ℓ^2 regularization, has the advantage of being easier to implement owing to its continuity in derivative. This results in more non-zero ECI than ℓ^1 regularization due to the derivative reaching 0 at minimum so the ECI cannot be optimized to zero normally by gradient-based algorithms. Those smaller ECI for larger clusters may be physically meaningful, e.g. long-range interactions. Nonetheless, the extra cost to evaluate the cluster expansion with more ECI is typically negligible. The use of prior probability distributions is most effective when the prior probability distributions are physically motivated (Figure 2c).[67] It is shown that using physically-motivated priors can significantly reduce the prediction error for a given training set size.[53, 67] Throughout this dissertation, the physically-motivated Gaussian priors will be used. For example, the inverse of the covariance matrix for the prior is diagonal and the elements could be (and there are more choices of the functional forms depending on the systems):

$$\lambda_{\alpha\alpha} = \begin{cases} 0, & n_\alpha = 0 \\ \lambda_1, & n_\alpha = 1, \\ \lambda_2 e^{\lambda_3 r_\alpha} e^{\lambda_4 n_\alpha}, & n_\alpha > 1 \end{cases} \tag{17}$$

where n_α is the number of sites in cluster function α, r_α is the maximum distance between sites, and λ_1, λ_2, λ_3, and λ_4 can be determined using a conjugate-gradient algorithm to minimize the root mean square leave-one-out cross-validation (LOOCV) error.

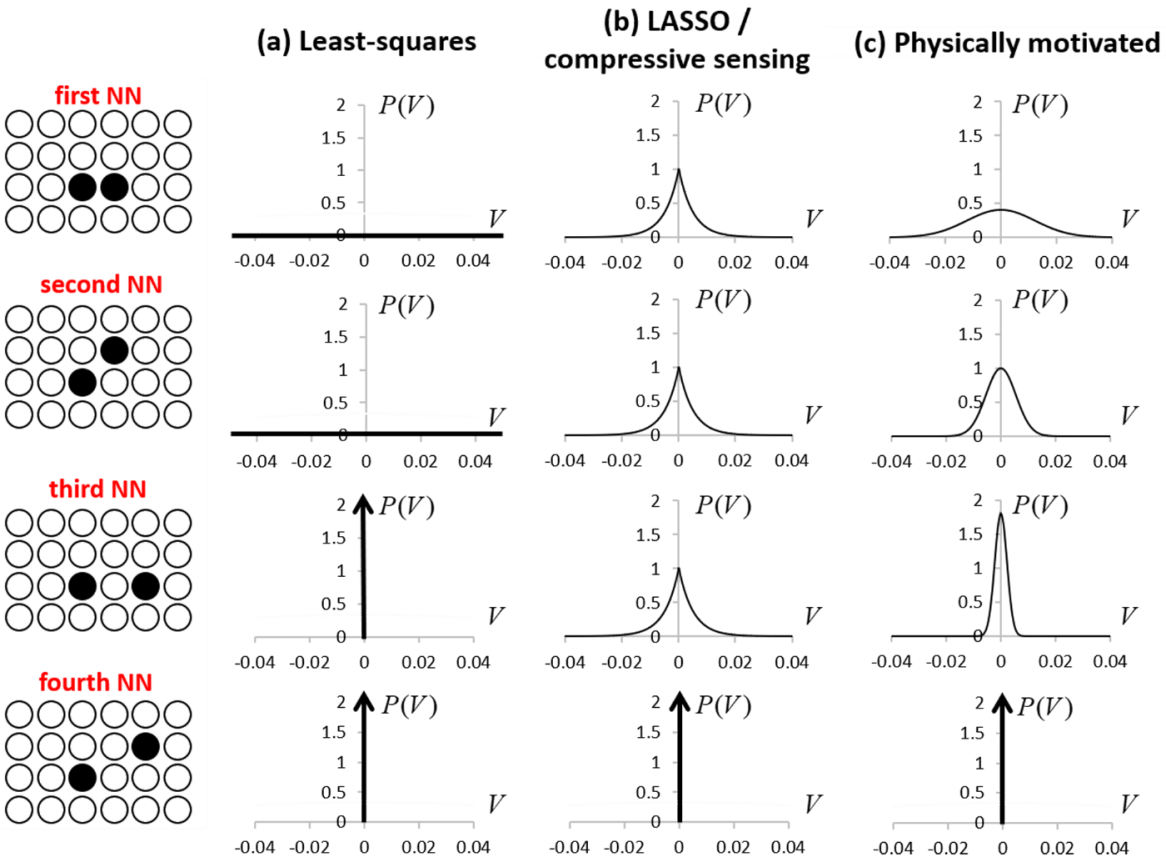

Figure 2. Bayesian interpretation of (a) least-squares fit, (b) *lasso* / compressive sensing, and (c) physically motivated Gaussian prior probability distributions under the assumptions that ECI typically become smaller as the distance between sites in the cluster becomes larger. V is the ECI value and $P(V)$ is the prior probability distribution for values of V. The dark vertical arrows indicate Dirac delta functions. Reproduced from ref. 72. Copyright 2018 American Chemical Society.

2.3 Applications of cluster expansion in materials

Cluster expansions have become a valuable tool for understanding structure-property relationships in materials research. A recent review published in 2018 by Cao *et al.*[72] has well summarized the progress and enthusiasm in this field as well as future directions. In this section a brief review will be given, with a few more interesting studies highlighted.

The use of cluster expansions on surfaces starts from the predictions of surface energies of alloys.[24, 27-28, 30] Subsequent studies on the ordering and segregation of alloy surfaces, kinetic Monte Carlo (KMC) simulations based on cluster expansion Hamiltonians, and rational design of catalysts, are among the active topics.[24, 27-33, 35-36, 38-39, 43] For example, Han *et al.*[31] developed a coupled cluster expansion of a Pt/Ru surface with adsorbed oxygen to model surface segregation in Pt-Ru surfaces in oxidizing environments. In 2019, Cao *et al.* developed surface cluster expansions that explicitly account for lattice parameters (strain-dependent cluster expansions), enabling the predictions of adsorbate binding energies and catalytic activities at every point in the alloy phase diagram.[75]

The initial construction of cluster expansion on nanoparticles of fixed size and shape was performed by Yuge in 2010.[44] Since then, nanoparticle cluster expansions have been implemented to study the shapes of nanoparticles,[45, 53, 76-77] internal atomic ordering with and without adsorbates,[50, 53, 60-61, 78] and adsorbate binding energies on nanoparticles of fixed shape.[51-52, 77-79] It is worth noting that cluster expansions on nanoparticles with fixed size and shape cannot be used to directly predict the structure-property relationships of such nanoparticles, since there is no guarantee that the shape would be the same as (or close to) the equilibrium shape observed in real experiments.

To model realistic nanoparticles with varied size and shape, the vacuum space outside of a nanoparticle needs to be treated as lattice sites as well; each of these sites can be occupied by either a metal atom or a "vacancy", an extra species introduced into the cluster expansion. Examples can be found by Mueller and co-workers in ref. 45, 54-56. As the size and shape of the nanoparticle changes, so do the subsets of vacant and occupied sites on the lattice. This will significantly increase the computational cost of generating such cluster expansions due to the increasing number of combinatorial ECI that need to be fit and thus it can become challenging for studying medium- and high-entropy alloys at the nanoscale.

In the next two chapters of the dissertation, further developments of the cluster expansion method on nanoparticles are presented. The first part (Chapter 3) focuses on developing a higher-order cluster expansion with varying shapes and with surface adsorbate included explicitly, enabling the direct comparison with experimentally characterized nanoparticles. The second part (Chapter 4) focuses on developing a transition-state cluster expansion for the more accurate prediction of transition rates of diffusion, which will be used in kinetic Monte Carlo (KMC) simulations.

3. Pt-Cu Nanoparticle

3.1 Background and motivation

Alloy nanoparticles are a promising class of catalysts due to their tunable size, shape, composition, and surface atomic structure[80-82] and thus have great potentials of being active and selective for the application of catalysis (e.g. fuel cells). The rational design of alloy nanocatalysts is however limited by the challenges present both computationally and experimentally in the understanding of the structure-property relationships at the nanoscale. To design a bimetallic nanocatalyst, the following effects need to be considered: the effect of lattice parameters (the strain effect), the effect of alloying on the electronic structures (the ligand effect), and the effect of local atomic order near the active sites (the ensemble effect),[83] so that general trends and design rules can be gained. Computationally, it is feasible to use high-fidelity density functional theory (DFT)[84-85] calculations to predict the structures and properties of single-crystal periodic surfaces and small nanoparticles (up to ~3 nm wide).[86-91] However, directly predicting the realistic structures as well as catalytic properties of nanoparticles at experimentally relevant sizes or even the energies using DFT is prohibitively expensive.

The use of cluster expansion offers a fast and accurate way to predict the energies of such systems that exhibit substitutional disorder. Cluster expansions[1-2] are energy models, usually fit to DFT calculations, that are capable of accurately (within about 5 meV per atom of DFT) predicting the energies of millions of nanoparticles per minute. Cluster expansions trained on small-size (1~2 nm in diameter) nanoparticles can be used in Monte Carlo[92] simulations to predict structures and thermodynamic properties of larger nanoparticles.

As discussed in the previous chapter, nanoparticle cluster expansions have been at the forefront of computational modeling of nanoscale materials and have been successfully applied to study i) nanoparticle shapes,[45, 53, 76-77] ii) internal atomic ordering with and without adsorbates,[50, 53, 60-61, 78] and iii) adsorbate binding energies on nanoparticles of fixed shape.[51-52, 77-79] However, there has been relatively little work on directly comparing the nanoparticle structures predicted by the cluster expansions with those of experimentally synthesized particles at the same time simulating experimental conditions.

In this work, comparisons of the cluster expansion predicted 5~10 nm Pt-Cu nanoparticles of varying size, shape, and composition with experimental characterization of Pt-Cu bimetallic nanoparticles have been made possible. The predicted lattice parameters, surface compositions, and shapes of the alloy nanoparticles are found to in good agreement with experiments. In addition, to account for the adsorbate-induced surface segregation, it is demonstrated that the best agreement for surface compositions can be achieved by a novel cluster expansion for alloy nanoparticles of varying shape and size that explicitly includes adsorbed oxygen. The Pt-Cu model system is of interest because Pt-based bimetallic alloys are promising catalysts for the oxygen reduction reaction (ORR) from both theoretical[88, 93-95] and experimental studies,[95-100] and Cu-based catalysts are being extensively studied for CO and CO_2 reduction reaction.[99, 101-107] Experimental work was done by the Wang group[1]. This chapter is based in part on the published work in ref. 57 (C. Li[†] and D. Raciti[†] *et al.* J. Phys. Chem. C, 2018, 122, 31, 18040).

[1] Prof. C. Wang and his students D. Raciti and T. Pu.
[†] Equal contribution.

3.2 Methodology

3.2.1 Cluster expansion

Following the cluster expansion method described in Chapter 2, the construction of the cluster expansion and training set for the fitting will be described in this section. For nanoparticles with varying shape and size, the vacuum space around the nanoparticle was treated as a collection of sites that are occupied by "vacancy" (Figure 1). Thus, it is instructive to use a training set of small nanoparticles (e.g. 1~2 nm in diameter) to construct a cluster expansion that can be used to rapidly and accurately predict the properties of larger nanoparticles with varying shape, size, composition, and atomic order.[79]

To investigate the Pt-Cu alloy nanoparticle, a ternary cluster expansion was constructed based on an fcc lattice, where each site can be occupied by platinum (Pt), copper (Cu), or a vacancy. Site variable values of 0, 1, and 2 were assigned to these species. A quaternary cluster expansion with oxygen (O) added to simulate the oxidizing environments was constructed in a similar way, where the site variable values of 0, 1, 2, and 3 were assigned to Pt, Cu, O, and vacancy, respectively. A discrete cosine basis was used to generate the cluster functions (see equation (5)).

In this work, the training set for the Pt-Cu-vacancy cluster expansion contained 122 nanoparticles ranging from 90~250 atoms and the training set for the Pt-Cu-O-vacancy cluster expansion contained 193 nanoparticles ranging from 90~344 atoms. The general procedure/strategy for building and refining a cluster expansion is as follows:

a) generate random structures across all composition range,

b) calculate their energies using DFT,

c) add them to the training data set,

d) predict low-energy structures using the current cluster expansion,

e) and repeat steps b–d until the cluster expansion is converged (e.g. newly predicted structures are similar to the ones that already exist in the training set and they have low leave-one-out cross-validation errors).

The above procedure also applies to other chapters in the dissertation. Here, the training set contained 28 ground-state (low-energy) structures in total. In addition, bulk structures were added twice (2 bulk Pt, 2 bulk Cu, and 2 "empty" structures) to the training data, making sure that the bulk energies are sufficiently accurate. The cluster expansion was truncated to include the empty cluster, the one-body (point) cluster, all two-body (pair) clusters up to the seventeenth-nearest neighbor, all three-body clusters up to the sixth-nearest neighbor, and all four-body clusters up to the third-nearest neighbor, for a total of 531 symmetrically distinct cluster functions for Pt-Cu-vacancy cluster expansion, and 1827 symmetrically distinct cluster functions for Pt-Cu-O-vacancy cluster expansion. The ECI for these cluster functions were fit to the training set using the Bayesian approach with a multivariate Gaussian prior distribution.[67] This approach allows for more distinct ECIs to be included in the cluster expansion than there are structures in the training set. The inverse of the covariance matrix for the prior was diagonal, with elements given by:

$$\lambda_{\alpha\alpha} = \begin{cases} 0, & n_\alpha = 0 \\ \lambda_1, & n_\alpha = 1 \\ \lambda_2 e^{\lambda_3 r_\alpha} e^{\lambda_4 n_\alpha}, & n_\alpha > 1 \end{cases} \tag{18}$$

where n_α is the number of sites in cluster function α, r_α is the maximum distance between sites, and λ_1, λ_2, λ_3, and λ_4 were determined using a conjugate-gradient

algorithm to minimize the root mean square leave-one-out cross-validation (LOOCV) error, which is an estimate of the prediction error.[108] The resulting Pt-Cu-O-vacancy cluster expansion has a LOOCV error of 4.5 meV per atom relative to DFT calculations and Pt-Cu-vacancy cluster expansion has a LOOCV error of 3.9 meV per atom relative to DFT calculations.

3.2.2 DFT calculations

DFT calculations were performed using the Vienna Ab initio Simulation Package (VASP)[85] with the Perdew-Burke-Ernzerhof (PBE)[109] exchange-correlation functional. The Cu, Pt_pv, and O_GW PBE projector-augmented wave (PAW)[110] potentials were used, and all VASP calculations were run with accurate precision, ensuring that there were no wrap-around errors. A single *k*-point at the center of the Brillouin zone was used for each nanoparticle. For bulk materials (Pt and Cu), the Brillouin zone was sampled using grids generated by the *k*-point grid server[111] with a minimum distance of 46.5 Angstrom in real space lattice. Second-order Methfessel-Paxon smearing[112] with a width of 0.2 eV was used to set partial occupancies. Real space projectors were used to evaluate the non-local part of the PAW potential. The convergence criteria for the electronic self-consistent iteration and the ionic relaxation loop were set to be 10^{-4} eV and 10^{-3} eV per cell, respectively.

3.2.3 Reference chemical potential

To simulate the nanoparticle morphology evolution in oxidizing environments, the chemical potential of oxygen was set to that of oxygen provided by N_2O from experiments. The standard-state chemical potential of oxygen provided by N_2O can be calculated as

$$\mu_O = H_0(N_2O) - H_0(N_2) - T\Delta S_0^{\exp}, \tag{19}$$

where H_0 is the standard-state enthalpy and $\Delta S_0^{\exp}$ is the standard-state difference in entropy between N_2O and N_2 from experiments (NIST-JANAF tables).[113] DFT could be used to approximate the value of $H_0(N_2O) - H_0(N_2)$, however, it is possible that there may be errors in the DFT calculation of $E_{DFT}(N_2O) - E_{DFT}(N_2)$, where E_{DFT} indicates a DFT-calculated energy. Alternatively, this difference can be better expressed in terms of the experimental enthalpy of formation for N_2O,

$$H_0(N_2O) - H_0(N_2) = \Delta H_0^{\exp}(N_2O) + \frac{1}{2}H_0(O_2), \tag{20}$$

where $\Delta H_0^{\exp}(N_2O)$ is the standard-state enthalpy of formation for N_2O. Substituting equation (20) into equation (19) yields:

$$\mu_O = \Delta H_0^{\exp}(N_2O) + \frac{1}{2}H_0(O_2) - T\Delta S_0^{\exp}. \tag{21}$$

Again, DFT could be used to directly calculate $H_0(O_2)$, but it is well known that GGA (and LDA) can have large errors when calculating the energy of gas phase O_2 molecule due to overbinding. It is thus necessary to add a correction term to the DFT-calculated energy to accurately reproduce experimental formation enthalpies.[114] Using a method

similar to that of Wang *et al.*,[115] the average difference between DFT-calculated energies and experimental formation enthalpies of seven non-transition metal oxides (CaO, MgO, Li_2O, Al_2O_3, SiO_2, Na_2O and K_2O) was calculated to be 1.252 eV (Figure 3). With this correction term applied, equation (21) becomes

$$\begin{aligned}\mu_O &= \Delta H_0^{\exp}(N_2O) + \frac{1}{2}\left[E_{DFT}(O_2) + 1.252\ \text{eV}\right] - T\Delta S_0^{\exp} \\ &= \mu_0^{\exp}(N_2O) - \mu_0^{\exp}(N_2) + \frac{1}{2}\left[E_{DFT}(O_2) + 1.252\ \text{eV}\right],\end{aligned} \tag{22}$$

using the fact that the experimental enthalpy of formation for O_2 in the standard state is 0. Equation (22) was used to calculate the chemical potential of oxygen in this work. The chemical potential at a given partial pressure was adjusted using $\mu_P = \mu_{P_0} + kT\ln(\frac{P}{P_0})$ to match experimental conditions. The enthalpy of formation under standard states were obtained from the NIST-JANAF tables.

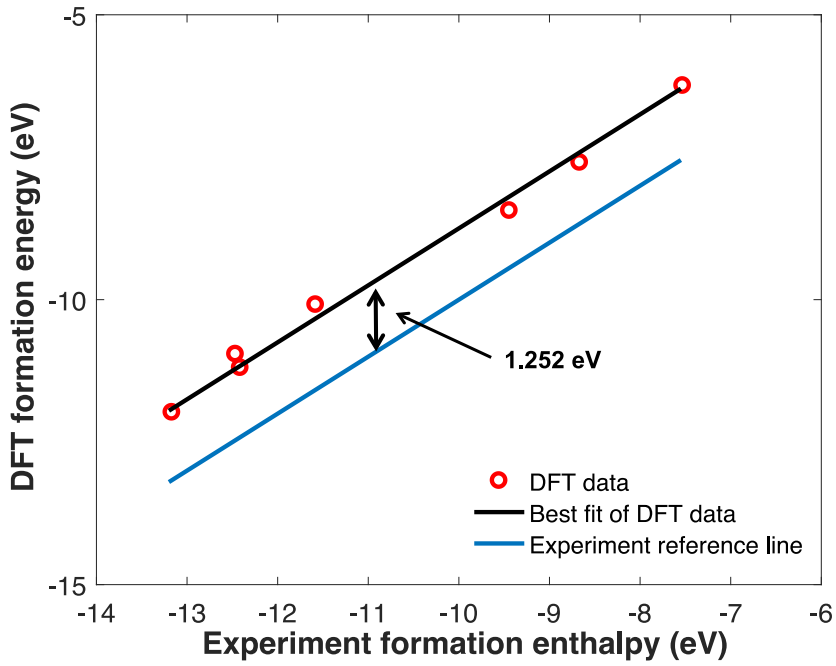

Figure 3. DFT-calculated formation energy of non-transition metal oxides (per O_2 in the reaction) as a function of experimental enthalpy of formation. The blue line is an experimental reference line, and the black line is the best linear fit of the DFT calculated formation energies.

3.3 Results and discussion

3.3.1 Lattice parameter cluster expansion

The Pt-Cu-vacancy lattice parameter cluster expansion was fit to the nearest neighbor distances of the relaxed structures in the DFT training set. The leave-one-out cross-validation (LOOCV) error for this cluster expansion, a measure of its predictive accuracy, was 0.004 Angstroms per bond.

Good agreement has been obtained between cluster expansion predicted lattice parameters and experimental measurements at room temperature for ~5 nm Pt-Cu nanoparticles of varying composition (Figure 4a). This is not surprising as the lattice parameters largely

follow the Vegard's law.[116] For Cu-rich nanoparticle, the experimentally measured $PtCu_3$ lattice parameter has the largest deviation (~1%) from cluster expansion prediction, possibly due to aggregation of nanoparticles and formation of copper oxides.[57] The relative trend of lattice parameters for the pure phases are also verified: cluster expansion predicted lattice parameters of the 5 nm Pt and Cu nanoparticles should fall in between those of the 2 nm nanoparticles and bulk materials (green and red points, Figure 4) calculated by DFT.

It then becomes straightforward to also assess the size-dependent lattice parameters of the Pt-Cu nanoalloy. The predicted lattice parameter indeed contracts with particle size (Figure 4b), which is consistent with previously reported experimental and theoretical results on size effects.[117-119] For pure Pt and pure Cu, the results are being compared with an analytical expression derived by Qi and Wang,[118]

$$a_{NP}(D) = a_{bulk}\left(1 - \frac{1}{1+\sqrt{\alpha}DG/\gamma}\right), \tag{23}$$

where α is a geometry factor defined as the ratio of the surface area of a non-spherical nanoparticle to that of a spherical nanoparticle of the same volume, (1.000 for Cu sphere and 1.105 for Pt cuboctahedron), D is the diameter of the nanoparticle, G is the shear modulus and γ is the average surface energy. Least-squares fits were performed and it is found that the G/γ ratios of 45.9 and 42.4 nm^{-1} give the best fit for pure Pt and pure Cu, with root-mean-square errors being 0.0029 and 0.0021 Angstrom, respectively. These values are comparable to ratios of 24.3 and 26.9 nm^{-1} reported in the literature.[117-118]

Taken together, this cluster expansion is capable of predicting the lattice parameters of Pt-Cu nanoparticles of varying composition and size, and because of the Vegard's law the lattice parameter cluster expansion should also work robustly for other alloy systems.

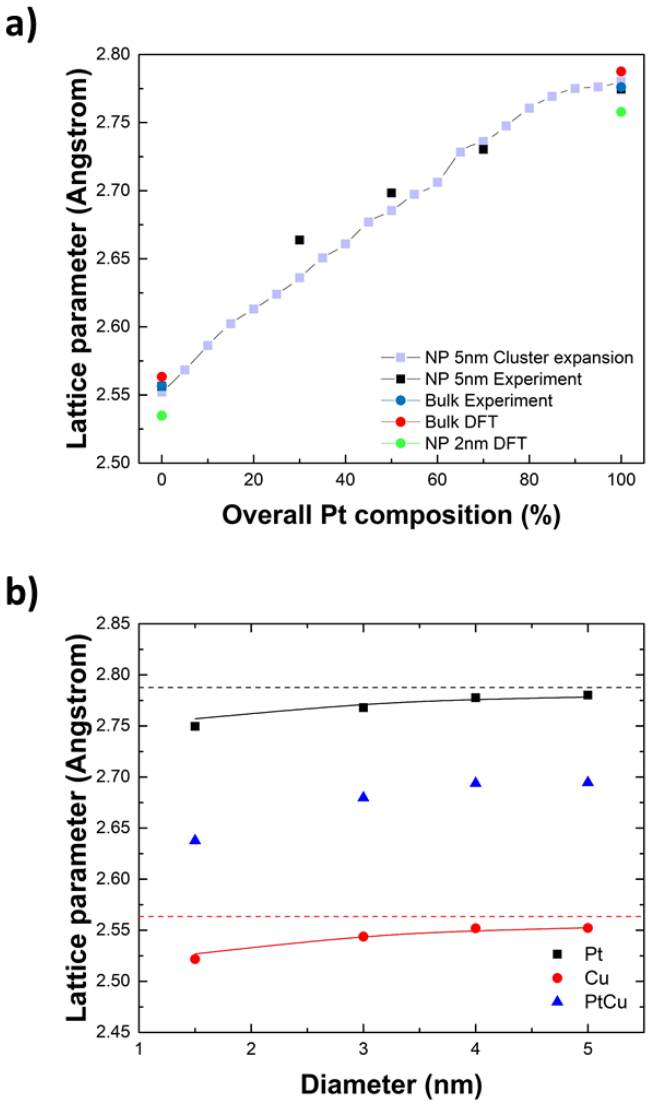

Figure 4. (a) Lattice parameters for Pt-Cu nanoparticles predicted by cluster expansion and measured by experiments.[57] The DFT calculated and experimental values for pure Pt and Cu bulk materials are also labeled. (b) Calculated size effect on lattice parameter of Pt, PtCu, and Cu nanoparticles. Horizontal lines represent bulk values predicted by the cluster expansion. Fitted curves are generated using the analytical expression from ref. 118.

3.3.2 Structure of Pt-Cu nanoparticles

With good agreement between lattice parameter prediction and experiment for the Pt-Cu nanoparticles across different compositions, the focus of this work has then moved forward to predicting the structure (i.e. shape) and near-surface composition of Pt-Cu nanoparticles. To this end, the DFT-calculated energies from the same training set used for the lattice parameter cluster expansion were used to fit a Pt-Cu-vacancy cluster expansion. Metropolis Monte Carlo simulations[92] were performed to identify low-energy structures and take thermodynamic averages at finite temperature.

In equilibrium at 25 °C, the Pt_3Cu nanoparticles exhibit a Pt skin and with a Cu-rich second layer (Figure 5 and Figure 6). This is consistent with previous experimental findings on near-surface alloys[120-121] and Cu-Pt core-shell nanoparticles after annealing in hydrogen (H_2).[122-123] It is observed that the Pt_3Cu nanoparticles have well-defined facets, with Pt(100) and Pt(111) facets being the dominant facets, which is consistent with Wulff constructions reported in the literature.[124-125] It is also interesting to see that the second layer is somewhat disordered (Figure 6), similar to what has been found for the Pt_3Ni system, which is a highly active catalyst for the oxygen reduction reaction (ORR).[75, 79, 89] The core region of the Pt_3Cu nanoparticle is predicted to have a $L1_2$ ordering (Figure 6), which is in agreement with the Pt-Cu phase diagram.[126]

When the overall Cu concentration increases to 50% (i.e. the PtCu nanoparticles), Cu atoms have segregated out to the surface, with (110) edge sites being the preferred occupied sites, as well as some of the (100) surface sites. Although the area of the Pt(111) facets gets reduced because of the creation of the additional (110) facets, most of the Pt(111) facets are still present at this composition (Pt : Cu = 1 : 1). This shape change is in agreement

with the experimental TEM images (Figure 5, first and second row), in which the Pt-Cu nanoparticle becomes less faceted when overall Cu composition increases.[57] The predicted composition-dependent shapes are consistent with Pt-Cu nanoparticle shapes reported in the literature.[127-128]

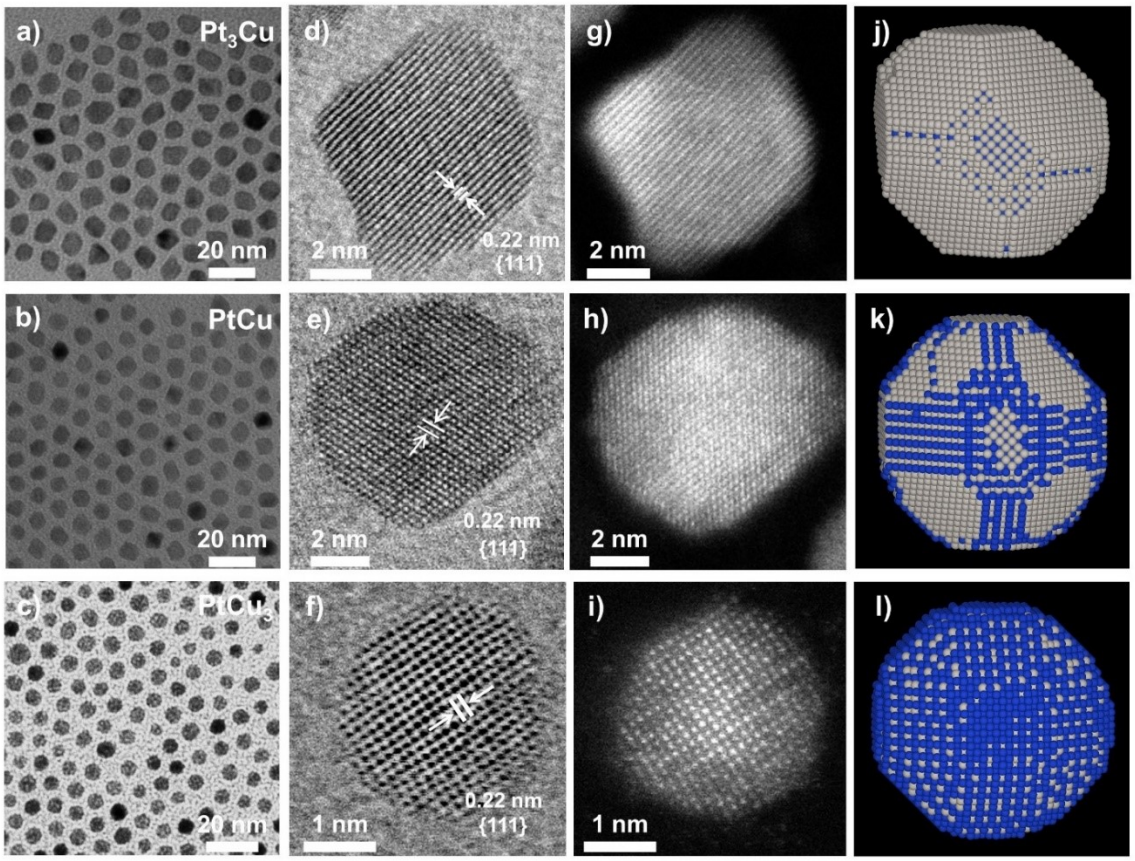

Figure 5. (a-i) TEM/HAADF-STEM images and (j-l) cluster expansion predicted structures for ~7 nm (13,000 atoms) Pt_3Cu, PtCu, and $PtCu_3$ nanoparticles.[57] Gray and blue spheres represent Pt and Cu atoms, respectively. Atomic structural images were generated using VESTA.[129]

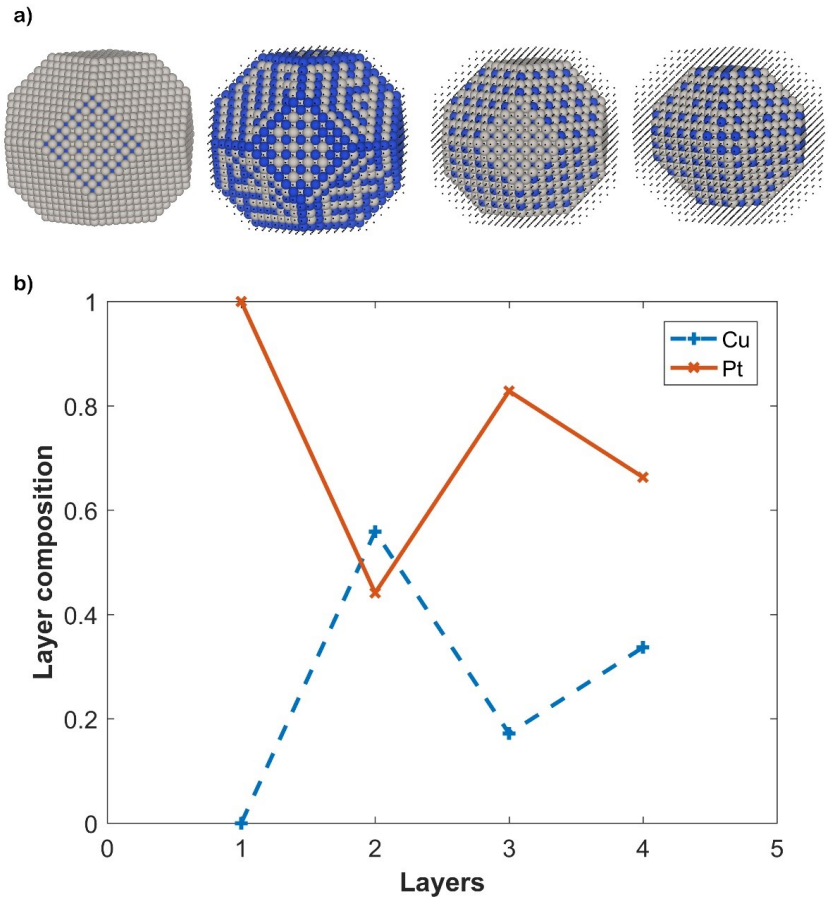

Figure 6. (a) Snapshots of layer-by-layer (1st, 2nd, 3rd, and 4th layer) structures of ~5 nm Pt_3Cu ($Pt_{3750}Cu_{1250}$) and (b) layer composition profiles (up to four layers). Gray and blue spheres represent Pt and Cu atoms, respectively. Small dots in a) are the atoms removed from outmost layers. Atomic structural images were generated using VESTA.[129]

Once the overall Cu content exceeds 50%, the surface fraction of Cu increases more rapidly. At a higher Cu composition ($PtCu_3$ nanoparticles) it is observed that the (100) surface sites are nearly all occupied by Cu atoms, whereas the rest of surfaces exhibit a pattern of $L1_2$ ordered phase with ratio of $PtCu_3$, which is in agreement with the Pt-Cu phase diagram.[126] Further shape change is observed: the $PtCu_3$ nanoparticles becomes even less faceted and more spherical than PtCu nanoparticles, which arises from the increasing area of (100) and (110) facets. It is likely that the difference in surface energies plays a role for the different

equilibrium shapes. To support this argument, DFT calculations on the surface energies of various facets of Cu and Pt (Table 1) were carried out. It is found that the surface energies of Cu are lower than those of Pt, and the Cu surface energies for different facets are closer to each other than the Pt surface energies are. Thus, the cluster-expansion-predicted surface segregation and shape change are consistent with what would be expected based on the surface energies (see Wulff constructions in Figure 7).

Table 1. Surface energies of (111), (110), and (100) facets for Cu and Pt.

	γ_{Cu} (meV/Å^2)	γ_{Pt} (meV/Å^2)
(111)	95.42	111.45
(110)	112.24	141.55
(100)	106.79	139.31

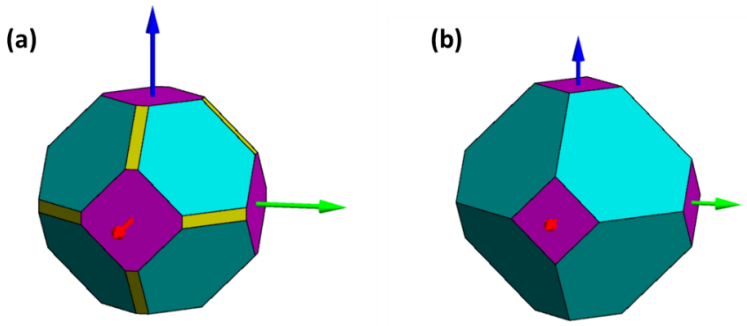

Figure 7. Wulff constructions of (a) Cu and (b) Pt nanoparticles based on DFT-calculated surface energies. Graphs were generated using the software by Zucker *et al.*[130]

3.3.3 Adsorbate-induced surface segregation

The advanced engineering and control of surface structures present ways to design more active catalysts, whether through the ligand effect, the ensemble effect, or even phase transition.[131-134] Surface adsorbate can also induce the preferential segregation of a species in alloy systems. It has been reported that when Pt-Cu nanoparticles are exposed to oxygen (or other oxidizing agents such as CO), Cu atoms can segregate to the surface and change the surface structure significantly.[135-136] The Pt-Cu-vacancy cluster expansion built in vacuum so far in this work (grey bars in Figure 8a), not surprisingly, cannot capture this oxidizing effect, and it underpredicts the Cu surface coverage by about 30% relative to experiments. (The experimentally measured surface coverages were obtained using a N_2O-H_2 titration method.[57, 137]) Such findings suggest that it is necessary to explicitly include the presence of possible oxygen adsorbates in the cluster expansion to realistically capture the effect of oxidation.

Note that it could be also possible that the room-temperature H_2 titration drives segregation of Pt to the nanoparticle surface,[99, 122] but this is likely a relatively small effect due to the weak Pt-H binding energy and low temperature during H_2 titration. The lack of H-induced segregation of Pt to the nanoparticle surface is supported by the low percentage of surface Pt observed on $PtCu_3$ nanoparticles (light blue bars in Figure 8a). Nonetheless, an extra atomic species can be included in the cluster expansion readily if were to investigate the effect of hydrogen or other type of species.

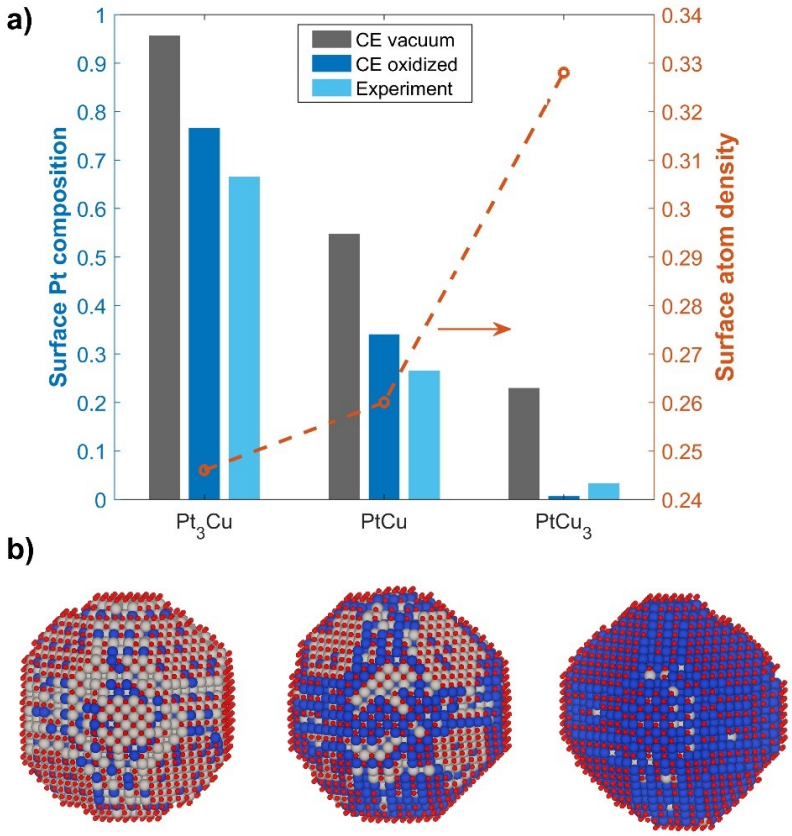

Figure 8. (a) Cluster expansion (CE) predicted surface Pt compositions of Pt-Cu nanoparticles in vacuum and oxidizing environment as a function of overall bulk concentration. Surface atom density is defined as ratio of number of surface atoms to total number of atoms in nanoparticles based on experimentally measured sizes. (b) Structures of Pt_3Cu, PtCu, and $PtCu_3$ in oxidizing environments. Gray, blue, and red spheres represent Pt, Cu, and O, respectively. Atomic structural images were generated using VESTA.[129]

3.3.4 Improved predictions

Previous works on cluster expansions of nanoparticles have either assumed the particle exists in vacuum,[45, 50, 53, 60, 77] used very small particles of fixed size and shape,[51-53, 77] or estimated the effects of adsorbates through the use of correction terms.[76, 78] Here, to address the problem of adsorbate-induced surface segregation in section 3.3.3, a novel nanoparticle cluster expansion that explicitly includes surface adsorbate is developed to study the

nanoparticles of varying size, shape, and composition. Specifically, each lattice site can be occupied by either Pt, Cu, O, or a vacancy, accounting for metal-adsorbate and adsorbate-adsorbate interactions. This cluster expansion has made the approximation of all the oxygen atoms sitting at fcc sites of the surface prior to relaxation (in DFT) although other adsorption sites may have lower energies. While this may introduce errors in cases where there exists another site with lower energy than the fcc site, it greatly improves the agreement between the cluster-expansion-predicted and experimentally measured surface compositions relative to the results where the particles were assumed to exist in a vacuum.[57]

The Pt-Cu nanoparticle morphology and surface composition were determined by running a grand canonical Monte Carlo simulation with a fixed oxygen chemical potential, which came from N_2O decomposition (see Methodology). Because no nanoparticles with oxygen in sub-surface layers were considered in the training set, Monte Carlo simulations were also constrained so that there was no oxygen present in the sub-surface layers. To simulate the synthesis of the nanoparticles, initially a Monte Carlo simulation was run in which the nanoparticles were annealed at a temperature of 500 °C, which is the highest temperature the particles reached before titration measurements. Then, the temperature was reduced to 90 °C to simulate the N_2O titration experiments.[57] At this temperature only the outermost three layers were allowed to be annealed, as it is likely that the core of the nanoparticle is kinetically trapped.[76]

Using this cluster expansion, the predicted surface Cu composition increases around 20% on average (dark blue bars in Figure 8a) from vacuum to oxidizing environment, partially due to the stronger binding of oxygen to Cu than to Pt.[138] Recent experimental studies also showed that a significant increase in Cu surface composition was observed in oxidizing

environments.[135-136] Although there was still a small gap between the cluster expansion prediction and experimental observation, the agreement with experiment is much better when the surface oxygen is explicitly included in the cluster expansion. Compared with the nanoparticles in vacuum, the nanoparticle shapes also changed (Figure 8b). For example, for Pt_3Cu, it is seen that the area of (110) facets increases and the area of (100) facets decreases, making the particle more spherical in oxidizing environments. At higher Cu concentration, Pt surfaces are no longer present, e.g. on $PtCu_3$. Instead, the particles have an oxidized copper surface. This is in line with the titration experiment, where a full monolayer of oxygen was observed,[137] and the oxygen coverages in the simulations are greater than 0.95 ML (Figure 9). It is worth pointing out that the changes of shapes may not occur in practice if the nanoparticles become kinetically trapped by the formation of the surface oxide; a kinetic Monte Carlo simulation based on the current cluster expansion could be used to investigate such effects.

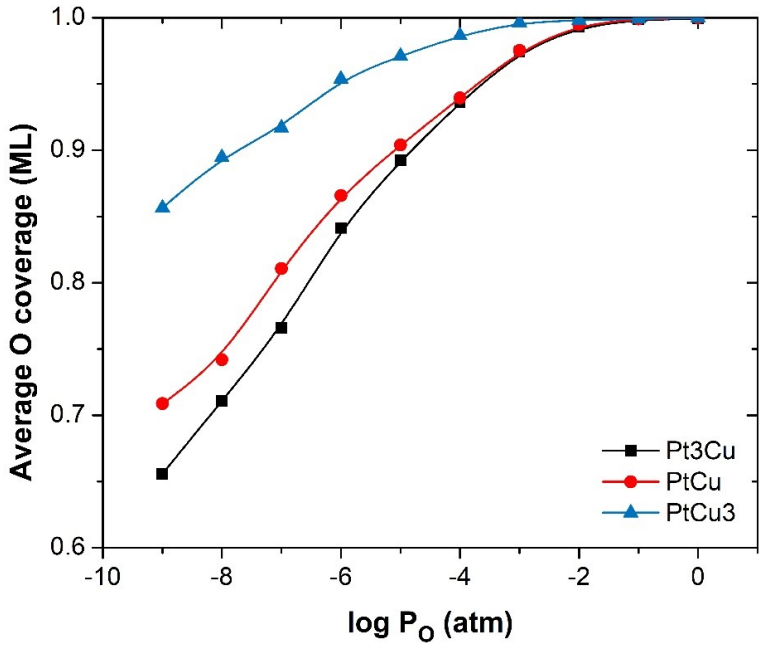

Figure 9. Average oxygen coverage on the surface of Pt_3Cu, PtCu, and $PtCu_3$ nanoparticles as a function of the oxygen partial pressure.

3.4 Summary and conclusion

Cluster expansions have been generated to investigate Pt-Cu nanoparticle structures in both vacuum and oxidizing conditions. The predicted lattice parameters, shapes, and surface compositions of the nanoparticles are found to be in good agreement with experimental characterizations. In particular, the results demonstrated that explicitly including potential oxygen adsorbates in cluster expansions can significantly improve the quality of the predicted structures of nanoalloys at experimentally relevant sizes and conditions. The success of this method paves the way for directly predicting the catalytic activity on different sites of nanoparticles with realistic structures using a cluster expansion, since the

adsorbate binding energies are important descriptors of the catalytic activity. This method can be extended to possibly include *OH adsorbates in studying the oxygen reduction reaction and can be used in a kinetic Monte Carlo simulation. Therefore, the method developed in this work would be promising to provide insights into the understanding of the structure-property relationships of nanoalloys in different chemical environments and facilitate the rational design of catalysts.

4. Pt-Ni Nanoparticle

4.1 Background and motivation

4.1.1 Cluster expansion for diffusion

Diffusion is the phenomenon of material transport by atomic movement,[139] and it plays an important role in determining various material properties such as the stability and activity of nanocatalysts,[140-144] the conductivity and stability of batteries[145-148] and fuel cells,[149-152] and the electrical properties of semiconductor devices.[153-156] Atomic diffusion in materials often consists of hops between local minima on the potential energy surface (PES), with atoms vibrating about these local minima in the time between hops. If these transition rates can be computed efficiently, the simulation of such hops and evolution of the system can be significantly accelerated through the use of kinetic Monte Carlo (KMC)[157-158], in which the states of the system evolving could be effectively treated as discrete jumps between local minima rather than continuous time evolution. By transition state theory,[159] these rates depend exponentially on the activation energies of the hops, making the accurate (and rapid) calculation of activation energies critically important to the success of a KMC simulation; and this should generally hold for other types of dynamic simulations as well.

Several methods for predicting activation energies have been proposed and implemented in the literature. These include the broken bond model[160-167] and a model based on Marcus theory,[168-170] which have been used in KMC simulations to investigate diffusion-related phenomena in materials such as dissolution, dealloying, intercalation, coalescence, crystal growth and so forth. These methods could be applied to a variety of material systems due to the relatively simple functional forms. However, the simplicity of these models limits their accuracy, and there would be no way to systematically improve them if the predicted

activation energies are not sufficiently accurate. An appealing alternative is to use the systematically improvable machine-learned energy/potential models such as the cluster expansions[2, 12] and interatomic potentials[171-178] for the accurate and rapid prediction of activation energies (A few successful practices are summarized in Table 2). As the cluster expansion is a lattice model explicitly designed to calculate the energies of local minima on the potential energy surface, it is particularly well suited for KMC. Other types of KMC schemes such as the off-lattice KMC are also worth pointing out.[179-180]

The cluster expansion has become a valuable tool for studying atomic order and structure-property relationships in alloys,[3, 23, 34, 45, 53, 57, 61, 77-79, 108, 132, 181-185] but it is rarely used to model diffusion.[12, 186] In 2001, Van der Ven and Ceder *et al.* demonstrated how cluster expansions could be used to predict activation energies in bulk Li_xCoO_2 by constructing two cluster expansions: a global cluster expansion of the local minima on the PES, and a local cluster expansion around the hopping atom that enabled the calculation of a "kinetically resolved activation barrier", a barrier independent of the hopping direction.[12] The combination of the two cluster expansions can then be used to calculate the activation energies of the hops, which have a directional dependence.

Table 2. Various models for predicting activation energies parameterized from *ab initio* data. The reported errors are root-mean-square errors (RMSE) unless otherwise noted.

	Approach	Fitting error / meV	Validation error / meV	Ref.
Vacancy-mediated diffusion in Pt-Ni nanoparticles	CE	83	127	This work
Lithium diffusion in Li_xCoO_2	CE	40	-	12
FCC solute diffusion (5 hosts)	ANN/GKRR	92~105	148~154	173
Impurity diffusion (15 hosts)	GPR/GKRR	-	116~155	171
Vacancy diffusion in Fe-Cu alloys	GPR	-	67[a]	172
Lithium diffusion in Li_3PO_4	ANN	48~73[a]	-	174
Self-diffusion on Cu surfaces	ANN	~161	-	175
Transition metal solute diffusion	SVM	92	142	176
Interstitial diffusion of nitrogen, oxygen, boron, and carbon in metals	GB	135	311	177
Cu bulk vacancy diffusion	SR	-	37~106	178

CE: cluster expansion; ANN: artificial neural network; GPR: Gaussian process regression; GKRR: Gaussian kernel ridge regression; SVM: support vector machine; GB: gradient boosting; SR: symbolic regression.

[a] mean absolute error.

4.1.2 Thesis research

In this work, a related approach to that of Van der Ven and Ceder *et al.* is developed. A single global cluster expansion is defined with transition states included explicitly as a set of sublattice sites, which could make it more compatible with general-purpose cluster expansion software packages and easier to extend to include collective hops in which multiple atoms can move simultaneously. The accuracy of this approach is assessed through a comparison with alternative (simpler) models for calculating the activation energy including the broken bond model and a model related to Marcus theory. It is found that the prediction error of the cluster expansion is similar to that of other models for small training set sizes, but with larger training set sizes the cluster expansion has a significantly lower error than the other models. For the purposes of the comparison, KMC simulations are carried out on the vacancy-mediated diffusion in Pt-Ni nanoparticles, which have been widely studied as potential catalysts for the oxygen reduction reaction.[75, 89, 140, 187-188] The cluster expansion has a comparable overall execution speed with other simpler models and the one related to Marcus theory yields predictions of nanoparticle evolution that are the most similar to those of the cluster expansion. This chapter is based in part on the preprint in ref. 189 (C. Li *et al.* arXiv:2009.12474, 2020).

4.2 Methodology

4.2.1 DFT calculations

Density functional theory (DFT)[84] calculations were performed using the Vienna Ab initio Simulation Package (VASP)[85] with the revised Perdew-Burke-Ernzerhof (RPBE)[109, 114

exchange-correlation functional. The Pt_pv_GW and Ni PBE projector-augmented wave (PAW)[110] potentials were used. A single *k*-point at the center of the Brillouin zone was used for each nanoparticle. For bulk materials, the Brillouin zone was sampled using generalized Monkhorst-Pack grids generated by the *k*-point grid server[111] with a minimum distance of 46.5 Å between real space lattice points. Second-order Methfessel-Paxon smearing[112] with a width of 0.2 eV was used to set partial occupancies. The convergence criteria for the electronic self-consistency iteration and the ionic relaxation were set to be 10^{-4} eV and 0.03 eV/Å, respectively. The climbing image nudged elastic band[190-191] (CI-NEB) method was used to calculate the activation energies of atomic diffusion, with a force convergence below 0.05 eV/Å.

4.2.2 Transition-state cluster expansion

Cluster expansions are generalized Ising models that account for many-body interactions[1-2] and are commonly used to study atomic order in substitutional materials.[17, 53, 57, 72, 78, 108, 192] In this application, the arrangement of atoms in the material is expressed as a set of discrete sites that are occupied by different elements. In the cluster expansion constructed here, the sites are arranged on an fcc lattice and each site can be occupied by a Pt atom, Ni atom, or vacancy. A discrete cosine basis was used to generate the cluster functions (see Chapter 2). The effective cluster interactions (ECI) of the cluster expansion were fit to a set of DFT-calculated energies using the Bayesian approach,[67] which has been shown to effectively improve the accuracy of the cluster expansion. Specifically, exponential decay in the prior distribution width with respect to the number of sites in each cluster and the maximum distance between sites was assumed.

In this work, the cluster expansion formalism is extended by explicitly adding the sublattice sites for all possible transition-state sites halfway between nearest-neighbor sites (Figure 10a). Each of these transition-state sites correspond to a saddle point on the PES for a hop between neighboring fcc sites, thus it allows for the prediction of the activation energies directly from the cluster expansion. The transition state energies and structures (where an atom is at a transition state site) in the training set were obtained from DFT nudged elastic band calculations (section 4.2.1).

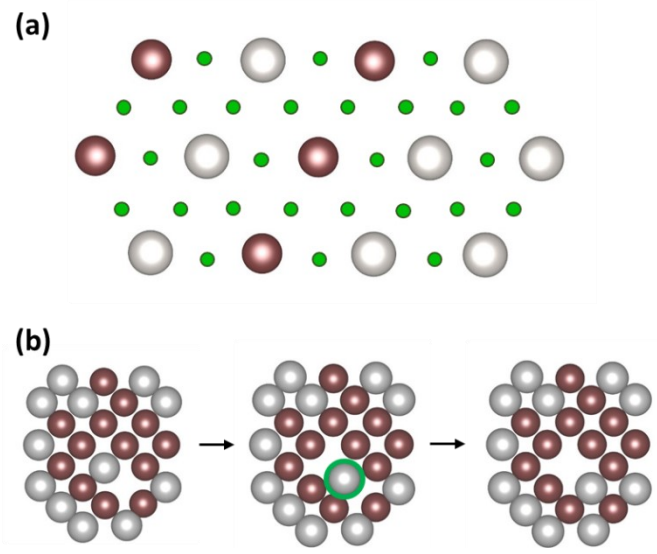

Figure 10. (a) A schematic of transition-state cluster expansion. Large gray and brown spheres represent Pt and Ni, respectively, on lattice sites (local minima on the PES). Small green dots represent transition states between two local minima. For illustration purposes a two-dimensional lattice is shown, but the model in this paper is based on a three-dimensional fcc lattice. (b) A set of training structures representing a diffusive hop, with the diffusing species at the transition state circled in green. From left to right: initial, transition, and final state.

For this cluster expansion, the allowed configuration space is physically constrained to prevent simultaneous occupation of a transition state site and a neighboring fcc site, i.e. clusters which contain both the transition state and a neighboring end state. For a similar

reason, the clusters that contain more than one transition state are also removed, effectively only allowing a single atom to hop. This framework could be extended to study collective hops in which multiple atoms move simultaneously along the diffusion path, which is likely to occur on surfaces particularly.[193-195] The constraints on the set of allowed configurations make the cluster expansion overdetermined, i.e. there are more possible cluster functions than possible configurations. The cluster expansion therefore needs to be simplified by removing unnecessary cluster functions. This is accomplished by removing all functions associated with clusters that include two sites that cannot be simultaneously occupied. As the number of remaining functions is then equal to the number of allowed configurations, and these functions are linearly independent, they form a complete basis for the constrained configurations.[189] It is worth noting that the simplification procedure is not limited to the studies of diffusion and can be used in any cluster expansion in which some sites cannot be simultaneously occupied.

A training set of 299 relaxed structures was generated using DFT for fitting the cluster expansion. The training set contained five bulk structures ("empty" structure, bulk Pt, bulk Ni, bulk PtNi, bulk Pt_3Ni) and the initial, transition, and final states of diffusive hops in different nanoparticles (ranging from 90 to 226 atoms). Each of the five bulk structures was included twice to ensure accuracy in the bulk limit. The last 84 structures in the training set were randomly generated surface hops, which are important to the structural evolution of the nanoparticle. The cluster expansion was truncated to include the empty cluster, point clusters, all two-body clusters up to a cutoff distance of 8 Å, all three-body clusters up to a cutoff distance of 6 Å, all four-body clusters up to a cutoff distance of 4 Å, all five-body clusters up to a cutoff distance of 4 Å, and all six-body clusters up to a cutoff distance of 4

Å. In addition to the 304 energies in the training set, 196 activation energies (energy differences between the transition state and the two corresponding end states) were explicitly included in the fitting to improve accuracy.[171, 196] An additional regularization parameter was introduced to distinguish the expected magnitude of ECI for clusters that include and do not include transition states. The cluster expansion contained 1097 symmetrically distinct cluster functions and the ECIs for these cluster functions were fit to the DFT-calculated training set using the Bayesian approach with a multivariate Gaussian prior distribution.[67] The inverse of the covariance matrix for the Gaussian prior was diagonal, with elements given by:

$$\lambda_{\alpha\alpha} = \begin{cases} 0, & n_\alpha = 0 \\ e^{-\lambda_1}, & n_\alpha = 1, \text{ include transition state} \\ e^{-\lambda_2}, & n_\alpha = 1, \text{ not include transition state} \\ e^{-\lambda_1} e^{\lambda_3 r_\alpha} e^{\lambda_4 n_\alpha}, & n_\alpha > 1, \text{ include transition state} \\ e^{-\lambda_2} e^{\lambda_3 r_\alpha} e^{\lambda_4 n_\alpha}, & n_\alpha > 1, \text{ not include transition state} \end{cases} \quad (24)$$

where n_α is the number of sites in cluster function α, and r_α is the maximum distance between sites. The λ_1, λ_2, λ_3, and λ_4 were determined using a conjugate-gradient algorithm to minimize the root mean square leave-one-out cross-validation (LOOCV) score, which is an estimate of the prediction error.[108] Final values of the parameters λ_1, λ_2, λ_3, and λ_4 for the Pt-Ni-vacancy cluster expansion are 20.843, 19.990, 1.787, 1.849, respectively. The cluster expansion has a LOOCV error of 0.127 eV for the activation energies and 1.203 meV per atom for the formation energies relative to DFT calculations.

4.2.3 Kinetic Monte Carlo

Kinetic Monte Carlo (KMC)[197-198] simulation was used to study the structural evolution of the Pt_3Ni nanoparticle, where atoms were only allowed to hop into neighboring vacant sites. Ni dissolution was allowed from a surface site with a coordination number less than 10 and all of its neighboring atoms having more than 2 nearest-neighbor atoms after Ni dissolution; a zero activation energy for Ni dissolution was assigned due to the fast dissolution rate observed from experiments.[140] The standard rejection KMC algorithm is as follows:

a) Start at time $t = 0$ with an initial state i and compute the number of all possible transition events N_i (diffusion and dissolution).

b) Randomly choose an event by uniformly sampling the N_i events and accept the event with a probability k_{ij} / k_0, where $k_{ij} = v\exp(-E_a / k_B T)$ is the transition rate from state i to j, E_a is the activation energy, v is the prefactor, and k_0 is an upper bound for the transition rate ($k_0 = v$ which corresponds to a zero activation energy). The same prefactor for diffusion and dissolution was used.

c) Update KMC time by $t := t + \Delta t$, where $\Delta t = (N_i k_0)^{-1} \ln(1/u)$, and u is a uniform random variable from $(0,1]$. $k_0 = 1$ was used for "KMC time".

d) Go to step b).

KMC simulation on a truncated octahedral Pt_3Ni nanoparticle with random initial atomic order ($Pt_{3411}Ni_{1137}$, with a diameter of approximately 6.2 nm) was performed. The supercell was 74.1 Å × 74.1 Å × 74.1 Å. Due to the rejection KMC scheme, a small activation energy of e.g. 0.3 eV at room temperature would result in an acceptance probability of about 10^{-5},

which would make the simulation more expensive. An elevated temperature of 1000 K was chosen to accelerate the dynamics and reduce the computational cost of the simulations. The KMC simulations were stopped when the KMC time reached 1500. The nearest-neighbor environments for the Pt-Ni nanoparticles were calculated using the equations below and averaged over five different runs. The values for N_{Pt-Pt}, N_{Pt-Ni}, and N_{Pt-Vac} are measurements of the average number of Pt-Pt bonds, Pt-Ni bonds, and Pt-vacancy bonds around a Pt atom (N_{Ni-Pt}, N_{Ni-Ni}, and N_{Ni-Vac} are for the Ni atom similarly).

$$\begin{aligned} N_{Pt-Pt} &= \frac{\#bond_{Pt-Pt}}{\#atom_{Pt}}, N_{Pt-Ni} = \frac{\#bond_{Pt-Ni}}{\#atom_{Pt}}, N_{Pt-Vac} = \frac{\#bond_{Pt-Vac}}{\#atom_{Pt}} = 12 - N_{Pt-Pt} - N_{Pt-Ni} \\ N_{Ni-Pt} &= \frac{\#bond_{Ni-Pt}}{\#atom_{Ni}}, N_{Ni-Ni} = \frac{\#bond_{Ni-Ni}}{\#atom_{Ni}}, N_{Ni-Vac} = \frac{\#bond_{Ni-Vac}}{\#atom_{Ni}} = 12 - N_{Ni-Pt} - N_{Ni-Ni} \end{aligned} \quad (25)$$

4.3 Results and discussion

4.3.1 Accuracy of predictive models

As the cluster expansion is trained on both formation energy and activation energy, it is expected to be able to predict both properties accurately. The predictive accuracy of the cluster expansion is assessed by using cross-validation. The root mean square leave-one-out cross-validation (LOOCV) errors are calculated to be 1.203 meV per atom for the formation energies and 0.127 eV per particle for the activation energies (Figure 11a and Figure 11b) relative to DFT calculations. The LOOCV error of the activation energies is equivalent to 0.944 meV per atom, which is of the same order of magnitude as the error for

the formation energies. Although assigning higher weights to the activation energies in the fitting could further lower the prediction error, however, the exact choice of the weight can be hard to justify and therefore will not be discussed.

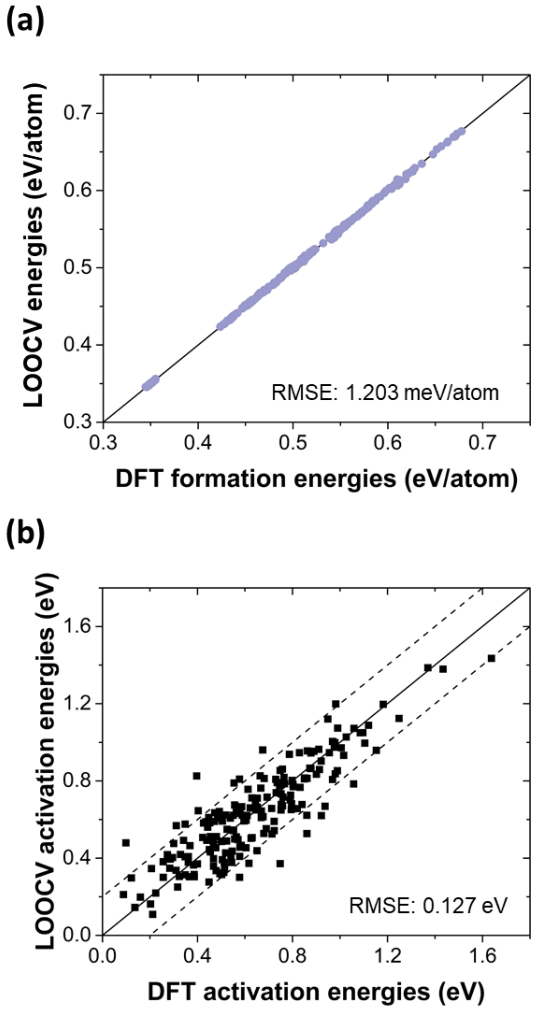

Figure 11. Leave-one-out cross-validation (LOOCV) of a) the formation energies and b) activation energies from the transition-state cluster expansion. The dashed lines in (b) indicate ± 0.2 eV deviation from perfect agreement.

To further validate the transition-state cluster expansion method, a Metropolis Monte Carlo[92] simulation in a canonical ensemble was used to predict the equilibrium surface

composition profile of a 4.5 nm Pt_3Ni nanoparticle ($Pt_{2547}Ni_{849}$) at 333 K. The Monte Carlo simulation was run from a high temperature (2000 K) and then decreased in steps by a factor of $4^{0.10}$ until 333 K. The near-surface composition profile (Figure 12) is similar to those which have been experimentally[89] and computationally[75, 199] determined for an extended $Pt_3Ni(111)$ surface, consistent with the fact that the surface of the cuboctahedral Pt_3Ni nanoparticle consists of mainly (111) facets. The bulk Pt_3Ni ordered structure is also found from the Monte Carlo simulation, largely because it was included twice in the training data for the cluster expansion.

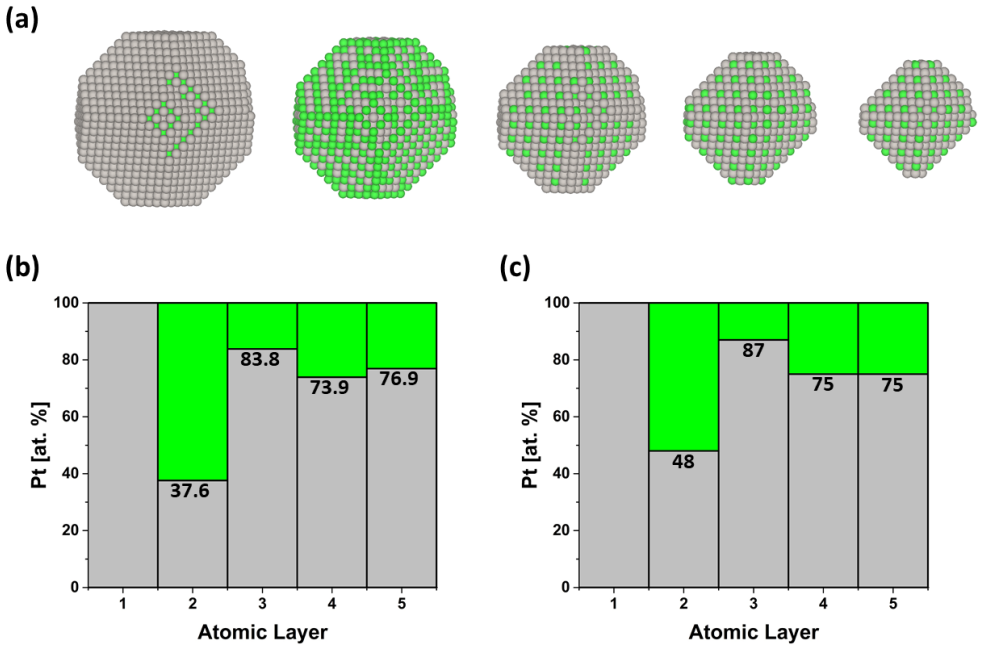

Figure 12. (a) Monte Carlo snapshots of a $Pt_{2547}Ni_{849}$ nanoparticle at 333 K, showing the first, second, third, fourth, and fifth layer, from left to right. Gray and green spheres represent Pt and Ni, respectively. (b) Thermodynamically averaged surface composition profile for a $Pt_{2547}Ni_{849}$ nanoparticle at 333 K. (c) Surface composition profile for a $Pt_3Ni(111)$ surface from experiments at 333 K.[89] Atomic-scale structural images were generated using VESTA.[129]

The accuracy of the transition-state cluster expansion for predicting activation energies is compared to other commonly-used simpler models (that were trained on the same training set): the broken bond model,[160] a model based on Marcus theory,[168] and a model previously used in which the activation energy for a hop to a lower-energy state is a constant value.[76, 140] This latter model will be referred as the "constant activation energy" model. In the broken bond model,[160] the activation energy for diffusion is calculated as a linear function of the number of nearest-neighbor bonds of each type (e.g. Pt-Pt, Pt-Ni, or Ni-Ni) that are broken when the hopping atom hops from the initial state. One of the drawbacks of this model is that it does not satisfy detailed balance, as the difference in activation energies between the forward and reverse hops will generally not be the same as the difference in energies between the end states. Detailed balance can be restored using an improved broken bond model in which a kinetically resolved activation (KRA) energy[163] is predicted as a function of the average number of bonds of each type at the initial and final states, and an energy term is explicitly included in this model. In the model based on Marcus theory,[168] the potential energy surface of the initial and final state of the reaction is approximated using a parabolic form. In this model, the activation energy can be analytically expressed as a function of the difference between the initial and final states (ΔE).[169] This model will be referred as the "parabolic potential" model. The final model, which has been used in previous work by Mueller and co-workers,[76, 140] uses a constant activation energy for hops to a lower-energy state and the same constant energy plus ΔE otherwise. The advantage of this model is that the value of the constant activation energy only affects the prefactor of the KMC simulation, so it is possible to simulate the dynamics of diffusion without

including any NEB-calculated activation energies in the training data. The functional forms of these models are provided in Table 3 below.

Table 3. Models used as comparisons to the cluster expansion in this work. The fitted parameters are determined by minimizing the RMS LOOCV error. n^i and n^f are the number of bonds at the initial and final state, respectively.

	Functional forms of activation energy	Fitted parameters	Schematics
Broken bond	$E_a = n^i_{Pt-Pt}E_{Pt-Pt} + n^i_{Pt-Ni}E_{Pt-Ni} + n^i_{Ni-Ni}E_{Ni-Ni}$	$E_{Pt-Pt} = 0.097$ eV $E_{Pt-Ni} = 0.066$ eV $E_{Ni-Ni} = 0.067$ eV	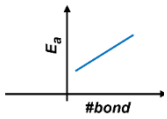
Broken bond (KRA)	$E_a = \frac{1}{2}\Delta E + \frac{1}{2}(n^i_{Pt-Pt} + n^f_{Pt-Pt})E_{Pt-Pt} + \frac{1}{2}(n^i_{Pt-Ni} + n^f_{Pt-Ni})E_{Pt-Ni} + \frac{1}{2}(n^i_{Ni-Ni} + n^f_{Ni-Ni})E_{Ni-Ni}$	$E_{Pt-Pt} = 0.097$ eV $E_{Pt-Ni} = 0.067$ eV $E_{Ni-Ni} = 0.066$ eV	
Parabolic potential	$E_a = \begin{cases} 0, & \Delta E < -4b \\ \frac{(\Delta E + 4b)^2}{16b}, & -4b \le \Delta E \le 4b \\ \Delta E, & \Delta E > 4b \end{cases}$	$b = 0.628$ eV	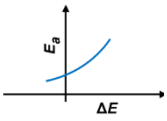
Constant activation energy	$E_a = \begin{cases} c, & \Delta E < 0 \\ c + \Delta E, & \Delta E \ge 0 \end{cases}$	$c = 0.510$ eV	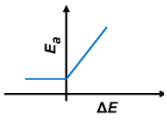
Weighted average	$E_a = fE_a^{\mathrm{CE}} + (1-f)E_a^{\mathrm{parabolic}}$	$f = 0.75$	

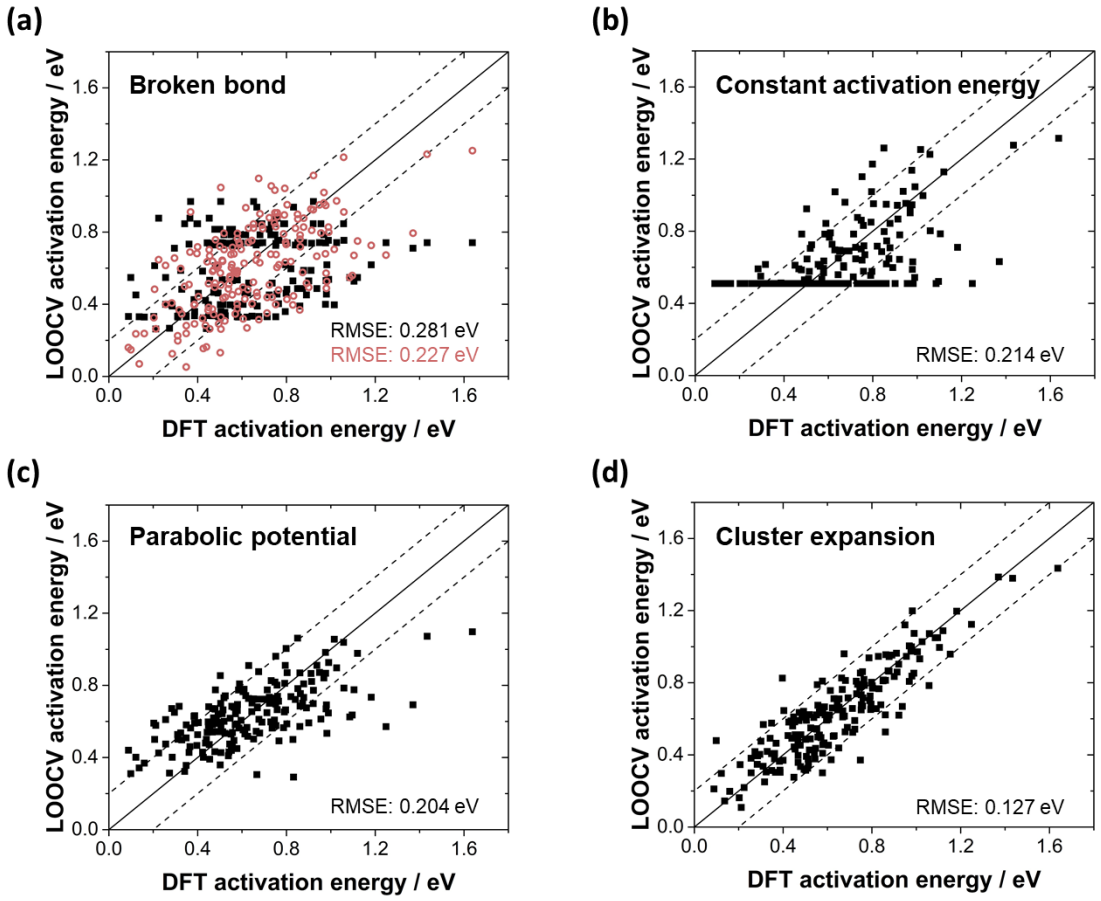

Figure 13. Leave-one-out cross-validation (LOOCV) of the activation energy from the four methods against the known DFT activation energy in the training set. In a) the black and red data points are the simple broken bond and the KRA broken bond model, respectively. The dashed lines indicate ± 0.2 eV deviation from perfect agreement.

The relative accuracies of different models are discussed in this section. It is found that the simple broken bond model has the largest root-mean-square LOOCV error (0.281 eV), followed by the KRA broken bond model (0.227 eV), the constant activation energy model (0.214 eV), the parabolic potential model (0.204 eV), and the cluster expansion (0.127 eV) (Figure 13). All the reported values here are the leave-one-out cross-validation error. The success of the cluster expansion is due largely to the fact that it is systematically improvable and includes far more parameters (1097 for cluster expansion) than the other simpler

models. Because the simple broken bond model only captures the nearest-neighbor environment around the initial state of the diffusing atom and its functional form establishes an upper bound for the activation energy (about 1 eV), it predicts many hops with identical activation energies regardless of the end states and it underestimates the activation energies for many hops with large activation energies. The KRA broken bond model is significantly more accurate (about 20%) than the simple broken bond model, likely because it does take into account the end states and makes the forward and reverse hops consistent. Moreover, because this model depends explicitly on the energy difference between the initial and final states, it does not impose an upper bound on the activation energy as the broken bond model does (Figure 13a). The constant activation energy model instead establishes a lower bound of the activation energy that is assigned to all downhill hops (Figure 13b). This causes overestimation and underestimation of small and large activation energies, respectively. The trend for the parabolic potential model (Figure 13c) is much better, although it still significantly overestimates and underestimates some small and large activation energies, respectively.

It is often possible to create a linear combination of multiple models to create a new model with improved predictive accuracy, an approach generally known as ensemble learning or stacked ensemble.[200] To explore this approach, a model consisting of a weighted average of the cluster expansion and the parabolic potential model is constructed (Table 3). The relative weights of the two models were determined in a way to minimize the leave-one-out cross-validation (LOOCV) error:

$$\sqrt{\frac{1}{N}\sum_{i=1}^{N}\left(y_i-\sum_{j=1}^{n}w_j\hat{y}_{ij}\right)^2},\ s.t.\ \sum_{j=1}^{n}w_j=1, \tag{26}$$

where N is the number of entries, n is the number of base models (here $n = 2$), w_j is the weight for the j^{th} model, $\hat{y}_{ij}$ is the cross-validation value of entry i from the j^{th} model, and y_i is the true (DFT) value of entry i.

Note that the weights determined this way, 0.75 for the cluster expansion and 0.25 for the parabolic potential model, are similar to what would have obtained using inverse variance weighting[201] (0.72 for the cluster expansion and 0.28 for the parabolic potential model), using the LOOCV errors to estimate the variance. The newly constructed weighted average model further lowers the LOOCV error by 10% (13 meV) relative to cluster expansion itself. This can be understood by the fact that these two models have error distributions that are largely uncorrelated due to their highly different formalisms (Figure 15).

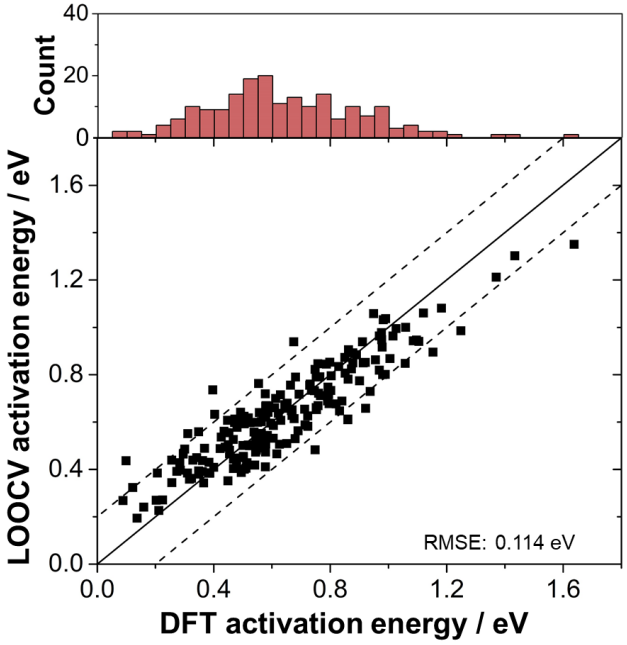

Figure 14. Leave-one-out cross-validation (LOOCV) of the activation energies from the weighted average model against the known DFT activation energies. The dashed lines indicate ± 0.2 eV deviation from perfect agreement. The upper panel shows distribution of the activation energy in the training set.

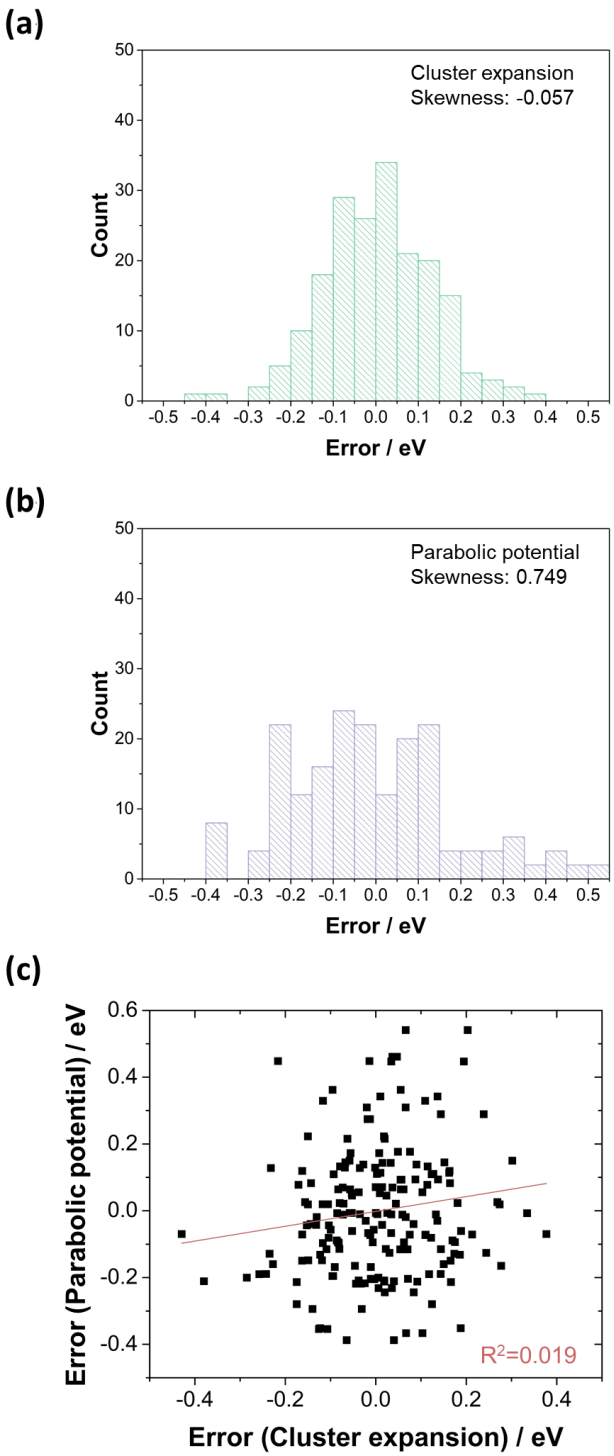

Figure 15. (a, b) Distributions of the leave-one-out cross-validation errors for the cluster expansion and the parabolic potential model, respectively. (c) A scatter plot of the leave-one-out cross-validation errors for the cluster expansion and the parabolic potential model, which shows the lack of correlation.

4.3.2 Test set performance

The improved performance of the cluster expansion comes with additional computational cost, both in terms of training set size and execution time. To assess the effect of training cost, the accuracy of the different methods has been evaluated as a function of training set size by randomly partitioning the data set into training sets and test sets, with models trained on the training sets and evaluated using the test sets (not trained on). Test sets are randomly chosen to contain 20% of the total amount of data, so the largest training set size considered here is 80% of the total data. The evaluation is repeated 10 times to calculate the average root-mean-square test error. The procedure is then repeated using randomly-selected training sets that are 80%, 60%, 40%, and 20% as large as the first training set. The averaged test set root-mean-square errors for the 10 different runs at each size are shown in Figure 16, with the standard deviations colored as shaded regions.

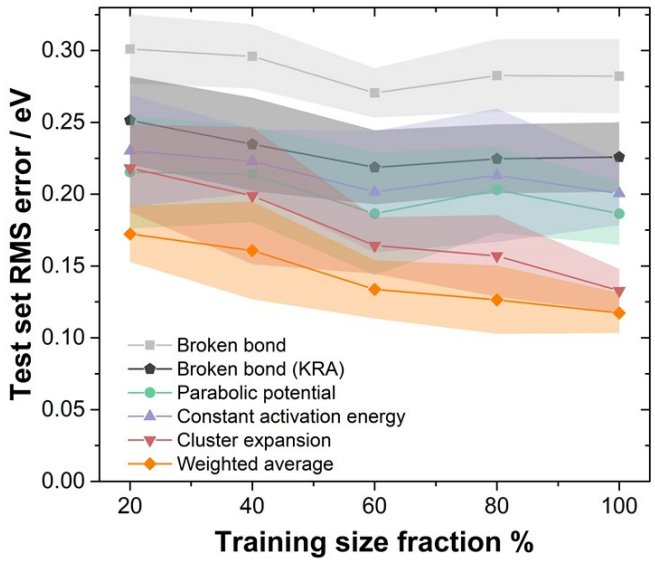

Figure 16. Test set root mean square (RMS) error as a function of training set size, expressed as a percentage of the remaining data set (excluding the test set) of 234 structures.

For the cluster expansion, it is observed that the test set errors decrease significantly with increasing training set size, whereas for the two broken bond models, the constant activation energy model, and the parabolic potential model, test set errors remain relatively constant with increasing training set size (Figure 16). This could be rationalized by the more flexible form of the cluster expansion compared to the simpler models (Table 3) discussed previously. These results indicate that when relatively small amount of training data is available, the parabolic potential, the constant activation energy, or the KRA broken bond model can predict activation energies with accuracy comparable to the cluster expansion, but since higher accuracy is often times desired especially for kinetic properties, the cluster expansion would be a better choice since it can be improved systematically via the generation of additional training data. The weighted average model has the lowest prediction error at every training set size and is an appealing approach especially for small and maybe medium training set sizes. For the system considered here, the weighted average model achieves the same level of accuracy as the cluster expansion with only about 60% of the training data (Figure 16). The model execution time will be discussed in the next section in the context of KMC simulations.

4.3.2 Structural evolution in KMC

To investigate how the different models may affect the structural evolution of a Pt_3Ni nanoparticle and how the model execution speed compares, KMC simulations have been performed on a truncated octahedral Pt_3Ni nanoparticle with random initial atomic order ($Pt_{3411}Ni_{1137}$, diameter of approximately 6.2 nm) at 1000 K. The elevated temperature was

chosen to accelerate dynamics and reduce the computational cost of the KMC simulations. In a typical KMC simulation, atoms were only allowed to hop into neighboring vacant sites, and the activation energy was computed using different models. The Ni dissolution was also considered, as significant Ni loss has been observed experimentally.[76, 140, 202] The Ni dissolution was only allowed from surface sites with a coordination number less than 10, and as long as all of the neighboring atoms were left with at least 3 nearest-neighbor atoms after Ni dissolution. For simplicity, for all models a zero activation energy was assigned to Ni dissolution, which generally occurs readily from the surface of the nanoparticle.[140] The snapshots of the Pt-Ni nanoparticles after the KMC simulation are shown in Figure 17.

The evolution of Ni composition in the first (outermost) layer is largely similar for the cluster expansion, the parabolic potential model, and the constant activation energy model (Figure 17f), where a Pt-rich shell of the nanoparticle is formed, which agrees with the previous KMC work and experimental work.[76, 140] The simple broken bond model produces a higher Ni composition in the first layer than that of the other models but with the lowest overall Ni composition (Figure 17g), indicating that the Ni atoms are exchanged more rapidly from inner layers to the surface of the nanoparticle and subsequently dissolved. The KRA broken bond model, however, shows completely different kinetics from the simple broken bond model, with a faster and more complete formation of a Pt shell and Pt(111) facet. This is likely due to the fact that the KRA broken bond model satisfies detailed balance, resulting in a more effective evolution toward a lower energy state.

Interestingly, the overall Ni dissolution rate (Figure 17g) largely follows the trend of the prediction errors of the models studied here. The simple broken bond model has the largest error and the cluster expansion has the smallest, with the parabolic potential model and the

constant activation energy model in between (see Figure 13). The large prediction error of simple broken bond model and its problem regarding detailed balance could be responsible for promoting more hops with unfavorable change in energy, thus creating more defects and a more porous structure (Figure 17d) than other models. Gorbatov *et al.* showed that it is necessary to include up to 4-body ECI for a different system, Al-Cu.[203] The less accurate models, such as broken bond models and constant activation energy model, may have less spread in the predicted activation energies and therefore may artificially accelerate rare events that could lead to Ni segregation to the surface.

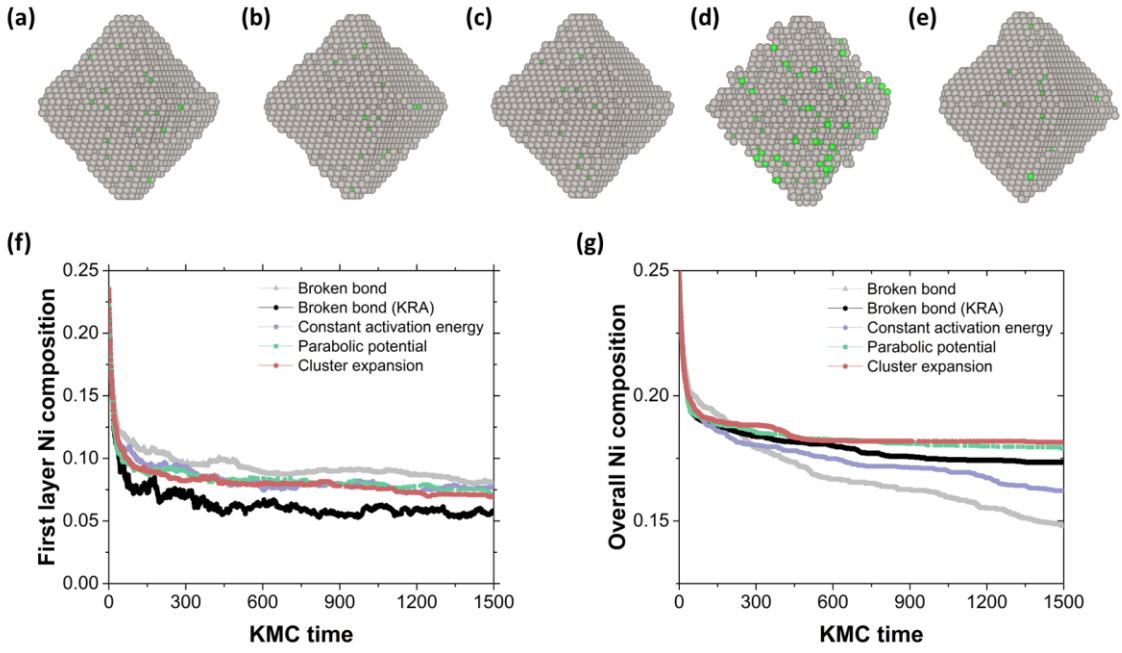

Figure 17. (a-e) Snapshots of Pt-Ni nanoparticles after the KMC simulations at 1000 K using (a) cluster expansion, (b) parabolic potential model, (c) constant activation energy model, (d) simple broken bond model, and (e) KRA broken bond model. (f, g) Profile of the first layer Ni composition and overall Ni composition from the KMC simulations.

Although the cluster expansion is much more accurate for predicting activation energies, it does not significantly affect the shape evolution of the Pt_3Ni nanoparticle compared to

the parabolic potential model or the constant activation energy model (Figure 17a-c, Figure 17f), except for the overall amount of Ni dissolution. The nearest-neighbor environments of Pt-Ni nanoparticles from five models are analyzed at the same overall Ni composition (18% Ni) from KMC simulations to provide more detailed information about the structures. The values for N_{Pt-Pt}, N_{Pt-Ni}, and N_{Pt-Vac}, measurements of the average numbers of Pt-Pt bonds, Pt-Ni bonds, and Pt-vacancy bonds around a Pt atom (see section 4.2.3), are almost identical for the cluster expansion, parabolic potential model and constant activation energy model, with the maximum difference being only about 0.19 (Table 4). These values are also comparable with the previous KMC work using the constant activation energy model.[76, 140, 189] Noticeably, the KRA broken bond model has the largest $N_{Pt-Pt} + N_{Pt-Ni}$ value, which is consistent with the less loss of the octahedral shape of the particle. It is worth noting that although the parabolic potential model has a prediction error similar to that of the constant activation energy model, its Ni composition profile is much closer to that of the cluster expansion. This could possibly be attributed to the more physically meaningful formalism of the parabolic potential model.

Table 4. The nearest-neighbor coordination environments of Pt-Ni nanoparticles averaged over five simulations at an overall Ni composition of 18% ($Pt_{3411}Ni_{748}$). N_{A-B} represents the average number of nearest-neighbor bonds around atom "A".

	N_{Pt-Pt}	N_{Pt-Ni}	N_{Pt-Vac}	N_{Ni-Pt}	N_{Ni-Ni}	N_{Ni-Vac}
Broken bond	7.98	1.91	2.11	8.73	2.56	0.71
Broken bond (KRA)	8.34	2.00	1.66	9.13	2.62	0.25
Constant activation energy	8.17	1.96	1.87	8.93	2.72	0.35
Parabolic potential	8.15	1.96	1.89	8.95	2.70	0.35
Cluster expansion	8.31	1.99	1.70	9.09	2.63	0.28

The simple broken bond model is the least accurate among the models, but it is much faster than the other models for calculating activation energies (by 3 orders of magnitude) since it only evaluates nearest-neighbor bonds, which is equivalent to a cluster expansion with only nearest-neighbor pair ECI (Table 5). All the other models calculate transition-state energies roughly equally quickly, as they all calculate activation energies (specifically, change in energies) using the complete cluster expansion, with 1097 ECI, to evaluate the energy difference between two different states. Further trimming of cluster expansion with $\sqrt{m_b V_b^2} < 10^{-4}$ eV could speed up the evaluation of the energies with little loss of accuracy (92 ECI removed); however, this speed-up is rather minimal compared to other routines in the KMC simulation.

Table 5. Average execution time for calculating the activation energy expressed relative to the time for the cluster expansion model.

	Relative time calculating activation energy
Broken bond	1.673×10^{-3}
Broken bond (KRA)	1.210
Parabolic potential	1.175
Constant activation energy	1.160
Cluster expansion	1

The overall time or speed of the KMC simulation depends on other routines in addition to calculating activation energies. In the KMC routine the total time consists of the time i) choosing a random event, ii) checking if the event is valid according to its neighbor environments, iii) calculating the activation energy and transition probability if the event

is valid, iv) updating the nanoparticle configuration if the event is accepted, and v) recording simulation data. It turns out that recording the nanoparticle configuration (in order to calculate Ni composition) after an accepted event takes up most of the computing time in this particular implementation, i.e. recording nanoparticle configuration scales with system size but calculating activation energy does not, which in turn makes the time for calculating activation energy effectively only a fraction of the total time. Also, steps i) and ii) take up about as much time as calculating the activation energy using the cluster expansion, thus, methods that calculate the activation energy significantly more quickly than the cluster expansion would have relatively little effect on the overall simulation time.

4.4 Discussion

The accuracy of modeling structural and kinetic evolution of the nanoparticle depends on the choice of the models, and the more accurate models can be computationally expensive. The simple broken bond model is fastest at calculating activation energy, but it results in a significantly different structural and kinetic evolution of the particle than the more accurate models. If no activation energy training data is available, the constant activation energy model would be the best option, as it calculates relative rates using only the difference in energy between the initial and final states. However, for the nanoparticle studied here, this model resulted in significantly faster nickel dissolution than the cluster expansion or the parabolic potential model. The parabolic potential model has a mean squared predictive error for activation energies that is similar to the constant activation energy model, but the kinetic evolution of the Pt-Ni nanoparticle predicted by the parabolic potential model is

more similar to the cluster expansion, which is the most accurate model. Note that these results may be particular to the system have studied here, and it is not clear to what extent they will generalize to other alloy systems. If larger amounts of training data (activation energies) can be generated, the transition-state cluster expansion provides the best results with no extra cost in terms of execution time. The weighted average approach can be used to further improve the predictive power or used as a way to reduce the cost of generating the training data. The transition-state cluster expansion may be particularly useful in other situations in which highly accurate activation energies are desired, such as the kinetic modeling of a chemical reaction on a catalytically active surface. The transition-state cluster expansion could also be used to study more complicated diffusion mechanisms such as a collective hop in which multiple atoms move simultaneously along the diffusion path, which might be challenging to model accurately using simpler approaches.

5. Au Nanorods

5.1 Background and motivation

5.1.1 CO_2 reduction

The advance of CO_2 electrocatalysis has recently attracted great attention as a sustainable way to synthesize liquid chemicals and fuels (e.g. by converting CO_2 to CO).[204-205] Among the metals known for catalyzing CO_2 reduction efficiently to CO, gold and its alloys (e.g. Au-Cu and Au-Pd) especially in nanoscale, have been shown to exhibit excellent activity and selectivity,[131, 133, 206-213] which could be appealing from a techno-economic point of view.[214-216] To allow for the design of Au-based catalysts, fundamental understanding of the reaction mechanisms and the catalytically active sites is necessary from both experiment and theory. A generally accepted type of active sites for the fcc crystals (from organic synthesis) is the under-coordinated sites both experimentally and theoretically.[208-209, 217-218] However, the exact CO_2 reduction mechanisms and/or rate-limiting steps are still under debate from experimental experts,[219-222] such as steps of electron transfer to CO_2, CO_2 to form *COOH intermediates, or *COOH to form *CO intermediates.

Even though the active sites are believed to be associated with the undercoordinated edge sites to some extent, designing a nanocatalyst with these sites being dominant and well-controlled on the surface remains quite challenging from experiments. Recently, the development of phase engineering of nanomaterials (PEN) by Zhang and co-workers has enabled the synthesis and design of a wide range of metals with unusual crystal phases, such as 4H (hexagonal) and hcp.[223-225] Nanostructures of such crystal phases preferentially expose unique surface sites such as the $(1\bar{1}00)_{4H}$ ridge sites and the $(11\bar{2}0)_{4H}$ ridge sites, which have greatly motivated this work on the understanding of structure-property-

performance relationship in nanocatalysts of the 4H phase for the electrocatalytic CO_2 reduction reaction (CRR).

5.1.2 Thesis research

In this work, three types of Au nanostructures have been studied: the 4H Au nanoribbon, the 4H Au nanorod, and the fcc Au nanorod, for CO_2 reduction. Cluster expansions[1-2] have been used to predict the atomic structures of the Au nanorods, with a comprehensive comparison with experimental characterizations using the high-resolution TEM and the Pb underpotential deposition (Pb_{upd}) techniques. Experimental work was done by the Wang group[2]. Further kinetic modeling has been performed to investigate the activity and selectivity of various surface sites on different Au nanostructures and it suggests that the excellent activity of the 4H phase could be possibly ascribed to the undercoordinated sites that are abundant and active on the 4H surfaces. This chapter is based in part on the published work in ref. 226 (Y. Wang[†] and C. Li[†] *et al.* Nano Lett., 2020).

5.2 Methodology

5.2.1 Cluster expansion for nanorod

To investigate the surface structures of Au nanorods, binary cluster expansions for fcc-Au nanorod and 4H-Au nanorod were generated based on the fcc and 4H lattice, where each

[2] Prof. C. Wang and his student Y. Wang.
[†] Equal contribution.

site can be occupied by either a gold atom or a vacancy. For the nanorods in this work, the vacuum space around the nanorods were represented by a collection of sites that are occupied by vacancies, allowing for the use of a training set consists of small (1~2 nm in diameter) nanorods to construct a cluster expansion that can be used to rapidly predict the energies and structures of larger nanorods with varying shapes and sizes. The cluster expansions were truncated to include the empty cluster, the single-site (point) cluster, all two-body (pair) clusters within a cutoff distance of 10 Å, all three-body clusters within a cutoff distance of 6 Å, and all four-body clusters within a cutoff distance of 3 Å, for a total of 28 and 110 symmetrically distinct cluster functions for the fcc-Au and 4H-Au cluster expansion, respectively. Training sets with 51 and 77 relaxed structures (fcc and 4H nanorods) by density functional theory (DFT)[84] calculations were generated and refined for fitting the ECI of the cluster expansions. The ECI for these cluster functions were fit to the training sets using the Bayesian approach.[67] The inverse of the covariance matrix for the prior was diagonal, with elements given by:

$$\lambda_{\alpha\alpha} = \begin{cases} 0, & n_\alpha = 0 \\ \lambda_1, & n_\alpha = 1 \\ \lambda_2 e^{\lambda_3 r_\alpha} e^{\lambda_4 n_\alpha}, & n_\alpha > 1 \end{cases} \tag{27}$$

where n_α is the number of sites in cluster function α, r_α is the maximum distance between sites, and λ_1, λ_2, λ_3, and λ_4 were determined using a conjugate-gradient algorithm to minimize the leave-one-out cross-validation (LOOCV) error, which is a measurement of the prediction error.[108] The resulting cluster expansions for fcc and 4H Au nanorods have LOOCV errors of 1.5 and 1.9 meV per atom, respectively.

5.2.2 DFT calculations

DFT calculations have been performed using the Vienna Ab initio Simulation Package (VASP)[85] with the revised Perdew-Burke-Ernzerhof (RPBE)[109, 114] and the PBEsol[227] exchange-correlation functional. Van der Waals interactions were accounted for by using the D3 correction,[228] and the VASPsol[229] implicit solvation model was used to treat the effect of aqueous solution on adsorption energies. The Au_GW, C_GW, O_GW and H_GW PBE projector-augmented wave (PAW)[110] potentials were used, and all VASP calculations were run with accurate precision. The Brillouin zone was sampled using efficient grids generated by the *k*-point grid server[111] with a minimum distance of 45.0 Å between adjacent points in real space lattice. Spin polarization was taken into account in the calculations and second-order Methfessel-Paxon smearing[112] with a width of 0.2 eV was used to set partial occupancies. Real space projectors were used to evaluate the non-local part of the PAW potential. The convergence criteria for the electronic self-consistent iteration and the ionic relaxation loop were set to be 10^{-4} eV and 10^{-3} eV per cell, respectively. For Au nanorod cluster expansions and surface energy calculations, the PBEsol functional was used, as it is found to improve the equilibrium properties of solids and surfaces.[230] The convergence for surface energies and adsorption energies are 1 meV/Å^2 and 10 meV, respectively. The slabs are at least six layers thick, and the vacuum layers are at least 18 Å. Calculations in this work suggested that RPBE-D3 gives overbinding to CO compared to experimentally measured CO adsorption energy on Au(211), whereas RPBE has a closer agreement with experiments.[107, 231] However, it was found that RPBE-D3 gave closer agreements on the onset potentials (related to *COOH binding energies) with experiments from this and previous study.[107] Therefore, in the free

energy diagram the RPBE energies were used for *CO and RPBE-D3 energies were used for *COOH. The hydrogen (*H) adsorption energies were calculated using the RPBE exchange-correlation functional.

5.2.3 Monte Carlo simulation

Simulated annealing was used to find the equilibrium shapes of the fcc and 4H Au nanorods. For each system studied, Monte Carlo simulations[92] were run from a temperature that is high enough (2000 K), then decreased in steps by a factor of $4^{0.05}$ until room temperature. At each temperature, the number of Monte Carlo iterations was 50 times the number of sites in the supercell. Subsequent annealing was carried out by only allowing atoms to swap on the surface of the nanorods. The number of iterations was set to be 100 times the number of sites in the supercell. In this work the supercells were 6 nm long (in the growing direction) and 7 nm wide (the nanorods were 5 nm in diameter). The thermodynamically averaged properties, e.g. average fractions of sites, were recorded during the Monte Carlo sampling at room temperature (300 K).

5.2.4 Pb underpotential deposition

The difference in the underpotential shifts for Pb adsorbed at two different surface sites, ΔV, can be estimated using the difference between the DFT-calculated Pb adsorption energies, ΔE_{ad} as follows:[232]

$$\Delta V \approx \frac{-\Delta E_{ad}}{2e} \tag{28}$$

$$\Delta E_{ad} = E(\text{slab+Pb*}) - E(\text{slab}) - E(\text{Pb}^{\text{o}}) \quad (29)$$

where e is the elementary charge and the factor of 2 comes from the fact that Pb loses two electrons when it dissolves, and $E(\text{Pb}^{\text{o}})$ refers to the energy of bulk Pb (per atom). In this definition, more negative values indicate stronger Pb adsorption. For simplicity, here fairly dilute Pb concentrations were assumed, where each Pb atom had no Pb nearest neighbors on the surface; accounting for voltage effects and interactions between adsorbed atoms would provide more accurate estimates.[233] To estimate the fraction of sites corresponding to each Pb_{upd} peak, thermodynamically averaged percentages of each type of sites on the 4H and fcc nanorods were recorded during the Monte Carlo simulations.

5.3 Results and discussion

5.3.1 Nanorod structures

Cluster expansions[1-2] and Monte Carlo simulations[92] have been used to predict the atomic structures of the Au nanorods in the pure 4H (ABCB stacking) phase and the fcc (ABC stacking) phase at room temperature. The equilibrium structures at room temperature are shown in Figure 18a and Figure 18b with different facets and sites labeled.

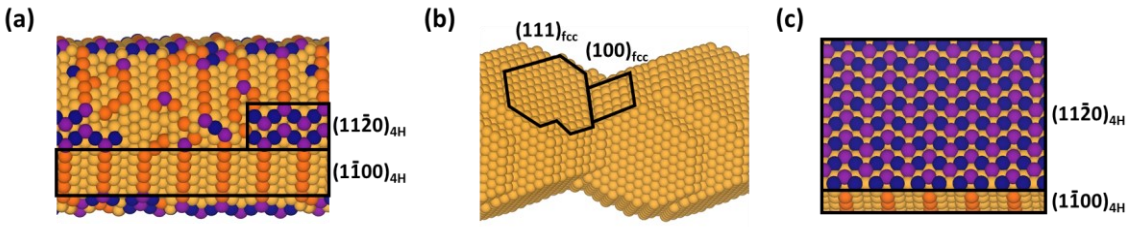

Figure 18. Cluster-expansion-predicted structure of a 4H-Au nanorod (a) and an fcc-Au nanorod (b) at room temperature. (c) A nanoribbon in the 4H phase. Orange, purple, and dark blue spheres denote $(1\,\bar{1}00)_{4H}$ ridge sites, ridge sites "*a*" of $(11\bar{2}0)_{4H}$, and ridge sites "*b*" of $(11\bar{2}0)_{4H}$, respectively. Atomic-scale structural images were generated using VESTA.[129]

For pure 4H Au nanorods, the cluster-expansion-predicted equilibrium surfaces comprise primarily of $(1\,\bar{1}00)_{4H}$ facets, which resemble a series of twinned (111) terraces. The $(11\bar{2}0)_{4H}$ facets are present in much smaller fractions, at the intersection of two $(1\,\bar{1}00)_{4H}$ facets only. The predicted shape agrees with the Wulff construction based on DFT-calculated surface energies (Figure 19 and Table 6). Pure fcc Au nanorods have mostly elongated (111) terraces, step edges, and edge sites at the intersections of the (111)/(111) and (111)/(100) facets (Figure 18b). The Monte Carlo simulations suggest that surfaces with the (211) orientation are likely to reconstruct so that they contain regions with extended (111) terraces, which is further supported by DFT calculations of the formation energies (Figure 20). This is also consistent with the surface structure of ultrathin fcc Au nanorod observed by Yang and co-workers.[234] Because of the "ABCB" stacking of the 4H-Au nanorods, there would be effectively a twin boundary (or "kink") appearing every four layers, thus they cannot have such extended (111) terraces as seen in fcc-Au nanorods and there is likely a higher fraction of undercoordinated sites on the surface of 4H nanorods

than fcc nanorods. The 4H-Au nanoribbon is modeled as a $(11\bar{2}0)_{4H}$ slab with a width and thickness of about 20 nm and 2.5 nm (Figure 18c) in accordance with ref. 235; the sidewall surface is $(1\,\bar{1}00)_{4H}$.

Table 6. DFT-calculated surface energies in this work. The "-rec" denotes a reconstructed surface with a missing row, and "-rec2" denotes a reconstructed surface with two missing rows.

	Surface energy (meV/Å^2)
(100)	72.42
(110)	76.02
(110)-rec	71.41
(110)-rec2	70.03
(111)	60.71
(211)	70.17
(211)-rec	69.02
(311)	74.01
(311)-rec	73.11
(322)	65.10
(332)	64.04
4H$(1\,\bar{1}00)$	61.78
4H$(11\bar{2}0)$	75.91

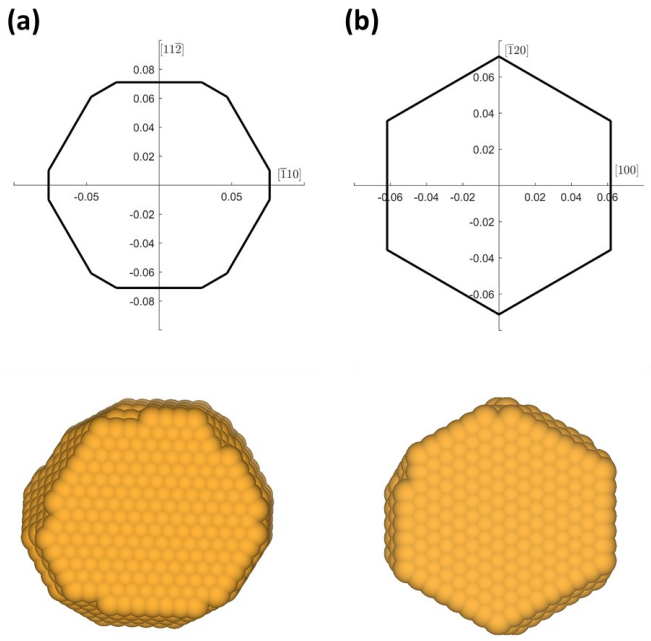

Figure 19. (Top) Wulff construction of (a) fcc, (b) 4H Au nanorod determined by DFT-calculated surface energies. (Bottom) Cluster-expansion-predicted equilibrium shapes of ~4 nm fcc and 4H nanorods. Atomic-scale structural images were generated using VESTA.[129]

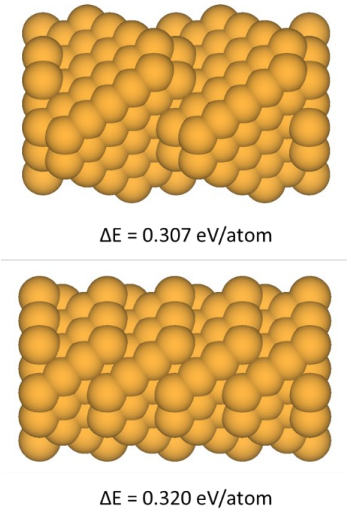

Figure 20. Two possible fcc-Au nanorod structures with 177 atoms per unit cell. (top) A cluster-expansion-predicted structure with (111) terraces. (bottom) A manually created structure having the same number of atoms per simulation cell but more (211) steps. DFT calculations indicate that the nanorod with more (111) terrace is more stable. The ΔE values are formation energy per atom relative to bulk Au.

5.3.2 Pb_{upd} analysis

The Pb underpotential deposition (Pb_{upd}) is an effective way to probe the surface structures of the Au nanocrystals by recording cyclic voltammograms in the presence of Pb^{2+}. The redox peak positions can then be correlated with the adsorption energies of Pb and the facets that Pb atoms adsorbed on.[210, 236-237] The experimentally measured Pb_{upd} peaks for three types of Au nanostructures are shown in Figure 21a. Comparing with the literature values for Au single crystals, the low-potential peak could be ascribed to the close-packed (111) facet (or terrace sites) of Au, whereas the high-potential peak is likely to be associated with the (110) facet or high-index facets abundant with undercoordinated sites.[236] DFT calculations of the Pb adsorption energies on the various types of Au surfaces have been performed and they correlate nicely with experimental trends, where Pb atoms generally bind to the close-packed (111) facet or terrace sites of Au less strongly than to the sites of open facets or the step edges (Figure 22 and Table 7).

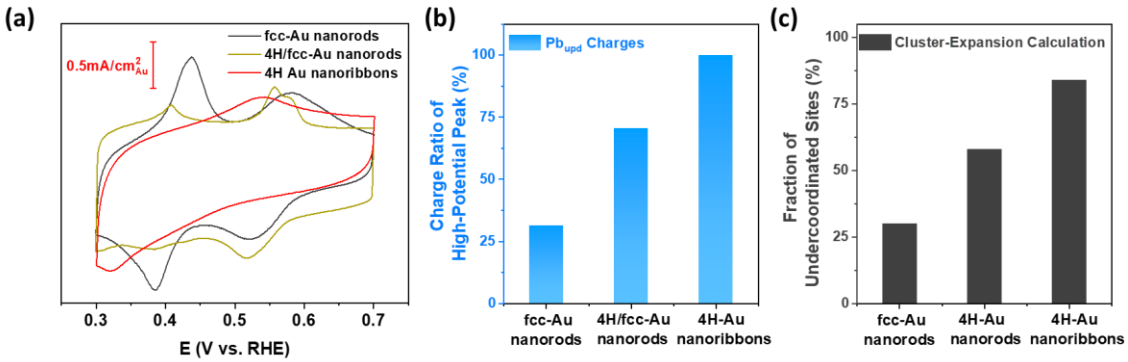

Figure 21. (a) Pb_{upd} profiles recorded on the three types of Au nanocrystals. (b) Fraction of charge associated with the high-potential peak in reference to the total Pb_{upd} charges. (c) Fraction of sites with relatively strong Pb adsorption, a measure of undercoordinated sites fraction, as determined by theoretical calculations on predicted Au nanostructures.

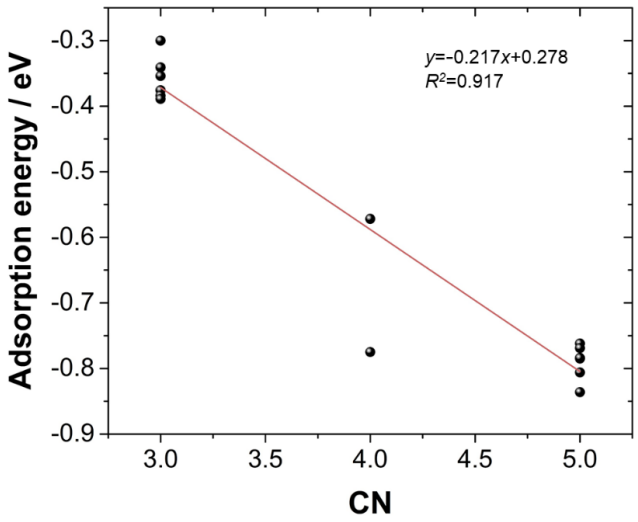

Figure 22. Correlation between the Pb adsorption energy and the coordination number (CN).

The relative area under the Pb_{upd} peaks can be interpreted as a measure of the fraction of the undercoordinated/terrace sites on the different Au nanostructures. (It should be noted explicitly that these are not direct measurements of the fractions of Au surface sites, but rather the Pb adsorption sites). From experiment, the 4H/fcc-Au nanorod, which is a mixed phase of 4H and fcc, exhibits a fraction of about 71% for the high-potential peak (Figure 21a, the right peak), which could be assigned to the stronger adsorption sites of Pb with coordination number CN=4 and CN=5 according to DFT calculations (Figure 22 and Table 7).[226] The terrace sites with CN=3 have similarly weak adsorption energies compared to the (111); these sites could be assigned to the left peak in Figure 21a. The 4H $(1\,\bar{1}00)$ "valley" site in Table 7, accounting for about $1/4$ of the surface sites on the 4H nanorod, has a coordination number CN=4 and an intermediate adsorption energy. This suggests that the peak and shoulder on the right side of the 4H nanorod Pb_{upd} voltammetric profile

(Figure 21a) may correspond to adsorption sites with coordination numbers of 4 and 5, respectively. In contrast, the fcc-Au nanorod shows the opposite feature, having only a fraction of 31% for the high-potential peak (Figure 21b), indicating more abundant terrace sites on the fcc-Au nanorod surface compared to the 4H-Au nanorod and thus corroborates the extended (111) surface feature. The estimated fractions of sites for the three types of Au nanostructures are shown in Figure 21c.

Interestingly, the 4H-Au nanoribbon only exhibits one broad Pb_{upd} peak closer to the positions of the right peaks for the nanorods, which may suggest negligible exposure of (111) facet or terrace sites on the surface of the 4H-Au nanoribbon.[226] This is consistent with the fact that about 80% of the nanoribbon surface is the $(11\bar{2}0)_{4H}$ facet[235] and there are no sites that bind to Pb weakly on that facet according to DFT results (Table 7). The leftward shift of the right-most peak may be attributed to the increasing 4H feature of the surface from fcc-Au nanorod to 4H/fcc-Au nanorod and then to 4H-Au nanoribbon, as it loses features such as the (211) step/valley sites that bind Pb more strongly but do not exist on the 4H nanorod and 4H nanoribbon (it could exist on the 4H/fcc nanorod of the mixed phase). As mentioned in section 5.2.4, accounting for interactions between adsorbed atoms would result in more accurate estimates and explanations of the relative peak shifts. For example, from DFT calculations the Pb adsorption energy changes from –0.30 eV to +0.25 eV when the Pb coverage increases from dilute to a full monolayer on (111); whereas the adsorption energy on 4H $(11\bar{2}0)$ only changes from –0.77 eV to –0.68 eV and it is not clear what the maximum coverage is due to its unique surface structure. Constructing another cluster expansion model would be of help to resolve the remaining problem. Nonetheless, the DFT and Au cluster expansion models have provided great insights into the structures

of the Au nanocrystals. A summary of the estimated fractions of surface Pb sites assigned to the left/right Pb_{upd} peak on the fcc-Au nanorod, 4H-Au nanorod, and 4H-Au nanoribbon are provided in Table 8.

Table 7. DFT-calculated Pb adsorption energies at various sites on different Au facets at dilute concentrations, converted to peak positions relative to that of fcc(111) by considering the equation $Pb^{2+} + 2e^{-} \rightarrow Pb*$, coordination number (CN) and generalized coordination number (GCN)[238-242] of the Pb site. Black and gold spheres represent Pb and Au atoms, respectively.

	CN_{Pb} (GCN)	Adsorption energy / eV	Peak relative to (111) / V	Fraction of sites	Peak position	
(111)	3 (2.500)	–0.300	0	0.68 with (322) and (211) terraces[a]	Left	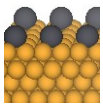
(322) terrace	3 (2.333)	–0.341	0.021	0.02	Left	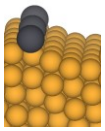
(322) terrace	3 (2.500)	–0.354	0.027	0.68 with (111)[a]	Left	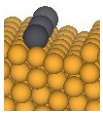
(322) terrace	3 (2.500)	–0.376	0.038		Left	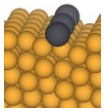
(211) terrace	3 (2.500)	–0.384	0.042		Left	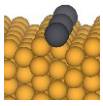
4H $(1\bar{1}00)$ terrace	3 (2.417)	–0.389	0.045	0.16 (ribbon) 0.42 (rod)	Left	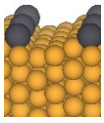

4H $(1\bar{1}00)$ valley	4 (3.500)	–0.572	0.136	0.08 (ribbon) 0.24 (rod)	Right	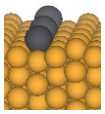
(322) valley	5 (4.000)	–0.762	0.231	0.12 with (211) valley[b]	Right	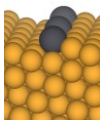
(100)	4 (3.000)	–0.775	0.238	0.16	Right	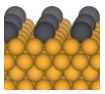
4H $(11\bar{2}0)$	5 (3.667)	–0.769	0.235	0.76 (ribbon)[c] 0.34 (rod)[c]	Right	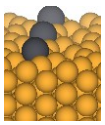
4H $(11\bar{2}0)$	5 (3.667)	–0.785	0.243		Right	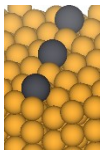
(110)-rec	5 (4.333)	–0.784	0.242	0.02	Right	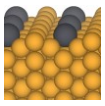
(211) valley	5 (4.000)	–0.806	0.253	0.12 with (322) valley[b]	Right	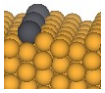
(110)	5 (3.667)	–0.836	0.268	0.00	Right	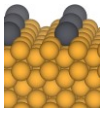

[a] Adsorption sites were classified by their coordination number and generalized coordination number, which is the same for each of these sites.

[b] Adsorption sites were classified by their coordination number and generalized coordination number, which is the same for these two sites.

[c] Adsorption sites were classified by their coordination number and generalized coordination number which is the same for these two sites.

Table 8. Fraction of surface Pb sites that assigned to left/right Pb_{upd} peak on the fcc-Au nanorod, 4H-Au nanorod, and 4H-Au nanoribbon.

	fcc-Au nanorod	4H-Au nanorod	4H-Au nanoribbon
Left peak (CN=3)	0.70	0.42	0.16
Right peak (CN=4)	0.16	0.24	0.08
Right peak (CN=5)	0.14	0.34	0.76

5.3.3 Free energy diagram and kinetic model

After successfully investigated the structures of the Au nanocrystals, the CO_2 reduction activity will be discussed in the following sections. To predict the relative activities of the different Au nanocrystals for CO_2 reduction to CO, the adsorption free energies of *COOH and *CO on the various sites on Au facets were calculated, as the *COOH and *CO are believed to be the key intermediates involved in this reaction, namely $CO_2(g) \rightarrow$ *COOH $\rightarrow$ *CO $\rightarrow$ CO(g).[103, 107, 208, 243-244] The free energy change of the intermediates at zero potential can be expressed as:

$$\Delta G = \Delta E_{DFT} + \Delta ZPE - T\Delta S + \Delta \int_{T'=0}^{T} C_p dT' \quad (30)$$

where ΔE_{DFT} is the electronic energy for the intermediate step of the CO_2 reduction from DFT calculations, ΔZPE is the difference in zero-point energies for a certain reaction, ΔC_p is the difference in constant-pressure heat capacity, ΔS is the change in entropy (Table 9). At an applied potential U, the change in free energy is shifted by $-neU$ according to the computational hydrogen electrode (CHE):[138]

$$\Delta G(U) = \Delta E_{DFT} + \Delta ZPE - T\Delta S + \Delta \int_{T'=0}^{T} C_p dT' - neU \quad (31)$$

where n is the number of ($H^+ + e^-$) transferred. All electronic energies are referenced to the corresponding Au clean slab, graphene (C), H_2 and H_2O. For example, the adsorption energy of CO can be calculated as:

$$\Delta E_{DFT}(*CO) = E_{DFT}(slab*CO) - E_{DFT}(slab) - E(C) - (E(H_2O) - E(H_2)) \quad (32)$$

Table 9. The zero-point energy (ZPE) corrections, entropy (TS) corrections, and enthalpic temperature corrections for adsorbates and non-adsorbates. The values are taken from the work of Peterson *et al.* at 291.65 K.[103] A correction of 0.32 eV for the free energy of CO_2(g) by Cao *et al.*[107] was applied due to errors in DFT-calculated reaction enthalpies compared to experimentally measured enthalpies.

	ZPE / eV	TS / eV	$\int C_p dT$ / eV
*CO	0.192	0.153	0.076
*COOH	0.624	0.178	0.096
*H	0.160	0.007	0.005
CO	0.14	0.60	0.09
CO_2	0.31	0.65	0.10
H_2	0.27	0.39	0.09
H_2O	0.58	0.65	0.10
C	0.13	0.02	0.026

It was assumed that the first step of proton and electron transfers to form *COOH were simultaneous,[103, 245] and the calculations herein showed that $*CO_2^-$ cannot be stabilized in either implicit solvent or explicit solvent (CO_2+Na+8H_2O). A recent study by Dunwell *et al.* also suggested that the electron transfer (ET) is unlikely to be the rate-limiting step on Au surfaces.[221] Thus, a two-step kinetic model (also accounting for *CO desorption in aqueous solution) is constructed:

$$CO_2(g) \rightarrow *COOH \rightarrow *CO \rightarrow CO(aq) \rightarrow CO(g) \quad (33)$$

where CO(aq) indicates a single CO molecule desorbed from the Au surfaces in aqueous solution, as described in the work by Cao *et al.*[107] to effectively serve as a kinetic barrier. The four intermediate reaction steps are:

$$CO_2(g) + 2(H^+ + e^-) \rightarrow *COOH + (H^+ + e^-) \quad (34)$$

$$*COOH + (H^+ + e^-) \rightarrow *CO + H_2O \quad (35)$$

$$*CO + H_2O \rightarrow CO(aq) + H_2O \quad (36)$$

$$CO(aq) + H_2O \rightarrow CO(g) + H_2O \quad (37)$$

There exists a roughly linear relationship[107, 244, 246] between G(*COOH) and G(*CO) on various facets that have been investigated (Figure 23). Using this linear relationship, the activation energies for equations (34-37) can be simplified as a function of the CO binding free energy G(*CO). To account for the kinetic barriers for the first step, an extra 0.18 eV is added, i.e. ΔG_a(*COOH) = ΔG(*COOH) + 0.18 eV, based on previous work on copper surfaces.[247] The changes in free energies as a function of potential for the above four steps are:

$$\Delta G_1(U) = G_a(\text{*COOH}) - G(\text{CO}_2) + eU = 0.448\Delta G(\text{*CO}) + 0.472 + eU \quad (38)$$

$$\Delta G_2(U) = G(\text{*CO}) - G_a(\text{*COOH}) + eU = 0.552\Delta G(\text{*CO}) - 0.472 + eU \quad (39)$$

$$\Delta G_3(U) = G(\text{CO}(aq)) - G(\text{*CO}) = 0.574 - \Delta G(\text{*CO}) \quad (40)$$

$$\Delta G_4(U) = G(\text{CO}(g)) - G(\text{CO}(aq)) = 0.119 - 0.574 = -0.455 \quad (41)$$

Therefore, a measure of catalytic activity can be defined as the negative of the maximum activation barriers:

$$\begin{aligned} \text{Activity} &= -\max(\Delta G_1(U), \Delta G_2(U), \Delta G_3(U), \Delta G_4(U), 0) \\ &= -\max(0.448\Delta G(\text{*CO}) + 0.472 + eU,\ 0.574 - \Delta G(\text{*CO}),\ 0) \end{aligned} \quad (42)$$

All adsorption energies were computed using the implicit solvation model (VASPsol).[229] The free energies of *COOH and *CO shown in Figure 23 are from the lowest-energy adsorption sites on each type of surfaces, i.e. the step edge sites on fcc and the ridge sites on 4H (note there are two types of ridge sites "*a*" and "*b*" on 4H $(11\bar{2}0)$ shown below). In the experiments, the partial pressure of CO is typically low (lower than ~1000 Pa),[226] which results in a lower free energy for CO(g) than *CO and facilitates CO desorption, validating the assumption of dilute *CO coverage in the calculations.

Table 10. Comparison of CO_2 adsorption on Cu and Au. The CO_2 was found to be unstable on Au(111). The only bent $*CO_2^{\delta-}$ structure on Cu(111) was obtained using PBE functional (in bold).[248-250]

	Cu(111)			Au(111)	
	Charge on $*CO_2$	O-C-O bond angle (°)		Charge on $*CO_2$	O-C-O bond angle (°)
PBE	**–0.81**	**130.5**		–0.03	177.9
RPBE	–0.12	171.8		–0.04	176.6
RPBE-D3	–0.12	173.7		–0.07	176.6

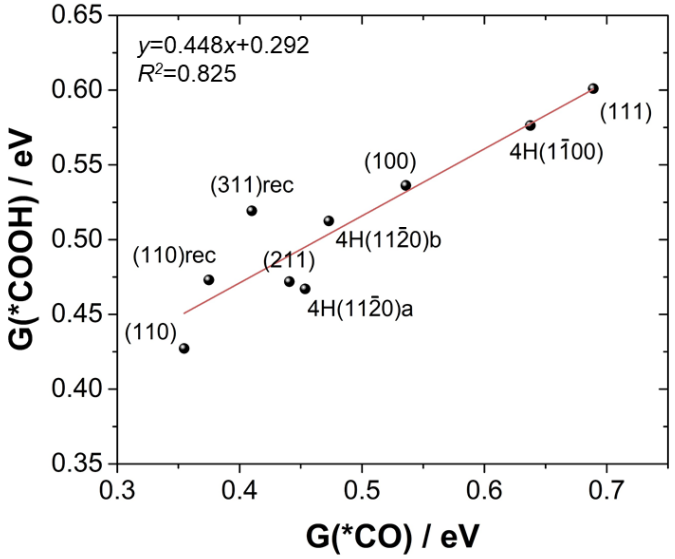

Figure 23. The linear relationship between G(*COOH) and G(*CO). The "4H$(11\bar{2}0)$ a" and "4H$(11\bar{2}0)$ b" are the ridge site "a" and ridge site "b" on this 4H facet. The "4H$(1\,\bar{1}00)$" is the ridge site on this 4H facet. "(110)", "(110)rec", "(211)", and "(311)rec" indicate the edge sites on these facets. These are the sites on each facet on which G(*CO) is lowest.

5.3.4 Activity and selectivity

To calculate the average activity for the Au nanostructures based on the kinetic model, a thorough exploration of all possible surface sites on the fcc and 4H nanostructures has been performed. For each site on the surface, the following equation is used to determine the CO_2 reduction current:

$$j \propto \exp(-\max(\Delta G(\text{*COOH}) + 0.18 + eU,\ 0.574 - \Delta G(\text{*CO}),\ 0) / k_B T) \quad (43)$$

where ΔG(*COOH) and ΔG(*CO) are adsorption energies at a specific site, and U is the applied potential. For commonly occurring sites, the DFT-calculated free energies of the *COOH and *CO are used. These free energies, as well as the coordination number (CN) and generalized coordination number (GCN)[238-242] of each site, are summarized in Table 11. For the surface site with both CN and GCN matching one in Table 11, DFT-calculated adsorption energies are used to evaluate equation (43). For the site that does not match one within Table 11, the *COOH and *CO adsorption free energies are estimated using a least-squares fit of DFT-calculated free energies against the CN of the adsorption site (Figure 24a and Figure 24b).

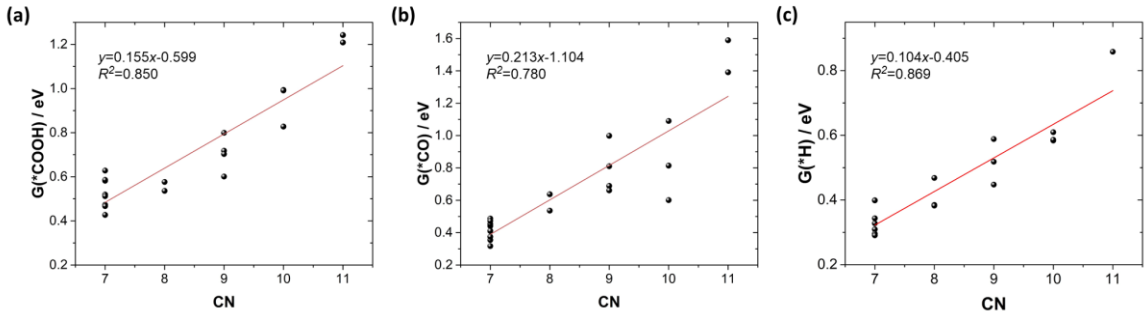

Figure 24. Least-squares fits of ΔG(*COOH), ΔG(*CO), and ΔG(*H) as a function of coordination number (CN).

Table 11. Generalized coordination number (GCN) and coordination number (CN) of Au, free energy of adsorption of *CO, *COOH, and *H, and fraction of sites on the 4H and fcc nanocrystals for all surface sites studied. Energies are relative to $G(CO_2(g))$. The suffix "-rec" indicates a reconstructed surface with a missing row. The "-rec2" indicates a reconstructed surface with two missing rows.

	GCN (CN_{Au})	G(*CO) / eV	G(*COOH) / eV	G(*H) / eV	Fraction	*CO	*COOH
(110)-rec edge	5.167 (7)	0.375	0.473	0.295	-	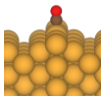	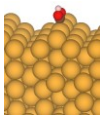
(110)-rec2 edge (111)/(111)	5.167 (7)	0.317	0.586	0.399	0.02	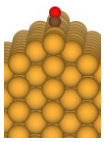	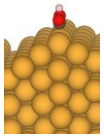
(311)-rec edge (111)/(100)	5.333 (7)	0.410	0.519	0.291	0.03	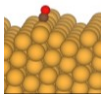	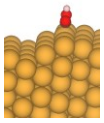
(211) step edge	5.500 (7)	0.441	0.472	0.309	-	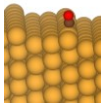	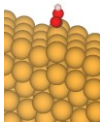
(322) step edge	5.500 (7)	0.411	0.582	0.328	0.02	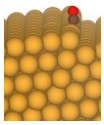	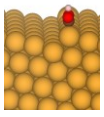
(110)	5.833 (7)	0.355	0.427	0.399	0.00	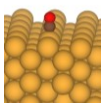	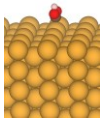
4H $(11\bar{2}0)$ ridge "*a*"	5.833 (7)	0.454	0.467	0.296	0.01 (rod) 0.21 (ribbon)	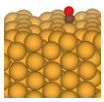	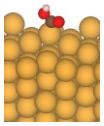
4H $(11\bar{2}0)$ ridge "*b*"	5.833 (7)	0.473	0.512	0.296	0.01 (rod) 0.21 (ribbon)	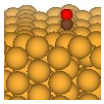	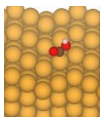
4H $(1\bar{1}00)$ ridge	6.333 (8)	0.638	0.576	0.468	0.12 (rod) 0.04 (ribbon)	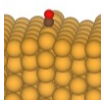	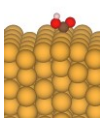

(100)	6.667 (8)	0.535	0.536	0.385	0.02	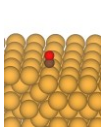	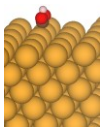
(211)-rec terrace (100) micro facet	6.750 (8)	0.661	0.674	0.383	0.02	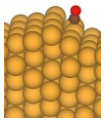	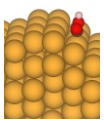
(110)-rec terrace	7.167 (9)	0.999	0.799	0.589	0.08	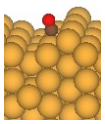	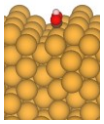
(111) terrace	7.500 (9)	0.689	0.601	0.447	0.35	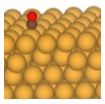	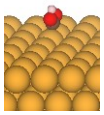
4H $(1\bar{1}00)$ terrace	7.500 (9)	0.811	0.703	0.518	0.14 (rod) 0.09 (ribbon)	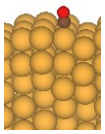	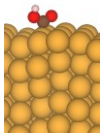
(211) valley	8.750 (10)	0.601	0.993	0.584	0.01	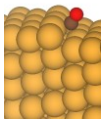	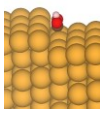
(311)-rec valley	8.833 (10)	0.815	0.991	0.586	0.01	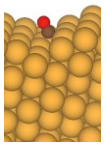	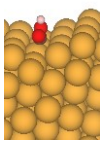
4H $(1\bar{1}00)$ valley	8.667 (10)	1.091	0.828	0.610	0.09 (rod) 0.04 (ribbon)	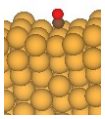	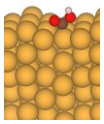
4H $(11\bar{2}0)$ valley "*a*"	9.167 (11)	1.391	1.242	0.858	0.01 (rod) 0.21 (ribbon)	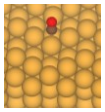	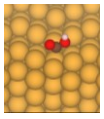
4H $(11\bar{2}0)$ valley "*b*"	9.167 (11)	1.589	1.209	0.858	0.01 (rod) 0.21 (ribbon)	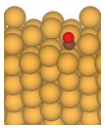	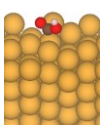

The surface areas of the Au nanostructures are estimated by:

$$A = \sum_i \left(\frac{A_i}{\#site_i} \right) f_{site_i} N_{site} \tag{44}$$

where $A_i / \#site_i$ is the area per site for site (facet) i, f_{site_i} is the fraction of site i, and N_{site} is the total number of surface sites. The fractions of different types of adsorption sites on the nanorods are estimated by counting the number of sites matching both the CN and GCN (Table 11). Summing up over the current contributed by all the surface sites and dividing by the surface area A yields the specific activity. Through this model it is predicted that the CO_2 reduction activity follows the trend of 4H nanoribbon > 4H nanorod > fcc nanorod. The enhancement of the activity for the 4H nanoribbon is about 3.3 and 23.7 times of that of 4H nanorod and fcc nanorod respectively (at –0.6 V), which is consistent with experiments.

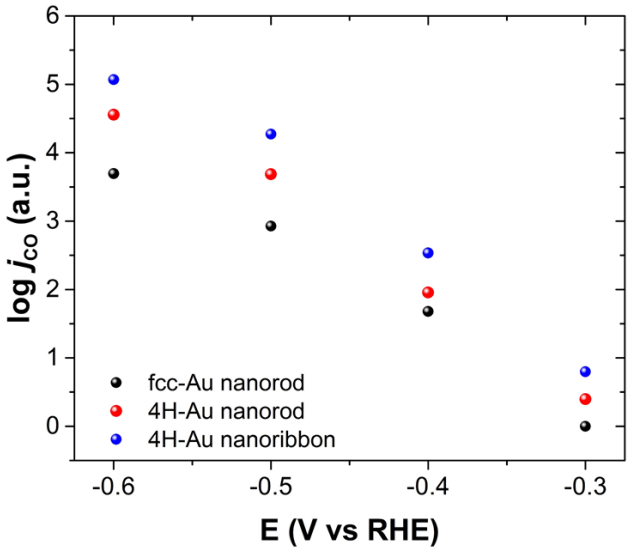

Figure 25. The CO specific activity as a function of potential for the fcc-Au nanorod, 4H-Au nanorod and 4H-Au nanoribbon, relative to that of fcc-Au nanorod at –0.3 V.

To further understand the selectivity of the synthesized Au nanocatalysts, the competing reaction, hydrogen evolution reaction (HER), is being evaluated. The rate-limiting step for the HER on Au, which binds hydrogen relatively weakly, is believed to be the Volmer step, in which a single hydrogen atom adsorbs on the surface. The most stable sites for *H are found to be the bridge sites except for the (111), where the fcc hollow site is the most stable site. The HER reaction pathway can be written as:

$$H^+ + e^- \rightarrow *H \rightarrow \tfrac{1}{2} H_2(g) \tag{45}$$

The kinetic barrier of the proton-electron transfer is expressed as ΔG_a(*H) = ΔG(*H) + 0.333 eV to map the adsorption free energy calculated in this work to the rate-limiting free energy barrier on Au(111) (0.78 eV) at 0 V vs the RHE based on the work by Lindgren *et al*.[170] Therefore, the HER activity can be calculated in a similar way:

$$\begin{aligned} \text{Activity} &= -\max(\Delta G(*\text{H}) + 0.333 + eU,\ -\Delta G(*\text{H}),\ 0) \\ &= -\max(\Delta G(*\text{H}) + 0.333 + eU,\ 0) \end{aligned} \tag{46}$$

No extra barriers are added to the H_2(g) liberation step here because of the largely positive adsorption energies of *H. The relative selectivity for the CO_2 reduction reaction (CRR), can be estimated by the difference in limiting potentials between the CRR and the HER.[251] Specifically,

$$\begin{aligned} &U_L(\text{CRR}) - U_L(\text{HER}) = \\ &\tfrac{1}{e}(-\max(\Delta G(*\text{COOH}) + 0.18 + eU, 0.574 - \Delta G(*\text{CO}), 0) + \max(\Delta G(*\text{H}) + 0.333 + eU, 0)) \end{aligned} \tag{47}$$

This can be simplified using the linear fits in Figure 24a-c to provide general trends in coordination dependence (Figure 26a) and can be plotted for the individual sites (Figure 26b and Figure 26c).

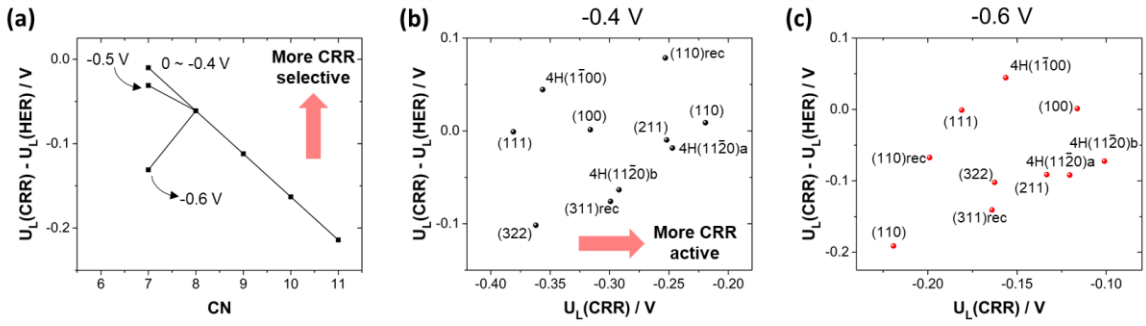

Figure 26. (a) Limiting potential difference $U_L(\mathrm{CRR}) - U_L(\mathrm{HER})$ as a function of coordination number (CN). (b-c) Limiting potential difference as a function of $U_L(\mathrm{CRR})$ at –0.4 V and –0.6 V, respectively. Top right region indicates more selective and active for CO_2 reduction reaction (CRR). The "4H$(1\,\bar{1}00)$" is the ridge site on this 4H facet. "(110)", "(110)rec", "(211)", and "(311)rec" indicate the edge sites on these facets. These are the sites on each facet on which G(*CO) is lowest.

Consistent with the work by Back *et al.*,[251] the undercoordinated sites on Au nanocrystals should be expected to be more selective for CO production at moderate overpotentials, e.g. 0 ~ –0.5 V for sites with CN=7. Decreasing the potential down to –0.6 V, the sites with CN=8 have the highest selectivity and the CRR current for sites with CN=7 are expected to be saturated, on average (as is obtained from the linear fits), and thus a drop in selectivity is observed (Figure 26a). This is largely due to the weaker coordination-dependence of ΔG(*H) compared to that of ΔG(*CO) and ΔG(*COOH) (Figure 24).

For the individual sites on the top right region of Figure 26c, the 4H$(1\,\bar{1}00)$ ridge site, particularly abundant on the 4H nanorod, is both active and selective for CRR at –0.6 V. Some fcc sites are predicted to be similarly active and no less selective (e.g. (110)rec edge)

than the sites on the 4H $(11\bar{2}0)$ facet, but these sites are predicted to be far less abundant on the fcc nanorods than the 4H $(11\bar{2}0)$ sites on the 4H phases.

5.3.5 The active sites

The active sites for CRR at different overpotentials can be directly seen from a set of heat maps showing the model-predicted current density (Figure 27). The color scale is relative to that of the most active site for each overpotential. The relatively high activity of the 4H nanocrystals can be largely ascribed to the highly active and abundant 7- and 8-fold undercoordinated sites on their surfaces, i.e. the $(11\bar{2}0)_{4H}$ and $(1\bar{1}00)_{4H}$ ridge sites (Figure 28). Specifically, about 46% and 32% of the surface sites for 4H-Au nanoribbons and 4H-Au nanorods fall into this category of undercoordinated sites, respectively.

At small overpotentials (e.g. –0.4 V), the CO_2 reduction is limited by the activation and hydrogenation of CO_2 to form *COOH. At these potentials, 7-fold coordinated sites such as the ones on fcc(322), fcc(311), fcc(110)-reconstructed, and $(11\bar{2}0)_{4H}$ are the most active due to their ability to strongly bind *COOH (Figure 28b). In particular, the two ridge sites on $(11\bar{2}0)_{4H}$ retain high activity down to a potential of –0.6 V, explaining the superior performance of 4H-Au nanoribbons (and possibly 4H-Au nanorods). One of these sites, the ridge site "*a*" (as labeled in Figure 28), is predicted to be particularly active at small overpotentials (–0.4 V) because it exhibits the most favorable deviation from the scaling relationship between the binding energies of *CO and *COOH (Figure 28). The ridge site "*b*" of $(11\bar{2}0)_{4H}$ becomes the most active site when site "*a*" becomes CO desorption limited (–0.6 V). At potentials below –0.6 V, CO desorption is rate-limiting on both of the above

sites and 8-fold coordinated sites with slightly weaker binding to CO, such as fcc(100) and the ridge site of $(1\,\bar{1}00)_{4H}$, become more active (Figure 27c). This is due to the reduced energy barrier for CO_2 hydrogenation (due to stabilization of *COOH relative to CO_2) at more negative potentials, in combination with more facile CO desorption on such sites with relatively weak CO binding strengths.[226] At these potentials the $(1\,\bar{1}00)_{4H}$ ridge site is also predicted to be among the most selective sites for CRR, based on the calculated limiting potentials for CO_2 reduction and hydrogen evolution (Figure 26). Note that across the full potential range considered in experiments the most active sites on the fcc nanorods (step edges and (100) sites) are relatively rare compared to those on the 4H nanorods and 4H nanoribbons. The 9-fold coordinated sites on the close-packed (111) surfaces/terraces on fcc nanorods, which are the majority sites, remain relatively inactive due to their weaker binding of *COOH intermediates.

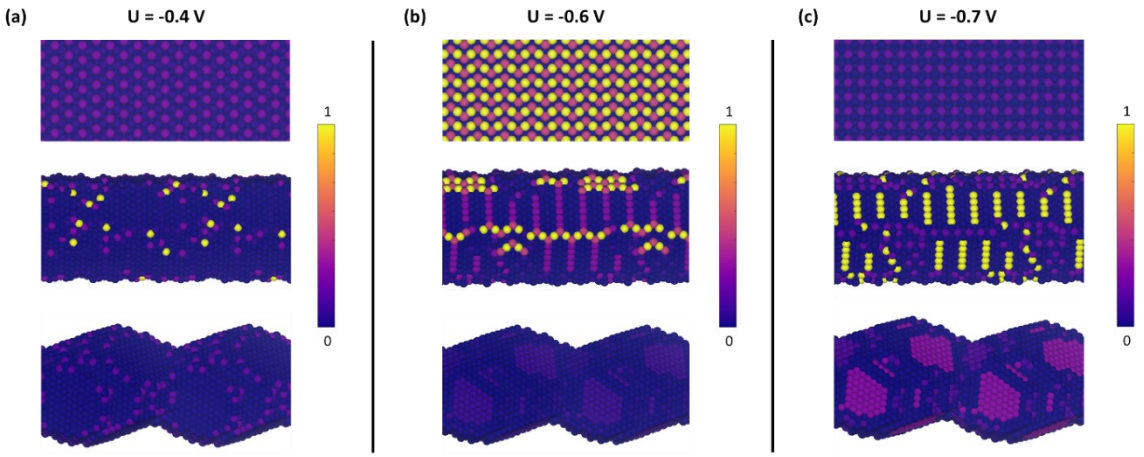

Figure 27. Predicted CO current density of all surface sites on 4H-Au nanoribbon, 4H-Au nanorod and fcc-Au nanorod, relative to the most active sites at (a) –0.4 V, (b) –0.6 V, and (c) –0.7 V. Atomic-scale structural images were generated using VESTA.[129]

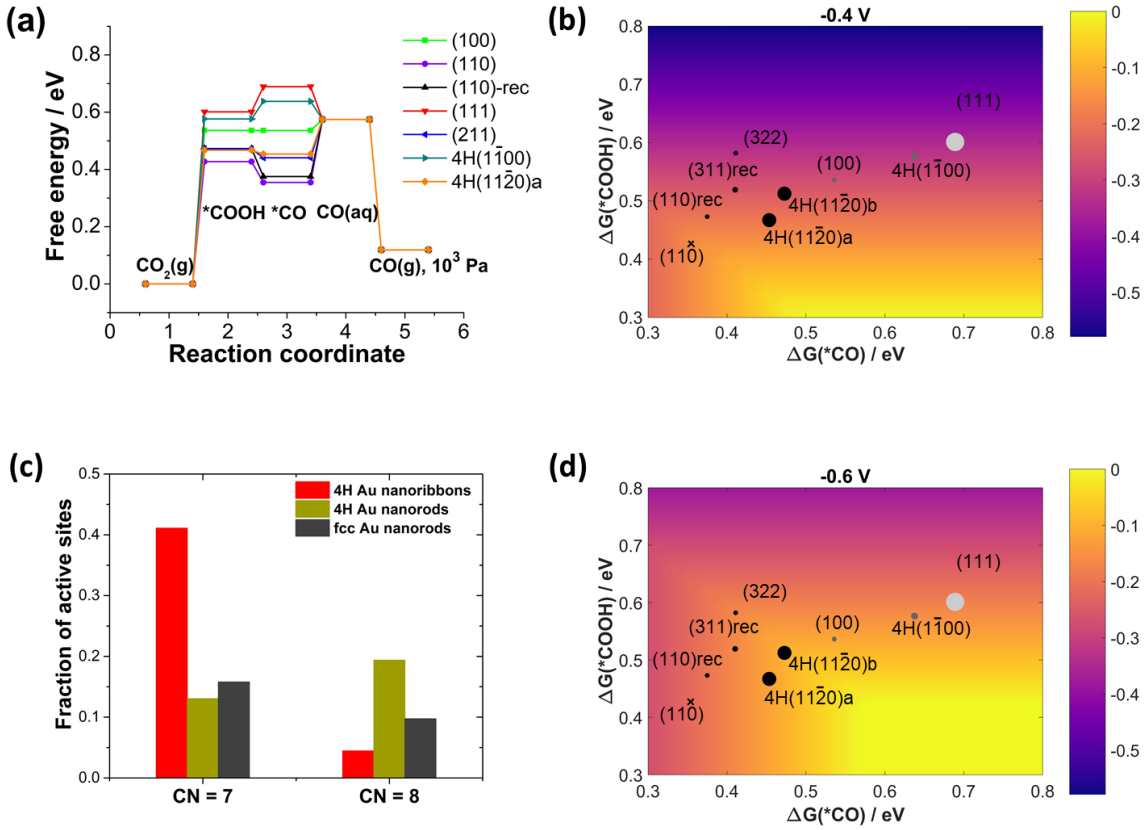

Figure 28. (a) DFT-calculated free energy diagram for CO_2 reduction to CO(g) at 0 V. CO(aq) represents a single CO molecule in aqueous solution.[107] (b) Trends in CO_2RR activity at –0.4 V as a function of ΔG(*CO) and ΔG(*COOH). The area of the marker indicates the relative fraction of the site type on the 4H nanoribbons and fcc nanorods, and "x" means zero fraction. Black, gray, and light gray circles indicate coordination number (CN) of 7, 8, and 9, respectively. (c) Predicted fraction of active sites with CN of 7 and 8 on Au nanocrystals. (d) Trends in CO_2RR activity at –0.6 V.

5.4 Summary and conclusion

In this work, cluster expansion and DFT modeling have been carried out to study structure-property relationships in Au nanocatalysts for CO_2 reduction with a direct comparison with experimentally characterizations, highlighting a computational framework of predicting surface structure and identifying catalytically active sites (and this should be particularly important for alloys as the surface structure can be different from the bulk). Consistent with

experiment, it is suggested that enhanced CO_2 reduction activity of the 4H-Au nanoribbons and 4H-Au nanorods could be ascribed to the formation of distinct and abundant undercoordinated sites on their surfaces. The creation of such surface sites in the 4H phase, which do not appear on fcc crystals, could provide a new strategy for rational design of CO_2 reduction electrocatalysts with similar surface structures. Introducing other metal epitaxial growth on the 4H-Au might open up new design strategies for future engineering of nanocatalysts as well.

6. Transition Metal Phosphide and Pt Surfaces

6.1 Background and motivation

6.1.1 Hydrogen evolution reaction

Hydrogen fuel cell technology is environmentally friendly as it only produces water as the chemical waste when it converts chemical energy to electricity and heat.[252] To power a hydrogen fuel cell, H_2(g) needs to be provided into the anode. The hydrogen evolution reaction (HER), half of the water splitting reaction, produces H_2(g) from renewable energy resources and thus can reduce the demand for fossil fuels and can become environmentally friendly as well.

For HER, in acid electrolytes protons are reduced to H_2 via $2H^+ + 2e^- \rightarrow H_2(g)$ and in base electrolytes via $2H_2O + 2e^- \rightarrow H_2(g) + 2OH^-$. Pt is found to be one of the most active catalysts for this reaction,[253-254] but due to its relatively high cost there is great interest in finding alternative catalysts (e.g. made of earth-abundant materials) that do not depend on expensive metals. A group of promising candidates is transition metal phosphide. Transition metal phosphides have emerged from both experimental and theoretical studies as active HER catalysts with good performance and relatively good stability.[255-262] As these metal phosphides consist of earth-abundant element such as Fe, Co, and Ni, they have the potential advantage of being more economically viable than Pt-based catalysts.

Computationally, it has been shown that the hydrogen adsorption free energy ΔG_H (more negative values indicate stronger adsorption) is a suitable descriptor of the catalytic activity for HER, and typically an adsorption free energy around 0 eV demonstrates higher activity.[254, 263-264] While numerous computational studies have found that ΔG_H is close to 0

on some sites on model transition metal phosphide surfaces, their catalytic activities still remains below that of Pt.[254-259, 264-267] If there exists a strong coverage dependence of ΔG_H, there would be a good chance that some of the sites have a $\Delta G_H \sim 0$ eV at some hydrogen coverages, which correspond to some applied potentials that need to be specified. Thus, the coverage effect and fundamental mechanisms should be understood to fully resolve this problem and provide more insights into designing active catalysts. In addition, there are evidences that the operating mechanism of the HER of the transition metal phosphides might be different from that of Pt:

- The hydrogen adsorption energy on transition metal phosphides has a strong coverage dependence compared to metals (e.g. ranging up to ~0.8 eV for Fe_2P), and the differences in ΔG_H between different sites on transition metal phosphide surfaces are large.[255, 259]
- On pure metal catalysts the hydrogen coverage can reach almost a full monolayer at small overpotentials, whereas on metal phosphides (and sulfides), the hydrogen surface coverages are much lower.[268-270]
- The Tafel slopes for transition metal phosphides, a measure of how the log of the current changes with the applied potential, are typically around 40~60 mV/dec, whereas that of Pt is around 30 mV/dec.[256-257, 260-262, 271]

6.1.2 Thesis research

To better understand the HER mechanisms on transition metal phosphide surfaces and how they compare to Pt, the cluster expansion approach[1-2] has been used to model realistic structures of hydrogen adsorption on the surfaces of transition metal phosphides and Pt. The cluster expansion is able to rapidly predict the energy of a particular arrangement of adsorbed H* on the surface of a material with high accuracy (on the order of a few meV per site), at the same time accounting for more accurate and realistic interactions between adsorbates, which could have dramatic effect on the catalytic activity.[272] For these reasons, there has been increasing interest in using cluster expansions to investigate heterogeneous catalysis.[38-39, 45, 50, 52-53, 57, 72, 76-79, 199, 273]

In this work, cluster expansions on four transition metal phosphide surfaces including FeP(011), Fe_2P(100), CoP(101), and Co_2P(101), have been generated, together with a Pt(111) surface for comparison purposes. The catalytically active sites and the reaction mechanisms are explored by using cluster expansions and Monte Carlo simulations. It is demonstrated that the effect of hydrogen coverage, interaction between adsorbed hydrogen atoms, and desorption kinetics all dictate the HER mechanisms and the active sites. The predicted mechanisms for transition metal phosphides and Pt are in good agreement with experimental studies. The challenge of using a simple descriptor for catalytic activity is further discussed. This chapter is based in part on the published work in ref. 272 (C. Li *et al.* Phys. Chem. Chem. Phys., 2019, 21, 24489).

6.2 Methodology

6.2.1 Cluster expansion

Surface cluster expansions have been generated to model the hydrogen adsorption on transition metal phosphide and platinum surfaces, where each possible adsorption site can exist in one of two states: occupied by hydrogen or vacant (+1 or −1 assigned to site variables). The Bayesian approach[67] was used to fit the cluster expansion to a set of DFT training data. The training sets contained structures with varying hydrogen coverages (0~1 monolayer) and supercell sizes, allowing for the rapid predictions of the energies and atomic orders of large-size supercells as a function of temperature and applied potential. The cluster expansions included the empty cluster, the one-body clusters, all two-body clusters within a cutoff distance of 8 Å, all three-body clusters within a cutoff distance of 4 Å, and all four-body clusters within a cutoff distance of 4 Å. The effective cluster interactions (ECI) for these cluster functions were fit to the DFT training data using the Bayesian approach[67] with a multivariate Gaussian prior distribution for the ECI values. The Bayesian approach has been shown to greatly improve the predictive accuracy of the cluster expansion for a given training set size.[53, 67, 72] The inverse of the covariance matrix for the prior distribution had elements of:

$$\lambda_{\alpha\alpha} = \begin{cases} 0, & n_\alpha = 0 \\ \lambda_1, & n_\alpha = 1, \\ \lambda_2 e^{\lambda_3 r_\alpha} e^{\lambda_4 n_\alpha}, & n_\alpha > 1 \end{cases} \tag{48}$$

where n_α is the number of sites in cluster function α, r_α is the cutoff distance, and the parameters λ_1, λ_2, λ_3, and λ_4 were determined using a conjugate gradient algorithm to

minimize the leave-one-out cross-validation (LOOCV) error. The resulting cluster expansions for $Co_2P(101)$, CoP(101), $Fe_2P(100)$, FeP(011), and Pt(111) have root mean square LOOCV errors of 3.4, 7.4, 7.0, 4.3, and 6.6 meV per site, respectively.

6.2.2 DFT calculations

Density functional theory (DFT)[84] calculations were performed with the Vienna Ab initio Simulation Package.[85] The revised Perdew-Burke-Ernzerhof (RPBE)[109, 114] exchange-correlation functional was used for all DFT calculations, as this resulted in the closest agreement with experimentally measured hydrogen adsorption energy on Pt(111) among RPBE, RPBE-D3 and PBE-D3, where D3 stands for the van der Waals correction method.[228, 274] Spin polarization was enabled. The Co, Fe, P, H_GW, Pt_pv PBE projector-augmented wave (PAW)[110] potentials were used and all calculations were run with accurate precision to ensure that there were no wrap-around errors. For calculations with transition metal phosphides, the slab thickness and vacuum thickness were at least 10 Å and 15 Å, respectively. The Brillouin zone was sampled using efficient grids generated by the *k*-point grid server[111] with a minimum distance of 18 Å between real-space lattice points; For Pt(111), a minimum distance of 40 Å was used. The shift vectors were automatically chosen to minimize the number of irreducible *k*-points. The convergence criteria for the self-consistent iteration and the ionic relaxation loop were set to 10^{-4} eV and 10^{-3} eV per cell, respectively.

The hydrogen adsorption free energy was calculated as $\Delta G_H = \Delta E_H + \Delta ZPE - T\Delta S$, where $\Delta E_H = E(slab + H^*) - E(slab) - \frac{1}{2}E(H_2(g))$ is the adsorption energy, ΔZPE and ΔS are

the differences in zero point energy and entropy between the adsorbed H* and the H_2 gas. All ZPEs of adsorbed H* were calculated using a second-order finite difference method (normal-mode analysis) with a step size of 0.015 Å. The $TS_{H_2(g)}$ of 0.41 eV in gas phase at 300 K was taken from the standard molecular tables.[275] The vibrational entropy in the adsorbed state was ignored as it is relatively small (0.01 eV at 300 K).[254, 268]

The climbing image nudged elastic band[190-191] (CI-NEB) approach was used to calculate activation barriers for the Volmer, Heyrovsky, and Tafel reactions, as well as surface diffusion. For the Volmer and Heyrovsky reactions, one layer of explicit H_2O/H_3O^+ water was used. Previous work have shown little difference in the interfacial field between systems with one, two, or three water layers.[268, 276] Molecular dynamics were run for 5 ps to obtain reasonable water structures on the phosphide surfaces. The atoms in the bottom two layers were fixed during relaxation, and the forces on the climbing images were converged to 0.10 eV/Å and subsequently converged to 10^{-3} eV using energy convergence. All other NEB calculations have a force convergence of 0.05 eV/Å. Dipole corrections were applied (Figure 29). The zero potential used in this work was referenced to the absolute potential of 4.4 V, which has been determined experimentally.[277-278]

To calculate the charge transfer coefficients and the Volmer and Heyrovsky barriers at constant potential, the supercell extrapolation[268, 276] and the charge extrapolation[279] schemes by Nørskov and co-workers were used. The charge extrapolation scheme is shown as follows:

$$E_2(\Phi_1) - E_1(\Phi_1) = E_2(\Phi_2) - E_1(\Phi_1) + \frac{(q_2 - q_1)(\Phi_2 - \Phi_1)}{2}, \qquad (49)$$

$$\Delta E(\Phi_{IS}) = E_{FS}(\Phi_{IS}) - E_{IS}(\Phi_{IS}) \\ = E_{FS}(\Phi_{FS}) - E_{IS}(\Phi_{IS}) + \frac{(q_{FS} - q_{IS})(\Phi_{FS} - \Phi_{IS})}{2}, \tag{50}$$

$$E_a(\Phi_{IS}) = E_{TS}(\Phi_{IS}) - E_{IS}(\Phi_{IS}) \\ = E_{TS}(\Phi_{TS}) - E_{IS}(\Phi_{IS}) + \frac{(q_{TS} - q_{IS})(\Phi_{TS} - \Phi_{IS})}{2}, \tag{51}$$

where Φ is the work function, q is the charge of the slab plus adsorbates, and $E_1(\Phi_1)$ and $E_2(\Phi_2)$ are energies from constant-charge calculations. Note that these are extrapolations to the potential of the initial state (IS). Alternatively, extrapolations to the end state (or transition state) can be done by interchanging index 1 and 2 in equation (49).

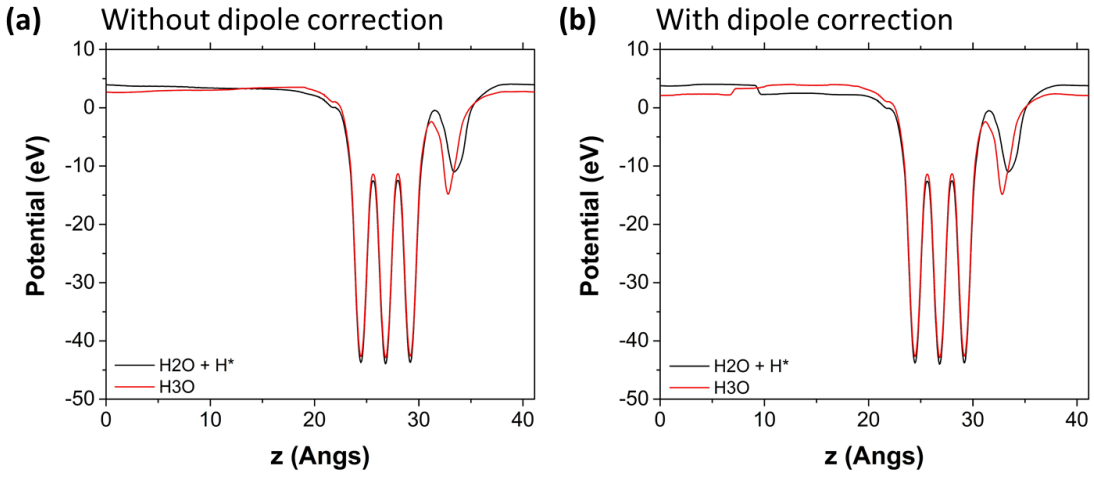

Figure 29. Local potential in *z* direction of Pt(111) slabs without and with dipole correction. Black curve represents a neutral water layer with an extra H on the surface. Red curve represents a water layer with an extra H in the water layer, i.e. forming $H_3O^{\delta+}$. Using dipole correction is necessary to determine the work function difference.

6.2.3 Monte Carlo simulations

Grand canonical Monte Carlo[92] simulations were performed to study the hydrogen adsorption structures and energetics as a function of temperature and applied potential. For each catalyst surface studied, simulated annealing was run from 1500 K and then decreased in steps by 50 K until 300 K. At each temperature, the number of Monte Carlo iterations was 2000 times the number of adsorption sites in the 12×12 supercell. (The number of adsorption sites per unit cell for Co_2P(101), CoP(101), Fe_2P(100), FeP(011), and Pt(111) are 4, 5, 3, 4, and 2, respectively.) After the annealing, the thermodynamically averaged current densities and hydrogen coverages were recorded during the Monte Carlo simulations at 300 K with the same iteration numbers mentioned above.

6.2.4 Hydrogen coverage and evolution rates

The rate of hydrogen evolution was calculated by:

$$k = \nu \exp(-E_a / k_B T), \tag{52}$$

where E_a is the activation energy for H_2 liberation and ν is a kinetic pre-factor. It was assumed that the prefactor is the same for all reactions in this work and all current density will be expressed relative to that of the Tafel reaction on Pt(111) at –0.12 V, which has the highest current density of any reaction considered here. The relatively small potential window here was chosen because active HER catalysts usually do not require significantly large overpotentials.

By using cluster expansions, it becomes straightforward to calculate adsorption energies (ΔE) for all possible hydrogen configurations. However, it would be expensive to calculate activation barriers (E_a) for all possible configurations. To estimate E_a for the Tafel and Heyrovsky steps, the Brønsted-Evans-Polanyi relationships[280-282] were constructed by fitting a set of representative DFT-calculated E_a values to calculated adsorption energies on Pt(111) and transition metal phosphides (Figure 30 and Figure 31). The charge transfer coefficients were calculated for representative sites for each element in a similar way using the supercell extrapolation scheme.[268, 276] The hydrogen desorption rate in equation (52) is converted to current density by:

$$j = keN / A, \tag{53}$$

where N / A is the number of adsorption sites per area. The average current was calculated by summing up the current j contributed from all possible adsorbed hydrogen atoms (or pairs) and then divided by the number of hydrogen adsorption sites. The turnover frequencies for individual sites were calculated in a similar way.

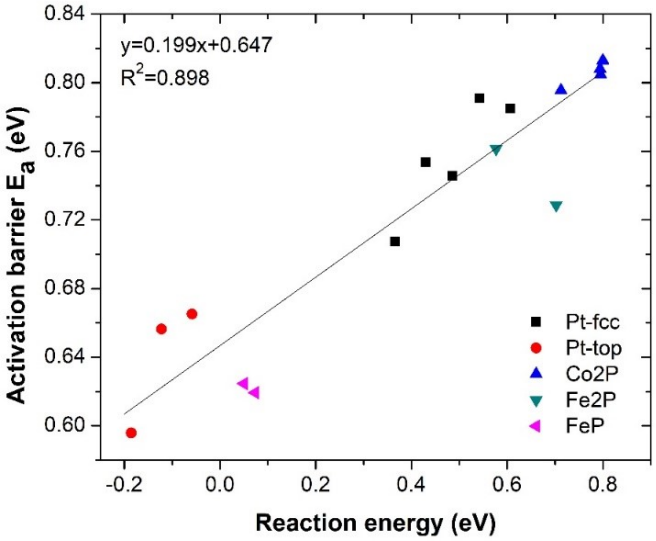

Figure 30. Brønsted-Evans-Polanyi (BEP) relationship of the Tafel reactions on Pt and transition metal phosphides. The different pairs of sites are: Pt(111) fcc + fcc, Pt(111) top + fcc, Co_2P Co bridge_*a* + bridge_*a*, Co_2P Co bridge_*a* + bridge_*b*, Co_2P bridge_*a* + P top, Fe_2P Fe bridge + bridge, Fe_2P Fe bridge + Fe-P bridge, FeP Fe bridge + bridge, and FeP Fe bridge + P top.

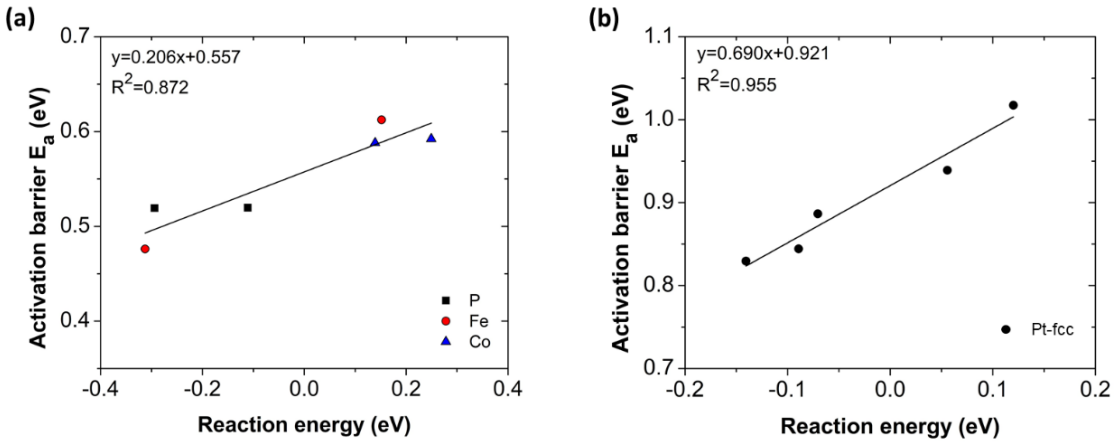

Figure 31. Brønsted-Evans-Polanyi (BEP) relationship of the Heyrovsky reactions at 0 V on (a) transition metal phosphides and (b) Pt(111) fcc sites with different H* coverages. The sites on transition metal phosphides are: P sites of CoP and FeP, Fe sites of FeP and Fe_2P, and Co bridge_*a* sites of Co_2P (one with dilute coverage and one with nearby Co bridge_*b* site occupied). All other sites on transition metal phosphides are with a dilute coverage.

Thermodynamically averaged currents, coverage, and arrangements of hydrogen atoms on different surfaces at different applied potentials were calculated using Metropolis Monte Carlo[92] simulations at 300 K. In these simulations, the applied potential was accounted for by using the computational hydrogen electrode (CHE)[138] model, in which the chemical potential of the proton-electron pair is equal to half that of H_2(g) at all temperature and pH values:

$$\mu(H^+ + e^-) = \frac{1}{2}\mu(H_2(g)) - eU, \tag{54}$$

where e is the elementary charge of an electron and U is the applied potential vs. the reversible hydrogen electrode (RHE). (In this work, all listed potential values are vs. the RHE.) According to Skúlason *et al.*,[268, 283] the activation barrier for the proton-electron transfer to the surface of Pt (the Volmer step) is much lower than that of H_2(g) desorption, i.e. H_2(g) desorption would be the rate-limiting step for the HER. It is shown that this is also true for transition metal phosphides[272] (Table 12). The chemical potential of adsorbed hydrogen can therefore be expected to be primarily determined by that of the proton-electron pair rather than by H_2(g). The reference chemical potential when calculating the potential-dependent hydrogen coverage in Monte Carlo simulations was chosen to be $\mu(H^+ + e^-)$. This will be revisited in the later section (see 6.3.5).

Table 12. Activation barriers for the Volmer step on transition metal phosphides and Pt(111) at 0 V. The extrapolation shows that hydrogen deposition on Pt-top is barrierless.

	Metal site (eV)	P site (eV)
FeP(011)	0.43	0.02
Co_2P(101)	0.31	0.36
Pt(111)	0	-

6.3 Results

6.3.1 Hydrogen adsorption and coverage

The surfaces considered in this work, including the four transition metal phosphide surfaces and a Pt(111) surface, are shown in Figure 32; the possible adsorption sites and their adsorption free energies are also shown in the same figure. The terminations of the transition metal phosphides are those that are believed to be the most probable surfaces from Kibsgaard *et al.*,[255] but it is worth noting that there might exist other low-energy terminations or surface reconstructions (which could be further searched using e.g. a genetic algorithm).

It is observed in Figure 32 that hydrogen adsorption is generally stronger on the metal-bridge sites of Fe_2P/Co_2P (blue colors) than FeP/CoP. In contrast, hydrogen adsorption on P sites of FeP/CoP is stronger than that on Fe_2P/Co_2P. The colors indicate the free energy of adsorption at a dilute coverage at 0 V. On Pt(111), hydrogen adsorption on the fcc site is 0.04 eV stronger than on the top site and all ΔG_H are slightly negative. Ideally, the hcp

site should also be considered, however, its adsorption energy is the weakest among all three adsorption sites (about 0.05 eV weaker than fcc) and Tan *et al.* found that the hcp coverage is less than 0.01 ML at negative potentials.[38] Thus, only the fcc and top sites are included in the current cluster expansion for Pt(111).

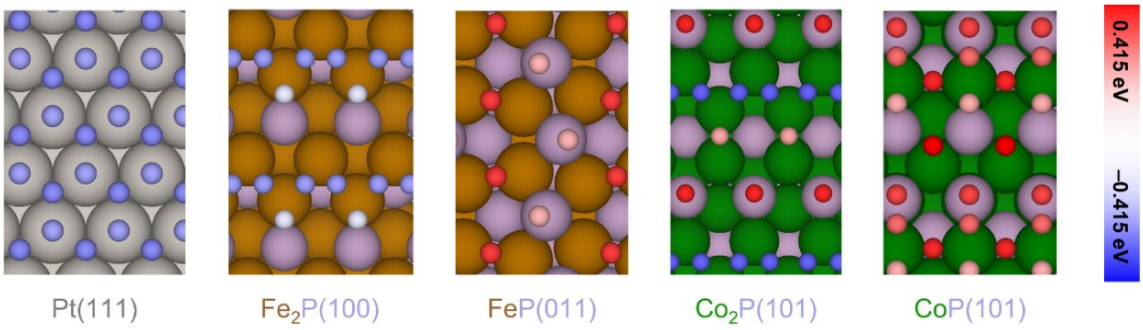

Figure 32. Surfaces with all possible hydrogen adsorption sites for Pt(111), $Fe_2P(100)$, FeP(011), $Co_2P(101)$, and CoP(101). Large grey spheres represent Pt, purple spheres represent P, gold spheres represent Fe, and green spheres represent Co. Small colored spheres represent H, and the colors indicate the free energy of adsorption ΔG_H for an isolated hydrogen atom at each site at a potential of 0 V. Atomic-scale structural images were generated using VESTA.[129]

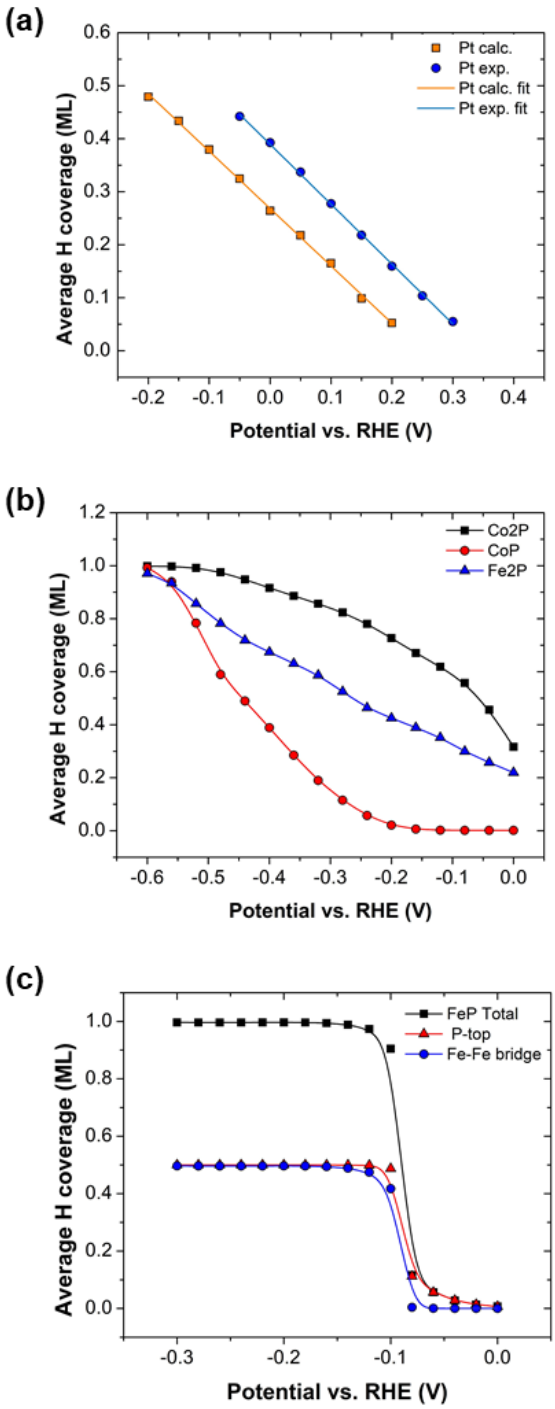

Figure 33. Average hydrogen coverage as a function of applied potential on (a) Pt(111), (b) the model surfaces for Co_2P(101), CoP(101), and Fe_2P(100). (c) Average hydrogen coverage and breakdown of the site contributions on FeP(011). The experimental data for Pt(111) are taken from Marković *et al.*[284]

The thermodynamically averaged surface hydrogen coverages at 300 K as a function of the applied potential are shown in Figure 33. The potential dependence of hydrogen coverage can be fit to a Frumkin isotherm:[284-285]

$$\frac{\theta}{1-\theta}\exp\left(\frac{r\theta}{RT}\right)=\exp\left(-\frac{U_{RHE}F}{RT}\right)\exp\left(-\frac{\Delta G_H^{\theta=0}}{RT}\right) \tag{55}$$

where U_{RHE} is the applied potential, F is the Faraday constant, and ΔG_H is the free energy of adsorption, and r is the interaction parameter that characterizes the lateral interactions among adsorbed hydrogen atoms. The interaction parameter, which is related to the slope of the coverage with respect to applied potential, is repulsive for $r>0$ and attractive for $r<0$. On Pt(111), the value of the interaction parameter that fits best to the Monte Carlo simulations at intermediate coverages is 32 kJ/mol, which is in excellent agreement with experimentally measured value of 30 kJ/mol (Figure 33a).[284] At these coverages the curve is nearly linear due to the non-exponential term of $\theta/(1-\theta)$, which then can be treated effectively as a nearly constant term compared to other exponentially varying terms. The hydrogen coverage reaches 0.5 ML, corresponding to all fcc sites being filled, at about –0.16 V, which is shifted by about 0.1 V from experimental findings.[253, 284] The relative position of the curve (in the horizontal axis) is determined by the free energy of adsorption, where the small deviation is due to the difference between DFT-calculated and experimentally measured adsorption free energy (ΔG_{DFT} = –21 kJ/mol and ΔG_{Exp} = –27 kJ/mol).[284]

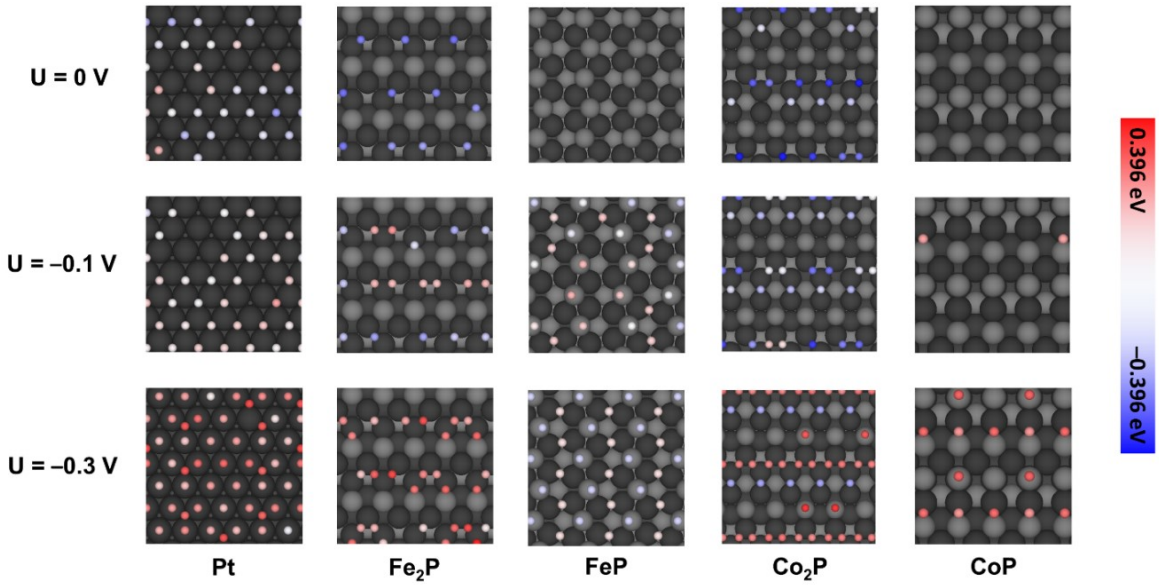

Figure 34. Snapshots of Monte Carlo simulations of adsorbed hydrogen on the surfaces of Pt(111) and phosphide surfaces. The simulations were run at 300 K with applied potentials of 0, –0.1, and –0.3 V. The grey and black spheres are the P and metal atom (Co or Fe) of the underlying material, and the colored circles represent adsorbed hydrogen atoms. The colors indicate the free energies of adsorption at each site relative to H_2(g). Atomic-scale structural images were generated using VESTA.[129]

At 0 V, the coverage of hydrogen on CoP and FeP is significantly below that of Pt(111). The hydrogen coverage on Co_2P/Fe_2P increases more quickly than it does on CoP as the potential drops more negatively (Figure 33b). An inspection of snapshots of the Monte Carlo simulations (Figure 34) reveals that the metal-metal bridge sites on Co_2P and Fe_2P, which do not exist on CoP and FeP, are populated first, due to stronger adsorption energies on these sites (see Figure 32). On FeP(011) the hydrogen coverage of both P sites and Fe-Fe sites quickly shift from 0 to 1 ML at around –0.1 V (Figure 33c and Figure 34), suggesting a phase transformation with either an empty surface or one fully occupied by hydrogen being energetically favorable. This is verified by inspecting DFT calculations of

the training data, where the formation energies (relative to an empty surface and a fully occupied surface) are positive for all coverages (Figure 35).

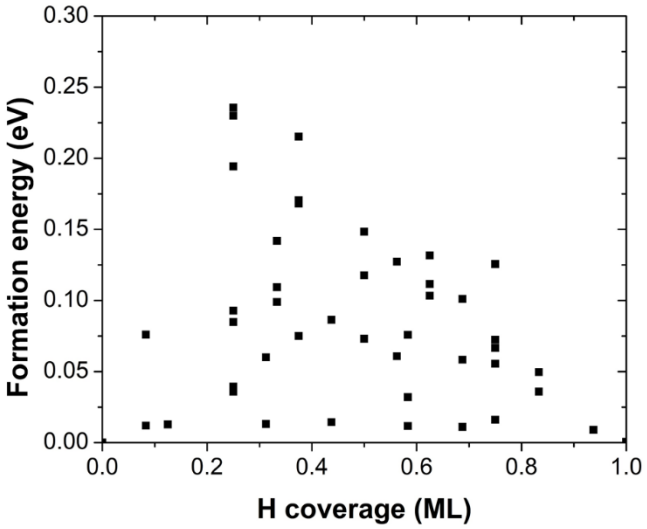

Figure 35. Training data for FeP(011). Formation energy with respect to an empty surface and a fully occupied surface.

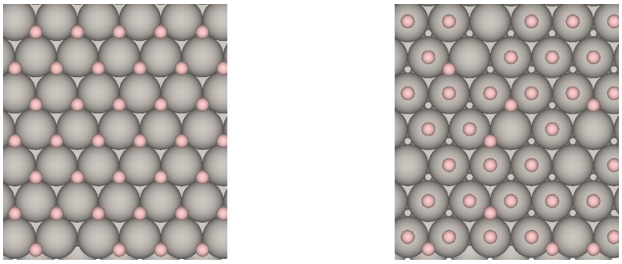

Figure 36. Monte Carlo snapshots of hydrogen adsorption at 300 K on Pt(111) at –0.16 V and –0.18 V. Large grey spheres and small pink spheres represent Pt and H, respectively. A phase transition from fcc-adsorption to top-adsorption was observed when decreasing the potential. Atomic-scale structural images were generated using VESTA.[129]

For Pt(111), it is observed that there is relatively little interaction between the adsorbed hydrogen atoms at small overpotentials (Figure 34), resulting in nearly uniform free energies of adsorption for all hydrogen atoms until the potential reaches –0.18 V, where a phase transformation takes place: the hydrogen adsorption structure of predominantly fcc-adsorption becomes energetically unfavorable and top-adsorption becomes more favorable at these potentials (Figure 36). This phase transformation was also observed from the cluster expansion simulations by Tan *et al.* at a potential of about –0.4 V.[38] The shift is possibly because of the differences in the DFT-calculated training set (e.g. slab thicknesses) and the way the cluster expansion is constructed and fitted. Experiments suggested that top H* appears at negative potentials after a monolayer of fcc sites are filled.[253, 286-287]

In general, as hydrogen coverage increases, the hydrogen-hydrogen lateral interactions would weaken the adsorption energies of hydrogen atoms on the different surfaces, thus facilitating H_2 liberation. This is particularly obvious on the metal-metal bridge sites on Fe_2P and Co_2P (Figure 34), where hydrogen binding to the surface becomes significantly weaker (shift from blue to red colors) as the potential becomes more negative and coverage increases. These lateral interactions serve to reduce the activation barriers for the HER and enhance the activities of these sites at negative potentials relative to what would be expected based on the single DFT calculation of the ΔG_H for an isolated H*. Similarly, the higher-energy sites that are not heavily occupied at 0 V become the most active ones at more negative potentials due to lateral interaction and/or phase transition.

6.3.2 HER mechanisms

There are two mechanisms for H_2 evolution. The first is the Volmer-Tafel mechanism, in which two adsorbed H* (come from the Volmer reaction) form a H_2(g) molecule via chemical desorption:

$$2(H^+ + e^-) \longleftrightarrow 2H^* \longleftrightarrow H_2(g), \tag{56}$$

where 2H* denotes two adsorbed nearby hydrogen atoms on the catalyst surface.

The Volmer-Heyrovsky mechanism consists of a coupled proton-electron transfer (the Volmer reaction) and an electrochemical desorption step, which involves a proton and an adsorbed H*:

$$H^+ + e^- \longleftrightarrow H^*, \;\; H^+ + e^- + H^* \longleftrightarrow H_2(g). \tag{57}$$

An illustration of the above elementary reaction steps for Pt(111) and FeP(011) is shown in Figure 37. The calculated free energies of adsorption on different sites and an inspection of Monte Carlo snapshots (Figure 34) on different surfaces may suggest that the Volmer-Heyrovsky mechanism (or a mixed mechanism) is more likely to be dominant on transition metal phosphides than on Pt(111), due to i) greater differences in adsorption free energies at neighboring sites so that Tafel reactions may be less likely to occur and ii) the increased probability of finding isolated hydrogen atoms with near-optimal hydrogen adsorption free energies compared to Pt(111), where all adsorbed H* have nearly the same ΔG_H at small overpotentials. This is consistent with observation of differing Tafel slopes, an indicator of reaction mechanism, on platinum and transition metal phosphides.[253, 256-257] Under the

assumption that catalytic activity is maximized when $\Delta G_H = 0$, the snapshots in Figure 34 indicate that the most active sites on transition metal phosphide surfaces may be driven by local atomic disorder.

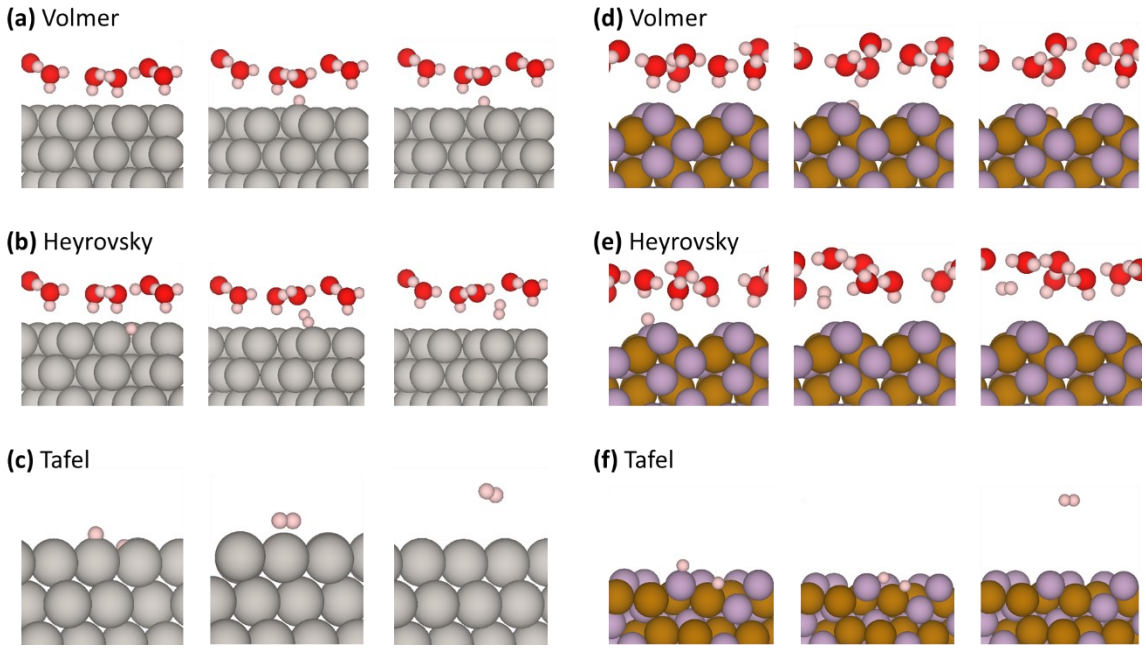

Figure 37. Elementary steps of Volmer, Heyrovsky, and Tafel reactions on Pt(111) and FeP(011). The columns within each panel correspond the initial state, transition state, and final state. Grey spheres represent Pt, gold spheres represent Fe, purple spheres represent P, red spheres represent O, and pink spheres represent H. Atomic-scale structural images were generated using VESTA.[129]

The pairs of neighboring hydrogen atoms that could form H_2(g) via the Volmer-Tafel mechanism were obtained by the construction of a two-dimensional Voronoi diagram (Figure 38).[288] Considering the possibility that the surface diffusion of H* could be rate-limiting, the activation barriers for diffusion between neighboring adsorption sites were also calculated and shown in the same figure (Figure 38). These barriers for diffusion are

below the Tafel barriers, and thus it is unlikely that the surface diffusion is the rate-limiting step on these surfaces.

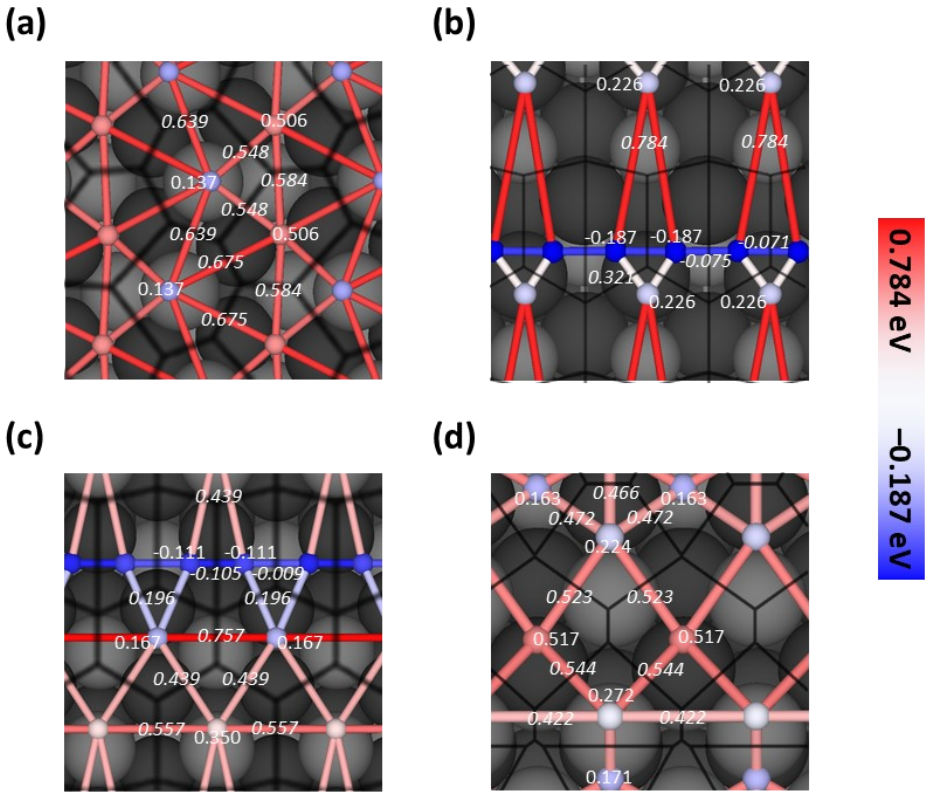

Figure 38. DFT-calculated hydrogen diffusion paths and barriers on (a) FeP, (b) Fe_2P, (c) Co_2P, and (d) CoP. Large grey and black spheres are the P and metal atom of the underlying material. Small spheres are H atoms. The color of the small hydrogen atom (and number) indicates the adsorption energy in eV at the specific site, and the color of the bond between two hydrogen atoms indicates the transition state energy along this path (given by numbers in italics). The black lines indicate the edges on the Voronoi diagrams that define neighboring atoms.

6.3.3 HER on Pt(111): weakly adsorbed species

For Pt(111), the HER prefers the Volmer-Tafel mechanism by more than three orders of magnitude compared to the Volmer-Heyrovsky mechanism (Figure 39a). The mechanism

has also been suggested by experiments.[253, 289] It is a result of the Tafel reaction barriers being lower than the Heyrovsky barriers; such trend is the opposite of what is observed on the transition metal phosphide catalysts.

The most active sites are the Pt top sites, for which there are two possible routes (top + top or top + fcc) for the HER. In this work it is found that the top + fcc route is more favorable because of the balance of hydrogen coverage and activation barrier.[272] The top + top Tafel route produces a ~30 mV/dec Tafel slope, as the coverage of both of the weakly adsorbed top H* can change exponentially with applied potential. The top + fcc route has a higher Tafel slope (38 mV/dec) due to nearly saturated fcc sites, which are consistent with Lindgren *et al*.[290] Although different pairs of active sites are claimed, both Lindgren *et al.* and this work suggest that the weakly bound Pt-top H* is kinetically active for the HER. The role of kinetically active Pt-top species is consistent with both experiments[253, 287] and simulations.[38, 170]

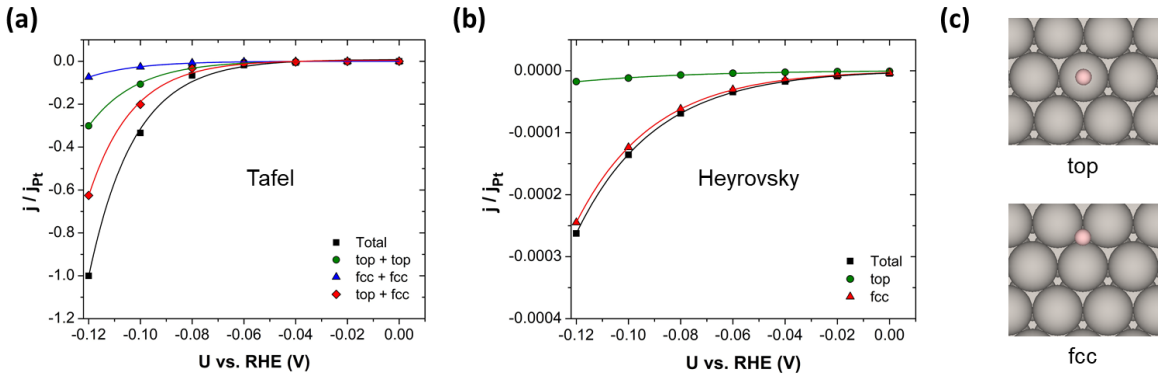

Figure 39. HER current density of Pt(111) as a function of applied potential assuming the rate-limiting step is either a Tafel reaction (a), or a Heyrovsky reaction (b). The current density is expressed as relative current to the Tafel current of Pt(111) at –0.12 V, which is denoted as j_{Pt}. (c) The top site and fcc site. Atomic-scale structural images were generated using VESTA.[129]

6.3.4 HER on metal phosphides: mixed mechanism

The predicted Tafel slopes for CoP and FeP are within the range of experimentally-determined values (Table 13) assuming the Volmer-Heyrovsky mechanism (FeP may have a mixed mechanism). These slopes could be rationalized by the dilute surface H* coverage at equilibrium potential so that the coverage could change exponentially with applied potential. For Co_2P, the Tafel slope assuming the Volmer-Tafel mechanism is predicted to be 46 mV/dec at small overpotentials, and it transitions to infinity at large overpotentials as the surface H* is saturated (Figure 41a), which is consistent with both experiment[289] and simulation.[291] For the Volmer-Heyrovsky mechanism, the slope is predicted to be 85 mV/dec at small overpotentials (Figure 41b) due to the relatively high surface hydrogen coverage at 0 V and it increases to 165 mV/dec at large overpotentials ($U < -0.5$ V). The Tafel slope is indeed coverage-dependent, which can be seen from this work[272] (generally larger Tafel slopes) and recent studies using micro-kinetic models.[291-293] The significant increase of Tafel slope at large overpotentials can be understood by the loss of potential dependence of the Volmer step when all surface sites saturate.[291-292] A theoretical value of about 120 mV/dec is obtained assuming that the charge transfer coefficient is 0.5; the Tafel slope according to Monte Carlo simulation in this work corresponds to a charge transfer coefficient of 0.36, which is consistent with the DFT-calculated value of 0.34 (Figure 40). Similar conclusions regarding the coverage are seen for the $Fe_2P(100)$ surface.[272]

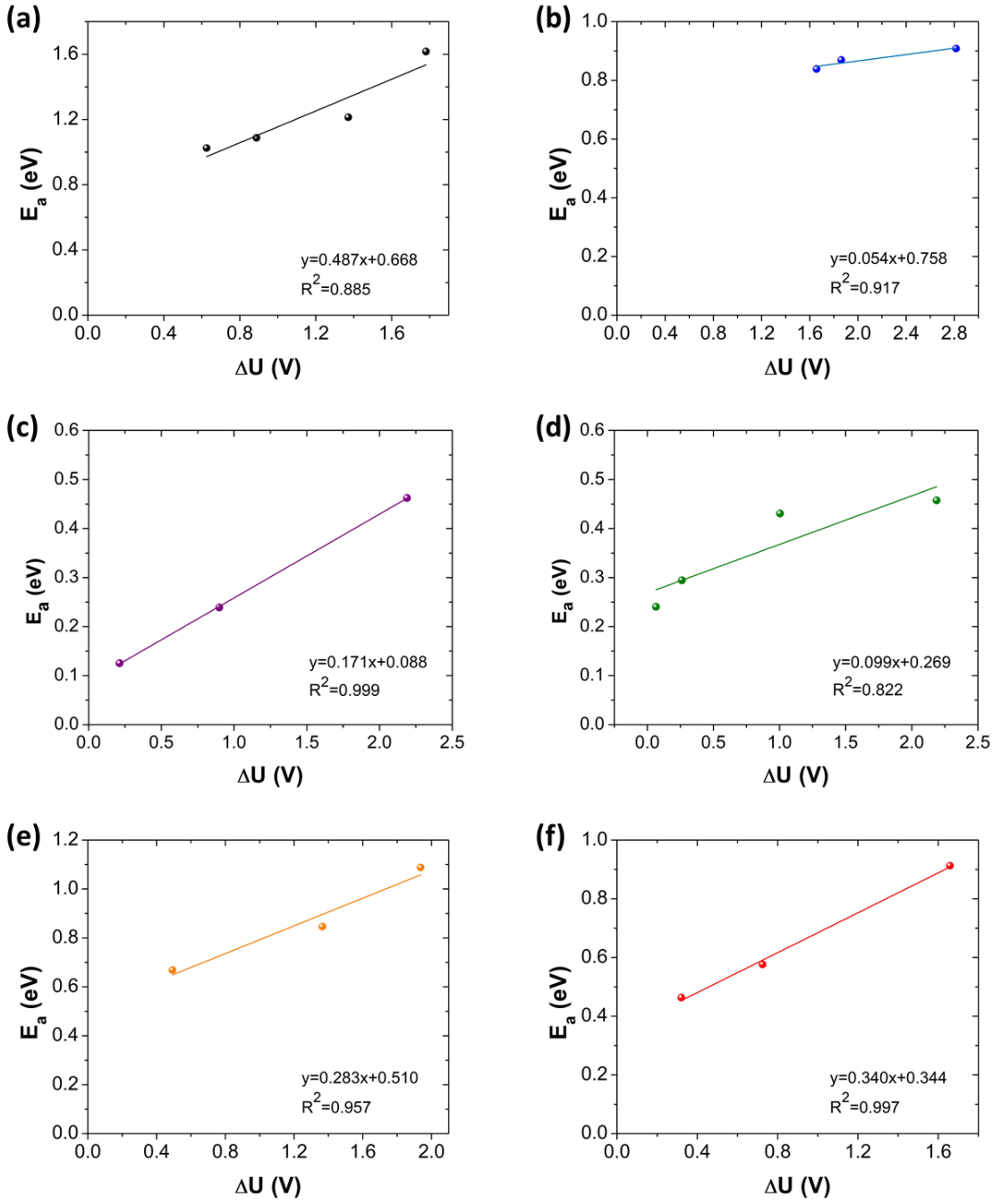

Figure 40. DFT-calculated Heyrovsky activation barriers E_a on (a) fcc site of Pt, (b) P site of FeP, (c) Fe site of Fe_2P, (d) P site of CoP, (e) Fe site of FeP, and (f) Co bridge_*a* site of Co_2P by using the supercell extrapolation scheme.[268, 276] ΔU is the change in potential between the initial state (with H*) and final state (with H_2(g)). Charge transfer coefficients are obtained as the slopes of the linear fits.

The predicted HER current densities and active sites for $Co_2P(101)$ assuming the rate-limiting step is either a Tafel or a Heyrovsky reaction are shown in Figure 41c and Figure 41d. The Co bridge sites are predicted to be the most active sites via the Heyrovsky mechanism, which is favored over the Tafel mechanism by more than 2 orders of magnitude. This is largely due to the smaller activation barriers for Heyrovsky reactions than Tafel reactions (by ~0.3 eV). There are strong lateral interactions between the hydrogen atoms adsorbed on Co bridge_*a* sites (Figure 41e) as discussed above that weaken the hydrogen adsorption energies (in the same direction as reducing the activation barriers) and thus facilitate H_2 liberation. Therefore, the Tafel slope for the Co bridge_*a* site (83 mV/dec) is lower than that of the Co bridge_*b* site (185 mV/dec) at small overpotentials, and a change in active sites from the Co bridge_*b* to Co bridge_*a* site at about –0.06 V is observed, even though the ΔG_H for an isolated H* is closer to 0 eV on the bridge_*b* site, which highlights one of the challenges of using the ΔG_H as the descriptor for HER activity.

Across the five catalyst surfaces studied in this work, Tafel slopes of 32~46 mV/dec (assuming a Tafel reaction is rate-limiting) and 44~123 mV/dec (assuming a Heyrovsky reaction is rate-limiting) are predicted from the cluster expansions, which are consistent with the range of reported values (see Table 13).[260-262, 271, 291, 294]

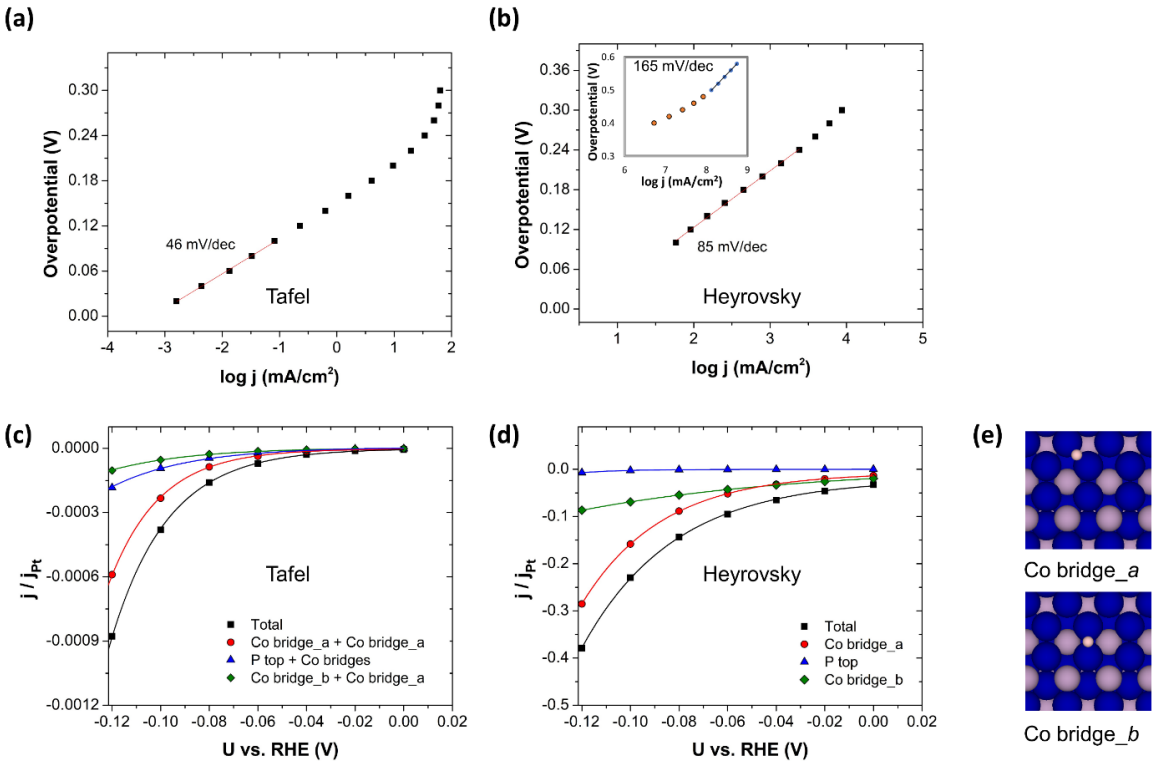

Figure 41. Tafel plots of HER on $Co_2P(101)$ assuming the rate-limiting step is either a Tafel reaction (a), or a Heyrovsky reaction (b). The inset in (b) shows the Tafel slope at higher overpotentials. Current density of $Co_2P(101)$ as a function of applied potential assuming the rate-limiting step is either a Tafel reaction (c), or a Heyrovsky reaction (d). The current density is expressed as relative current to the Tafel current of Pt(111), which is denoted as j_{Pt}. (e) Two types of Co bridge sites: "bridge_*a*" represents bridge site along *a*-axis and "bridge_*b*" represents bridge site along *b*-axis. Atomic-scale structural images were generated using VESTA.[129]

On FeP(011), several interesting features are worth discussing. The partial current density involving hydrogen bound on P-top sites remains relatively small as the potential is decreased (Figure 42a and Figure 42b) for two reasons. The first is due to the anomalously low charge transfer coefficient on the P site (0.05) compared to Fe site (Figure 40), which effectively make the decrease in E_a with respect to potential on the P sites less sensitive. The second is that the hydrogen adsorbed on these sites becomes more strongly bound at

more negative potentials. This unusual decrease of ΔG_H at higher coverages on the P-top site was also observed by Kibsgaard *et al*. in their origin paper (DFT calculations; although different exchange correlation functionals were used).[255] The decrease in ΔG_H with respect to coverage manifests itself in a way to abruptly enhance the catalytic activity at –0.1 V, in line with the aforementioned phase transition. The H* coverage jumps from nearly 0 to almost 1 ML (Figure 33). At this point the Tafel current almost immediately saturates, and the Heyrovsky current also has an abrupt jump (Figure 42). The sites involving Fe-bridge are identified to be the most active sites for the HER (Figure 42b).

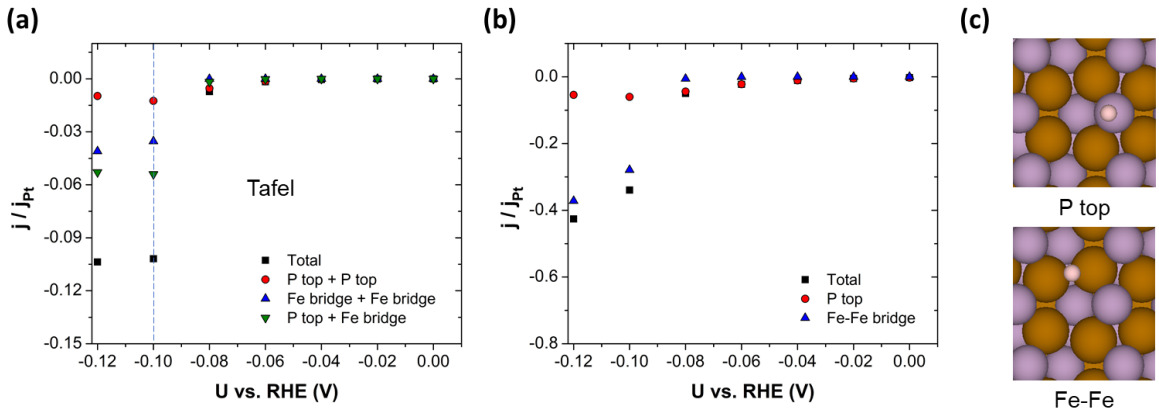

Figure 42. HER current density of FeP(011) as a function of applied potential assuming the rate-limiting step is either a Tafel reaction (a), or a Heyrovsky reaction (b). The current density is expressed as relative current to the Tafel current of Pt(111), which is denoted as j_{Pt}. The dashed line marks the phase transformation from an empty surface to a fully occupied surface. (c) The P top site and Fe-Fe bridge site. Atomic-scale structural images were generated using VESTA.[129]

Table 13. Predicted Tafel slopes (in mV/dec) at low overpotentials (U > –0.2 V) for the Volmer-Tafel mechanism and the Volmer-Heyrovsky mechanism on transition metal phosphides and Pt(111). The number in bold indicates a likely mechanism.

	Tafel	Heyrovsky	Experiments	Ref.
Fe_2P(100)	37	123	52~80	295-297
FeP(011)	**32**	**60**	29~76	261, 295, 298
Co_2P(101)	**46**	**85**	45~101	299-301
CoP(101)	38	**55**	50~70	294, 300, 302
Pt(111)	**34**	44	26~37	267, 295, 303
Ni_xP_y	-	-	27~51	260, 304-305

6.3.5 The chemical potential

Finally, it is worth revisiting the statement made previously, that the chemical potential of the adsorbed hydrogen is equilibrated with that of the proton-electron pair if the Volmer step is not rate-limiting. Consider the Volmer-Heyrovsky mechanism here (the Volmer-Tafel mechanism can be shown in a similar way), the forward and reverse reactions are:

$$H^+ + e^- \underset{k_{-1}}{\overset{k_1}{\rightleftarrows}} H* \underset{k_{-2}}{\overset{k_2}{\rightleftarrows}} \frac{1}{2} H_2(g). \tag{58}$$

The steady-state H* coverage θ can be determined by solving equation below,

$$\frac{\partial \theta}{\partial t} = k_1 c_{H^+}(1-\theta) - k_{-1}\theta - k_2\theta + k_{-2} p_{H_2}(1-\theta) = 0, \tag{59}$$

with the rate constants being:

$$k_1 = \nu \exp\left(-\frac{E_{TS1} - \mu(H^+ + e^-)}{kT}\right), \tag{60}$$

$$k_{-1} = \nu \exp\left(-\frac{E_{TS1} - \mu(H^*)}{kT} \right), \tag{61}$$

$$k_2 = \nu \exp\left(-\frac{E_{TS2} - \mu(H^*)}{kT} \right), \tag{62}$$

$$k_{-2} = \nu \exp\left(-\frac{E_{TS2} - \frac{1}{2}\mu(H_2)}{kT} \right), \tag{63}$$

where E_{TS1} and E_{TS2} are the transition-state energies for the Volmer and Heyrovsky steps and the "-" sign in the subscripts indicate the reverse reactions. For simplicity, here, the assumptions of $c_{H^+} = 1$ and $p_{H_2} = 1$ are made. The steady-state H* coverage is obtained to be:

$$\begin{aligned}
\theta &= \frac{k_1 c_{H^+} + k_{-2} p_{H_2}}{k_1 c_{H^+} + k_{-1} + k_2 + k_{-2} p_{H_2}} \\
&= \frac{\exp\left(\frac{\mu(H^+ + e^-) - E_{TS1}}{kT} \right) + \exp\left(\frac{\frac{1}{2}\mu(H_2) - E_{TS2}}{kT} \right)}{\exp\left(\frac{\mu(H^+ + e^-) - E_{TS1}}{kT} \right) + \exp\left(\frac{\mu(H^*) - E_{TS1}}{kT} \right) + \exp\left(\frac{\mu(H^*) - E_{TS2}}{kT} \right) + \exp\left(\frac{\frac{1}{2}\mu(H_2) - E_{TS2}}{kT} \right)} \\
&= \frac{1 + \exp\left(\frac{E_{TS1} - E_{TS2} + eU}{kT} \right)}{1 + \exp\left(\frac{\mu(H^*) - \mu(H^+ + e^-)}{kT} \right) + \exp\left(\frac{\mu(H^*) - \mu(H^+ + e^-) + E_{TS1} - E_{TS2}}{kT} \right) + \exp\left(\frac{E_{TS1} - E_{TS2} + eU}{kT} \right)} \\
&= \frac{1 + \exp\left(\frac{\Delta E^* + eU}{kT} \right)}{1 + \exp\left(\frac{\mu(H^*) - \mu(H^+ + e^-)}{kT} \right)\left[1 + \exp\left(\frac{\Delta E^*}{kT} \right) \right] + \exp\left(\frac{\Delta E^* + eU}{kT} \right)},
\end{aligned} \tag{64}$$

where $\Delta E^* \equiv E_{TS1} - E_{TS2}$. Rearranging equation (64), the effective chemical potential of H* can be expressed as:

$$\mu(H^*) = \mu(H^+ + e^-) + kT \ln\left(\frac{(1-\theta)\left[1+\exp\left(\frac{\Delta E^* + eU}{kT}\right)\right]}{\theta\left[1+\exp\left(\frac{\Delta E^*}{kT}\right)\right]}\right) \tag{65}$$

Now consider the following two cases:

Case I, $E_{TS1} << E_{TS2}$, $\Delta E^* << 0$, and $\Delta E^* << -eU$ (typically $U < 0$ so this is valid). The above equations are reduced to:

$$\theta = \frac{1}{1+\exp\left(\frac{\mu(H^*) - \mu(H^+ + e^-)}{kT}\right)}, \tag{66}$$

and

$$\mu(H^*) = \mu(H^+ + e^-) + kT \ln\left(\frac{1-\theta}{\theta}\right). \tag{67}$$

At intermediate coverages (e.g. less than a full monolayer of fcc site) the chemical potential of surface adsorbed H* will equilibrate with the chemical potential of proton-electron pair regardless of the applied potential and will have a nearly linear dependence of the coverage. If $\mu(H^*) < \mu(H^+ + e^-)$, then the hydrogen coverage will increase. A special case for U = 0 V is shown in Figure 43a, where ΔE^* does not have an effect on the chemical potential of H*.

Case II, $E_{TS1} >> E_{TS2}$, $\Delta E^* >> 0$. The above equations are reduced to:

$$\theta = \frac{1}{1+\exp\left(\frac{\mu(H^*)-\mu(H^+ + e^-)}{kT}\right)\exp\left(-\frac{eU}{kT}\right)}, \tag{68}$$

and

$$\begin{aligned}\mu(H^*) &= \mu(H^+ + e^-) + eU + kT\ln\left(\frac{1-\theta}{\theta}\right) \\ &= \tfrac{1}{2}\mu(H_2) + kT\ln\left(\frac{1-\theta}{\theta}\right).\end{aligned} \tag{69}$$

The chemical potential of H* in this case will equilibrate with the chemical potential of H_2(g) regardless of the applied potential when Volmer reaction is the rate-limiting step (a special case for $\Delta E^* = 0$ eV is shown in Figure 43b).

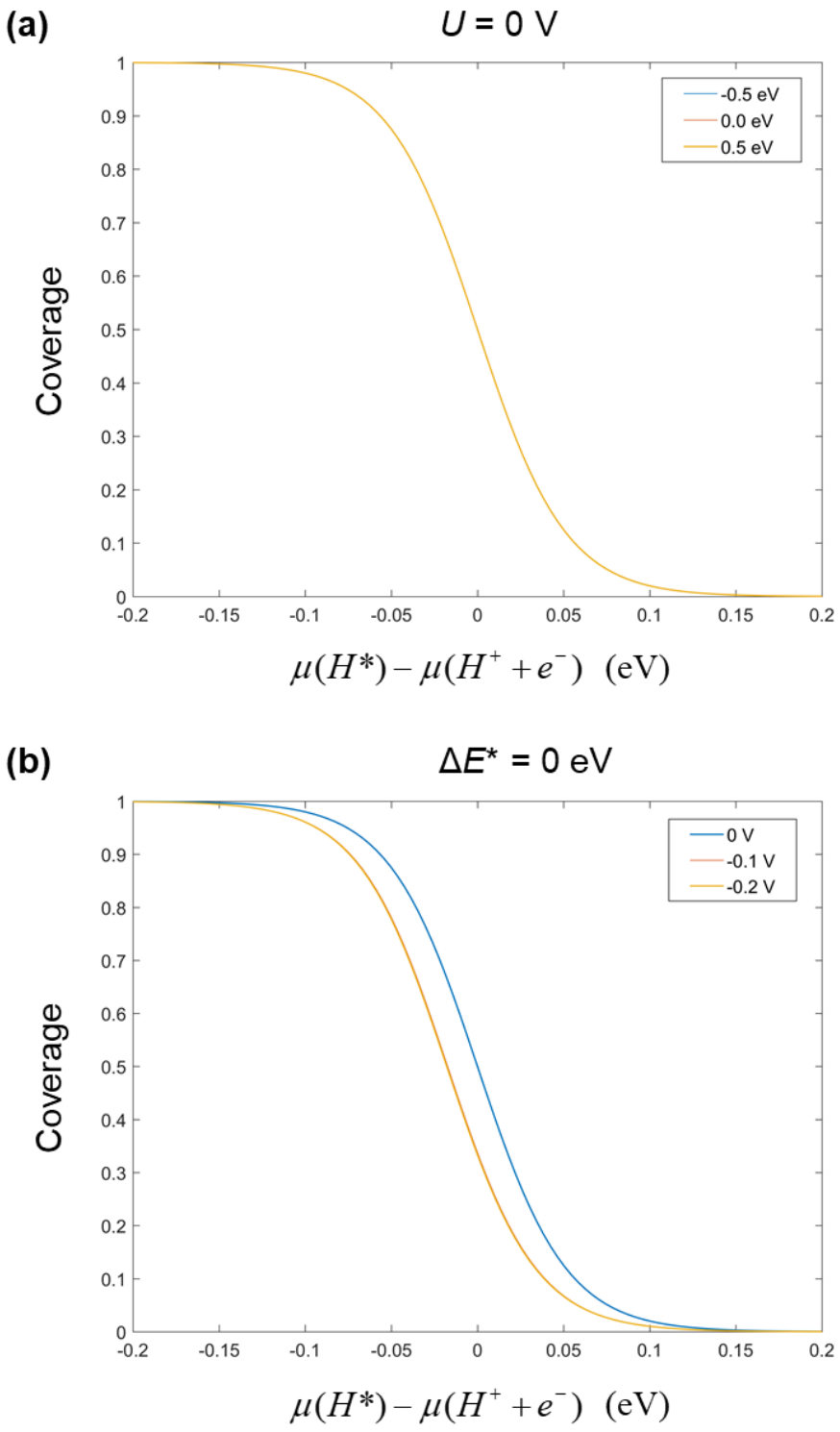

Figure 43. Coverage of hydrogen as a function of the chemical potential difference of $\mu(H^*)-\mu(H^+ + e^-)$ at (a) $U = 0$ V with varying activation energy difference ΔE^*, and (b) at $\Delta E^* = 0$ eV with varying applied potential.

6.4 Discussion

6.4.1 The challenge of using ΔG_H

Through the years researchers are using DFT-calculated ΔG_H as a descriptor for the HER activity. However, it could be challenging to obtain valuable insights for surfaces where ΔG_H is highly coverage-dependent. To illustrate this, the trends of HER current density of the Volmer-Heyrovsky mechanism are shown at 0, –0.1 and –0.3 V as a function of ΔG_H at both dilute coverage and full coverage (Figure 44a-d) for various surface sites on the transition metal phosphides and Pt(111). Further discussion of how the volcano shape is affected by coverage will be made. This discussion is limited to the Heyrovsky reaction for two reasons: i) the Heyrovsky mechanism is more likely on the transition metal phosphide surfaces and ii) the turnover frequency of each individual site can be examined more readily. (Alternatively, for Tafel mechanism, ΔG_{2H^*} can be examined.[306])

When plotting the log of the turnover frequency at 0 V against the free energy of adsorption in the dilute limit (Figure 44a), the right side of the volcano follows a nearly linear trend, because of their relatively low coverages at equilibrium potential and thus do not exhibit significant amount of lateral interactions with other highly occupied site, if there is any. This is particularly obvious for CoP (in down triangles), for which the coverages of all surface sites are predicted to be very low (Figure 34). Other sites shown in Figure 44a are P site on Co_2P and both sites on FeP.

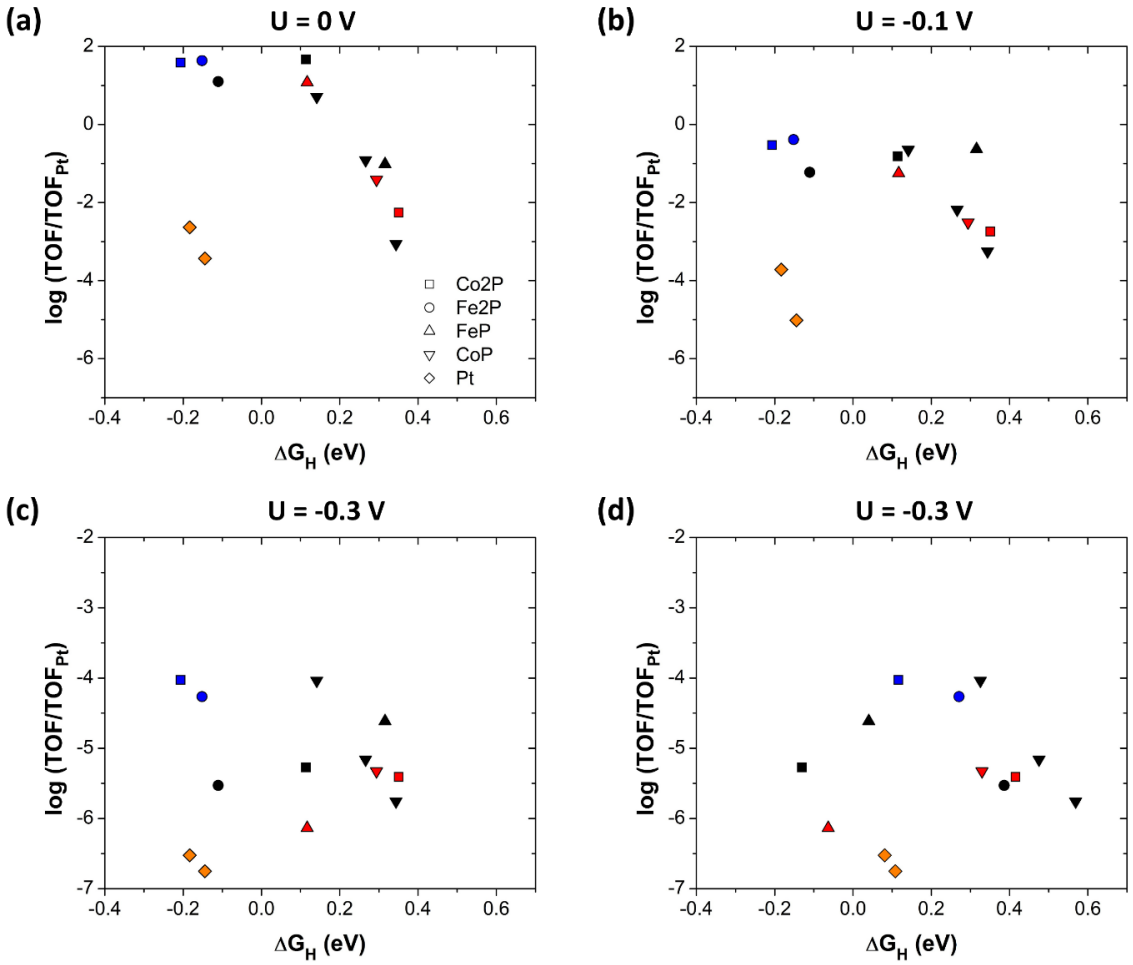

Figure 44. (a-c) Average turnover frequency (TOF) of various surface sites for which the turnover frequency is non-negligible at 0, –0.1, and –0.3 V, as a function of ΔG_H at dilute coverage. (d) Average HER (Volmer-Heyrovsky) turnover frequency of various surface sites at –0.3 V as a function of ΔG_H at a full monolayer. The TOF are expressed relative to that of Tafel reaction of Pt at a given potential. Color scheme: orange – Pt sites, red – P sites, blue – metal bridge sites with strong lateral interactions, black – other metal and metal-P sites.

For the left side of the volcano, the linear trend is almost lost, as ΔG_H in the dilute limit is a less accurate descriptor of the actual free energy of adsorption for these sites due to lateral interactions that would weaken the bond.[272] No obvious trends can be observed in Figure 44b and c either. Particularly, the metal-metal bridge sites of Co_2P and Fe_2P mentioned

previously, are on the left side. Pt(111) here does not follow the same trend as the transition metal phosphides (nor reside near the top of the volcano) because of the significantly different BEP relations. The volcano shape is restored at –0.3 V to some extent if the turnover frequencies are plotted against ΔG_H at a full monolayer coverage (Figure 44d), as this state more closely resembles the actual surface coverage at this potential (Figure 34).

6.4.2 Coverage effect

The fcc sites on Pt(111) have a ΔG_H around –0.18 eV at dilute coverage, and the P-top sites on FeP(011) have a ΔG_H around 0.11 eV at dilute coverage, which is expected to be more active for HER since it is closer to the top of the volcano. However, it has been observed that P-top sites on FeP become the least active sites at more negative potentials ($U < –0.1$ V). This could be due to the extremely low charge transfer coefficient, but even if the same charge transfer coefficient is assigned to the P-top sites as for Pt, the Pt sites are still more active as the potential is decreased (about 10 times at –0.3 V), which proves the poor activity of the P-top sites on FeP is largely due to coverage effect discussed earlier (unusual stabilization of H* as coverage increases). Also, on FeP, it is not clear whether the aforementioned phase transformation would happen in real-life catalysts. However, the potential for such a transformation to occur is important to keep in mind for surfaces on which catalytic activity appears to be suppressed because adsorbate binding becomes stronger as coverage increases. Once the phase transformation occurs, such surfaces may become highly active.[272]

6.4.3 Rational design of catalyst

The findings in this work can provide some insights into designing of HER catalysts not only valid for transition metal phosphides but may also work for other types of materials. The HER mechanism for Pt(111) is more likely to be the Volmer-Tafel mechanism, whereas for the transition metal phosphides, the Volmer-Heyrovsky (or mixed) mechanism is more likely, which is in good agreement with experiments.

An extremely low charge transfer coefficient on phosphorous was observed, and the Heyrovsky mechanism (the preferred mechanism for transition metal phosphides) is likely to prefer metal sites due to the reduced activation barriers on these sites at more negative potentials. This is consistent with a recent experimental and computational study showing that the Fe-rich phosphide Fe_3P has a smaller Tafel slope and higher activity compared to Fe_2P and FeP, where the metal sites were also found likely to be the most active sites.[295] In this work it is predicted that Fe_2P has a higher Tafel slope than FeP, opposite to experiment, which may suggest there are other possible hydrogen adsorption sites that can strongly interact with the neighboring hydrogen atoms (thus lowering the Tafel slope) on Fe_2P.

The hydrogen adsorption is most stable at bridge (bridge) sites, and the enhanced HER activity on these sites due to the favorable repulsive interactions have been observed on Co_2P,[272] for which the bridge sites are about 2.4 Å apart. Taking account of the particularly low surface diffusion barriers and similar adsorption energies between these active bridge sites, it might be possible to use such criteria to search for other possible catalyst surfaces that are promising for the HER as Pt.

6.5 Further considerations

6.5.1 KMC simulation

The HER activity has been predicted using Metropolis Monte Carlo simulations, which is a measure of the thermodynamically averaged activity for all the surface sites. A more accurate description of the HER activity can be modeled by running kinetic Monte Carlo (KMC)[157-158] simulations, from which the preferred reaction mechanism can be directly seen rather than assuming one, as has been the case for Metropolis Monte Carlo. For this purpose, a KMC simulation on Pt(111) is carried out using the same cluster expansion built for this work but using more accurate activation barriers from the work by Lindgren *et al.*,[290] which do not require expensive extrapolations and can be calculated at a fixed potential conveniently.[307]

The rejection-free KMC algorithm used in this work is described as follows:

a) Start at time $t = 0$ with an initial configuration i from a Metropolis Monte Carlo snapshot at 300 K.

b) Calculate the cumulative rate of transition up to event j: $R_{i,j} = \sum_{k=1}^{j} r_{ik}$ for $j = 1,...,N_i$, where N_i is the total number of possible events (including Volmer, Heyrovsky, Tafel, surface diffusion, and all their reverse reactions) from state i to k, $r_{ik} = v\exp(-E_a / k_B T)$ is the transition rate from state i to k, E_a is the activation energy, and v is the prefactor. The total rate is therefore R_{i,N_i}.

c) Carry out the event i to j for which $R_{i,j-1} < u_1 R_{i,N_i} \leq R_{i,j}$, where u_1 is a uniform random variable from $(0,1]$.

d) Update KMC time by $t := t + \Delta t$, where $\Delta t = R_{i,N_i}^{-1} \ln(1/u_2)$, and u_2 is another uniform random variable from $(0,1]$.

e) Go to step b).

The KMC simulation was run for 9.072×10^7 steps. The prefactor for the electrochemical reactions were chosen to be 10^9 s^{-1}, which accounts for the solvent reorganization effect at the interface.[308-309] Other events had a prefactor of 10^{13} s^{-1}. For step c), a pre-equilibration of the surface H* was performed by allowing surface diffusion of H* for at most $80\,N_{site}$ steps before a hydrogen liberation event occurs, whichever occurs first, where N_{site} is the total number of adsorption sites on the surface. This is done because of the significantly higher rate of the surface diffusion events compared to hydrogen liberation events and scaling the fast events can make the slow events sampled more efficiently. An alternative scaling scheme can be found in ref. 310.

The predicted HER current densities are shown in Figure 45a. The Heyrovsky current contributes to less than 0.01% (not shown in figure). Therefore, the Tafel mechanism is identified as the preferred mechanism on Pt(111), in agreement with the previous simulations in this work. The magnitude of the current density is comparable with that from experiment.[311-312] At potentials prior to the phase transformation from fcc to top adsorption (–0.18 V), the fcc + top pair is the most active pair of sites for the HER (< –0.08 V), which is also in agreement with the previously identified active sites. At the potential when the phase transformation occurs, the HER current density of the top + top pair exhibits a peak,

and the corresponding current density is the largest among the three pairs of sites. As the potential is further decreased, the fcc + fcc minority pair becomes the most active at more negative potentials.

These observations further validate the argument of the kinetically active, weakly adsorbed sites being the most active sites for the HER. However, it is natural to raise the question: why top + top pair is not the most active at small overpotentials (that would produce a 30 mV/dec Tafel slope seen in experiments) while fcc + fcc pair is the most active at large overpotentials? An inspection from the Monte Carlo snapshots (Figure 36) suggests that it could be due to the thermodynamics of the hydrogen adsorption. At smaller overpotentials (0 and –0.1 V), little trace of top H* is found and therefore, the probability of finding two nearby top H* is low. On the contrary, at large overpotentials the fcc H*, weakly adsorbed species, co-exists with top H* and its coverage is non-negligible. As a result, the probability of finding two nearby fcc H* is much higher than the case for top H*.

The Tafel slope transitions from 34 mV/dec at small overpotentials to 56 mV/dec prior to the phase transformation, consistent with the previously discussed coverage-dependent Tafel slopes. A Tafel slope about 60 mV/dec may indicate the fcc + top route with fcc sites saturated, as is demonstrated here and from Lindgren *et al.*[290]; a slope greater than ~30 mV/dec does not necessarily suggest a Heyrovsky mechanism. Likewise, a ~120 mV/dec slope does not necessarily suggest the Volmer step being rate-limiting; it could be either a Heyrovsky step or a Tafel step at a surface where the H* coverage is far from dilute.

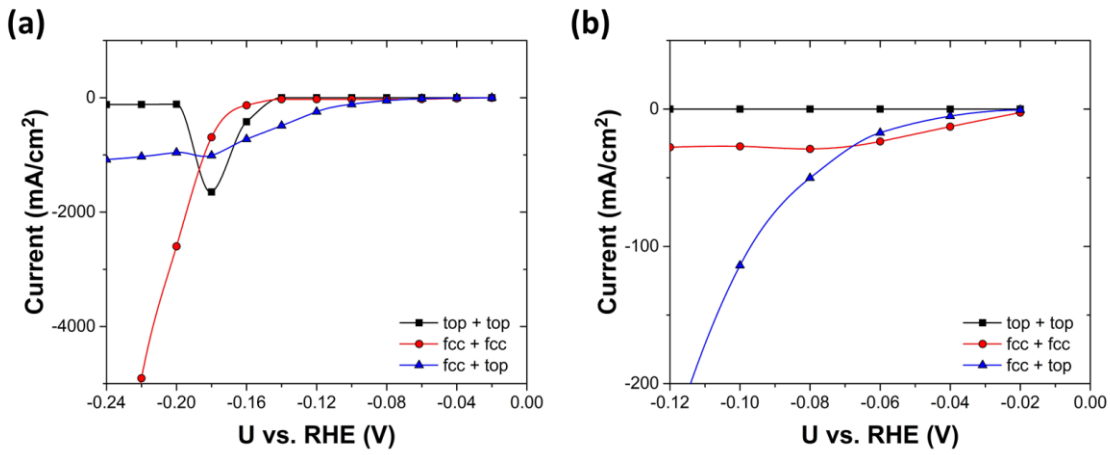

Figure 45. (a) HER current density of Pt(111) from a KMC simulation. The same plot at small overpotential is shown in (b).

The current results still cannot reach a full agreement with experimentally measured ~30 mV/dec Tafel slope; it has to be originated from two top sites where the coverage is dilute. This might be due to the limitation of the DFT calculations and methods used in this work. As a final note, the calculated adsorption energies of fcc site and top site H* and the predicted interactions between these species here will most likely differ from experiments where there are possibly *OH adsorption, cationic effect, pH effect, and electric field effect,[313-316] which need to be taken into account in the future work of theoretical modeling of electrocatalysis.

6.5.2 Other Pt surfaces

The Pt(111) surface has been studied extensively for the HER, however, other Pt surfaces are also worth investigating as they may have higher activity than that of Pt(111). In 1997, Marković *et al.*[253] measured experimentally that the activation energy for Pt(111) is the

largest, followed by Pt(100) and Pt(110), indicating that the Pt(111) is the least active and Pt(110) is the most active surface. In 1998, Conway *et al.*[311] reported that Pt(110) is the most active surface but the trend for Pt(111) and Pt(100) is opposite. Recently, activation energies have been calculated on Pt(111) and Pt(110) computationally[317-318] and they seem to support that the Pt(110) is more active than Pt(111); however, to date Pt(100) surface has not yet been modeled for the HER.

To try closing the gap, firstly, a cluster expansion on Pt(100) has been constructed using the same approach outlined in section 6.2.1. The cluster expansion included the bridge site, the top site, and the hollow site. 86 structures were in the training data, and the final LOOCV error, a measure of the predictive accuracy, was 6.4 meV per site. The snapshots of Monte Carlo simulations at 300 K are shown in Figure 46 (using the same color scale as other surfaces in the previous section).

At 0 V, the hydrogen adsorption is stronger and the coverage is higher than that on Pt(111). The coverage of the bridge site is slightly higher than 0.5 ML (here 1 ML denotes all bridge sites being occupied). The H* with colors close to white could be potentially highly active, while those with colors close to blue are the spectator species similar to the fcc sites on Pt(111). As the potential decreases (down to –0.3 V), the coverage of bridge sites keeps increasing with no apparent phase transformation to top sites being observed on Pt(100), likely due to the large difference in adsorption energies for the bridge site and top site, whereas for Pt(111) the adsorption energies for the fcc site and top site are much closer. Under the assumption that the weakly bound H* is more active for HER, the bridge sites appearing at above 0.5 ML (and possibly top sites) could be the most active sites on Pt(100).

The higher H* coverage is also in line with the higher Tafel slope than that of Pt(111) observed experimentally.[253, 312]

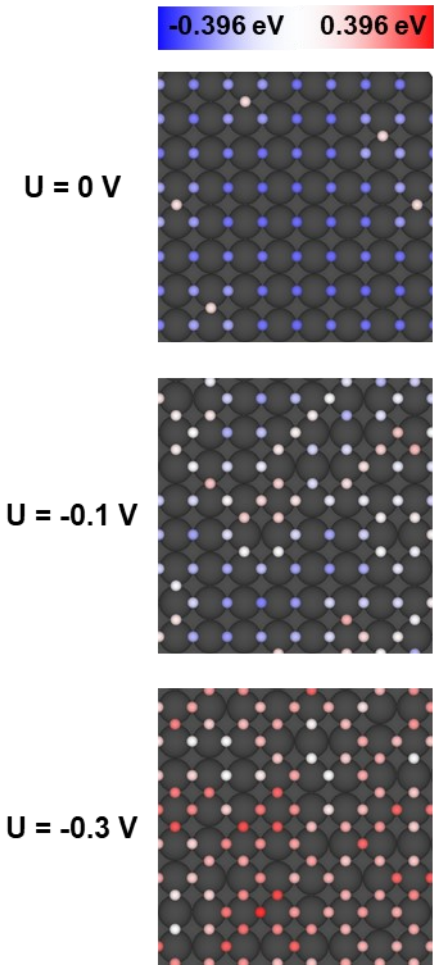

Figure 46. Snapshots of Monte Carlo simulations of adsorbed hydrogen on the surfaces of Pt(100) at 300 K with applied potentials of 0, –0.1, and –0.3 V. The colors indicate the free energies of adsorption at each site relative to H_2(g). Atomic-scale structural images were generated using VESTA.[129]

To further investigate the HER activity on Pt(100), activation barriers have been calculated. An unreconstructed surface was used as Tidswell *et al.* found that the Pt(100) surface was unreconstructed at all potentials.[319] All computational details have been consistent with

Lindgren *et al*.[290] except for the use of 4×4×3 slab here. Interestingly, the structure of H_2O layer is found to be in a buckled hexagonal geometry (Figure 47), which is about 0.1 eV (per O atom) more stable than the 4-fold planar coordination of the oxygen and hydrogen bonds[308]; however, this structure is not yet verified against experiments.

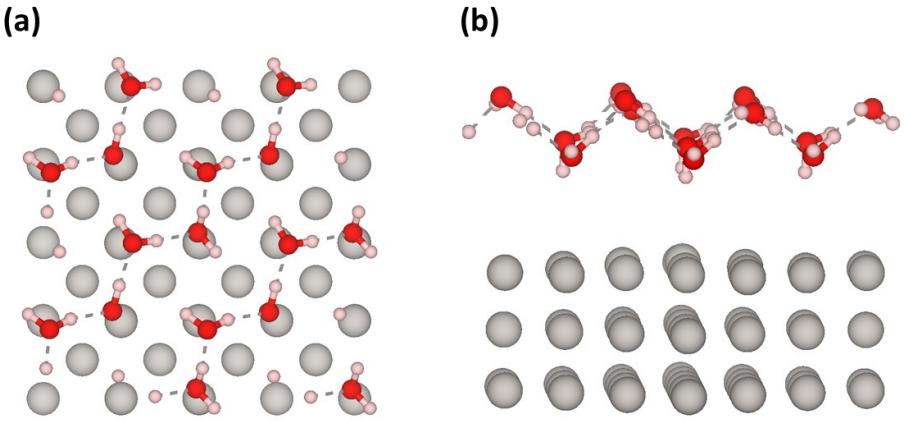

Figure 47. Structure of the Pt(100)-H_2O interface in top view and side view (Surface H* have been removed). Grey spheres represent Pt, red spheres represent O, pink spheres represent H, and dashed lines represent $H \cdots O$ hydrogen bonds. Atomic-scale structural images were generated using VESTA.[129]

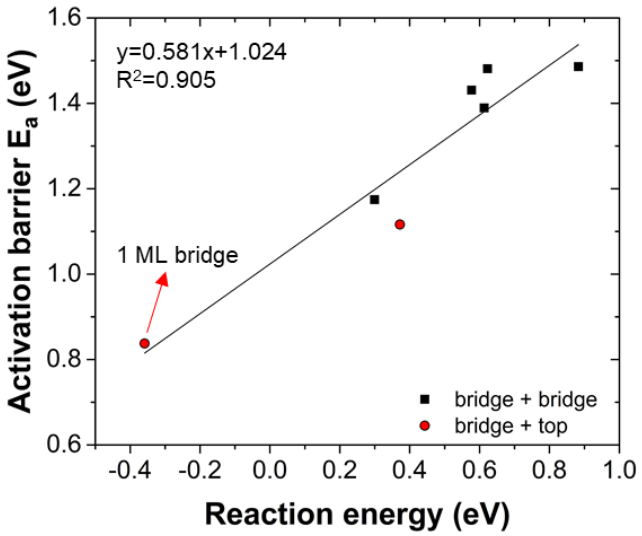

Figure 48. Activation barriers for the Tafel reactions on Pt(100). The data points are bridge + bridge, 0.5 ML bridge + top, and 1 ML bridge + top.

The calculated Tafel barriers are shown in Figure 48, including sites of bridge + bridge at various coverages, 0.5 ML bridge + top, and 1 ML bridge + top. The calculated values are in general more than 0.3 eV higher than those of Pt(111), with the smallest barrier here (0.84 eV at 1 ML bridge + top) still being ~0.2 eV higher than the fcc + top on Pt(111). Preliminary work[3] on the Heyrovsky reaction involving a top site H* suggests a barrier height of about 1.59 eV, which indicates that the Tafel mechanism (or a mixed mechanism) might be preferred on the Pt(100) surface. Taken together, the HER on Pt(100) is likely to be less active than Pt(111) even though the hydrogen coverage is higher on the Pt(100) surface. A detailed systematic study is currently underway.

[3] Unpublished work.

References

1. Ising, E., Beitrag zur Theorie des Ferromagnetismus. *Zeitschrift für Physik* **1925,** *31* (1), 253-258.
2. Sanchez, J. M.; Ducastelle, F.; Gratias, D., Generalized cluster description of multicomponent systems. *Physica A* **1984,** *128* (1), 334-350.
3. Van Baal, C. M., Order-disorder transformations in a generalized Ising alloy. *Physica* **1973,** *64* (3), 571-586.
4. Ozoliņš, V.; Wolverton, C.; Zunger, A., Cu-Au, Ag-Au, Cu-Ag, and Ni-Au Intermetallics: First-Principles Study of Temperature-Composition Phase Diagrams and Structures. *Phys. Rev. B* **1998,** *57* (11), 6427-6443.
5. Van der Ven, A.; Aydinol, M. K.; Ceder, G.; Kresse, G.; Hafner, J., First-Principles Investigation of Phase Stability in Li_xCoO_2. *Phys. Rev. B* **1998,** *58* (6), 2975-2987.
6. Van de Walle, A.; Ceder, G., Automating First-Principles Phase Diagram Calculations. *J. Phase Equilib.* **2002,** *23* (4), 348-359.
7. Mueller, T.; Ceder, G., *Ab initio* Study of the Low-Temperature Phases of Lithium Imide. *Phys. Rev. B* **2010,** *82* (17), 174307/1-174307/7.
8. Zhou, F.; Maxisch, T.; Ceder, G., Configurational Electronic Entropy and the Phase Diagram of Mixed-Valence Oxides: The Case of Li_xFePO_4. *Phys. Rev. Lett.* **2006,** *97* (15), 155704.
9. Aydinol, M. K.; Kohan, A. F.; Ceder, G., Ab initio calculation of the intercalation voltage of lithium-transition-metal oxide electrodes for rechargeable batteries. *J. Power Sources* **1997,** *68* (2), 664-668.
10. Skorodumova, N. V.; Simak, S. I.; Lundqvist, B. I.; Abrikosov, I. A.; Johansson, B., Quantum Origin of the Oxygen Storage Capability of Ceria. *Phys. Rev. Lett.* **2002,** *89* (16), 166601.
11. Lu, Z. W.; Wei, S. H.; Zunger, A.; Frota-Pessoa, S.; Ferreira, L. G., First-principles statistical mechanics of structural stability of intermetallic compounds. *Phys. Rev. B* **1991,** *44* (2), 512-544.
12. Van der Ven, A.; Ceder, G.; Asta, M.; Tepesch, P. D., First-principles theory of ionic diffusion with nondilute carriers. *Phys. Rev. B* **2001,** *64* (18), 184307.
13. Wei, S. H.; Ferreira, L. G.; Zunger, A., First-principles calculation of temperature-composition phase diagrams of semiconductor alloys. *Phys. Rev. B* **1990,** *41* (12), 8240-8269.
14. Teles, L. K.; Furthmüller, J.; Scolfaro, L. M. R.; Leite, J. R.; Bechstedt, F., First-principles calculations of the thermodynamic and structural properties of strained $In_xGa_{1-x}N$ and $Al_xGa_{1-x}N$ alloys. *Phys. Rev. B* **2000,** *62* (4), 2475-2485.
15. Sanchez, J. M.; Stark, J. P.; Moruzzi, V. L., First-principles calculation of the Ag-Cu phase diagram. *Phys. Rev. B* **1991,** *44* (11), 5411-5418.

16. Van der Ven, A.; Aydinol, M. K.; Ceder, G., First-Principles Evidence for Stage Ordering in Li_xCoO_2. *J. Electrochem. Soc.* **1998,** *145* (6), 2149-2155.
17. Laks, D. B.; Ferreira, L. G.; Froyen, S.; Zunger, A., Efficient cluster expansion for substitutional systems. *Physical Review B* **1992,** *46* (19), 12587-12605.
18. Sluiter, M.; de Fontaine, D.; Guo, X. Q.; Podloucky, R.; Freeman, A. J., First-principles calculation of phase equilibria in the aluminum lithium system. *Phys. Rev. B* **1990,** *42* (16), 10460-10476.
19. Sanati, M.; Hart, G. L. W.; Zunger, A., Ordering tendencies in octahedral MgO-ZnO alloys. *Physical Review B* **2003,** *68* (15), 155210.
20. Hao, S.; Zhao, L.-D.; Chen, C.-Q.; Dravid, V. P.; Kanatzidis, M. G.; Wolverton, C. M., Theoretical Prediction and Experimental Confirmation of Unusual Ternary Ordered Semiconductor Compounds in Sr–Pb–S System. *J. Am. Chem. Soc.* **2014,** *136* (4), 1628-1635.
21. Hart, G. L. W.; Nelson, L. J.; Vanfleet, R. R.; Campbell, B. J.; Sluiter, M. H. F.; Neethling, J. H.; Olivier, E. J.; Allies, S.; Lang, C. I.; Meredig, B.; Wolverton, C., Revisiting the revised Ag-Pt phase diagram. *Acta Mater.* **2017,** *124*, 325-332.
22. Ghosh, G.; van de Walle, A.; Asta, M., First-principles calculations of the structural and thermodynamic properties of bcc, fcc and hcp solid solutions in the Al–TM (TM=Ti, Zr and Hf) systems: A comparison of cluster expansion and supercell methods. *Acta Mater.* **2008,** *56* (13), 3202-3221.
23. Lu, Z. W.; Klein, B. M.; Zunger, A., Atomic short-range order and alloy ordering tendency in the Ag-Au system. *Modell. Simul. Mater. Sci. Eng.* **1995,** *3* (6), 753.
24. Stefan, M., Bulk and surface ordering phenomena in binary metal alloys. *J. Phys.: Condens. Matter* **2003,** *15* (34), R1429-R1500.
25. Barabash, S. V.; Blum, V.; Müller, S.; Zunger, A., Prediction of unusual stable ordered structures of Au-Pd alloys via a first-principles cluster expansion. *Phys. Rev. B* **2006,** *74* (3), 035108.
26. Ångqvist, M.; Muñoz, W. A.; Rahm, J. M.; Fransson, E.; Durniak, C.; Rozyczko, P.; Rod, T. H.; Erhart, P., ICET – A Python Library for Constructing and Sampling Alloy Cluster Expansions. *Advanced Theory and Simulations* **2019,** *2* (7), 1900015.
27. Sadigh, B.; Asta, M.; Ozoliņš, V.; Schmid, A. K.; Bartelt, N. C.; Quong, A. A.; Hwang, R. Q., Short-Range Order and Phase Stability of Surface Alloys: PdAu on Ru(0001). *Phys. Rev. Lett.* **1999,** *83* (7), 1379-1382.
28. Ruban, A. V.; Skriver, H. L., Calculated surface segregation in transition metal alloys. *Comput. Mater. Sci.* **1999,** *15* (2), 119-143.
29. Sluiter, M. H. F.; Kawazoe, Y., Cluster expansion method for adsorption: Application to hydrogen chemisorption on graphene. *Physical Review B* **2003,** *68* (8), 085410.
30. Wieckhorst, O.; Müller, S.; Hammer, L.; Heinz, K., First-Principles-Based Surface Phase Diagram of Fully Relaxed Binary Alloy Surfaces. *Phys. Rev. Lett.* **2004,** *92* (19), 195503/1-195503/4.
31. Han, B. C.; Van der Ven, A.; Ceder, G.; Hwang, B.-J., Surface Segregation and Ordering of Alloy Surfaces in the Presence of Adsorbates. *Phys. Rev. B* **2005,** *72* (20), 205409/1-205409/9.

32. Yuge, K.; Seko, A.; Kuwabara, A.; Oba, F.; Tanaka, I., Ordering and segregation of a Cu75Pt25(111) surface: A first-principles cluster expansion study. *Physical Review B* **2007,** *76* (4), 045407.
33. Lerch, D.; Wieckhorst, O.; Hammer, L.; Heinz, K.; Müller, S., Adsorbate cluster expansion for an arbitrary number of inequivalent sites. *Physical Review B* **2008,** *78* (12), 121405.
34. Chan, M. K. Y.; Reed, J.; Donadio, D.; Mueller, T.; Meng, Y. S.; Galli, G.; Ceder, G., Cluster expansion and optimization of thermal conductivity in SiGe nanowires. *Phys. Rev. B* **2010,** *81* (17), 174303.
35. Schmidt, D. J.; Chen, W.; Wolverton, C.; Schneider, W. F., Performance of Cluster Expansions of Coverage-Dependent Adsorption of Atomic Oxygen on Pt(111). *J. Chem. Theory Comput.* **2012,** *8* (1), 264-273.
36. Chen, W.; Dalach, P.; Schneider, W. F.; Wolverton, C., Interplay between Subsurface Ordering, Surface Segregation, and Adsorption on Pt–Ti(111) Near-Surface Alloys. *Langmuir* **2012,** *28* (10), 4683-4693.
37. Penev, E. S.; Bhowmick, S.; Sadrzadeh, A.; Yakobson, B. I., Polymorphism of Two-Dimensional Boron. *Nano Lett.* **2012,** *12* (5), 2441-2445.
38. Tan, T. L.; Wang, L.-L.; Johnson, D. D.; Bai, K., Hydrogen Deposition on Pt(111) during Electrochemical Hydrogen Evolution from a First-Principles Multiadsorption-Site Study. *J. Phys. Chem. C* **2013,** *117* (44), 22696-22704.
39. Hess, F.; Over, H., Rate-Determining Step or Rate-Determining Configuration? The Deacon Reaction over RuO2(110) Studied by DFT-Based KMC Simulations. *ACS Catal.* **2017,** *7* (1), 128-138.
40. Ng, M.-F.; Tan, T. L., Unveiling Stable Group IV Alloy Nanowires via a Comprehensive Search and Their Electronic Band Characteristics. *Nano Lett.* **2013,** *13* (10), 4951-4956.
41. Tan, T. L.; Jin, H. M.; Sullivan, M. B.; Anasori, B.; Gogotsi, Y., High-Throughput Survey of Ordering Configurations in MXene Alloys Across Compositions and Temperatures. *ACS Nano* **2017,** *11* (5), 4407-4418.
42. Tan, T. L.; Ng, M.-F., Computational screening for effective $Ge_{1-x}Si_x$ nanowire photocatalyst. *Phys. Chem. Chem. Phys.* **2015,** *17* (31), 20391-20397.
43. Cao, L.; Mueller, T., Rational Design of Pt3Ni Surface Structures for the Oxygen Reduction Reaction. *J. Phys. Chem. C* **2015,** *119* (31), 17735-17747.
44. Yuge, K., Segregation of $Pt_{28}Rh_{27}$ bimetallic nanoparticles: a first-principles study. *J. Phys.: Condens. Matter* **2010,** *22* (24), 245401.
45. Mueller, T.; Ceder, G., Effect of Particle Size on Hydrogen Release from Sodium Alanate Nanoparticles. *ACS Nano* **2010,** *4* (10), 5647-5656.
46. Tan, T. L.; Wang, L.-L.; Johnson, D. D.; Bai, K., A Comprehensive Search for Stable Pt-Pd Nanoalloy Configurations and Their Use as Tunable Catalysts. *Nano Lett.* **2012,** *12* (9), 4875-4880.
47. Wang, L.-L.; Tan, T. L.; Johnson, D. D., Configurational Thermodynamics of Alloyed Nanoparticles with Adsorbates. *Nano Lett.* **2014,** *14* (12), 7077-7084.
48. Yuge, K., First-Principles-based Optimization of Electronic Structures for Bimetallic Nanoparticles. *CALPHAD: Comput. Coupling Phase Diagrams Thermochem.* **2014,** *47* (0), 144-147.

49. Wang, L.-L.; Tan, T. L.; Johnson, D. D., Nanoalloy electrocatalysis: simulating cyclic voltammetry from configurational thermodynamics with adsorbates. *Phys. Chem. Chem. Phys.* **2015,** *17* (42), 28103-28111.
50. Teeriniemi, J.; Melander, M.; Lipasti, S.; Hatz, R.; Laasonen, K., Fe–Ni Nanoparticles: A Multiscale First-Principles Study to Predict Geometry, Structure, and Catalytic Activity. *J. Phys. Chem. C* **2017,** *121* (3), 1667-1674.
51. Eom, T.; Kim, W. J.; Lim, H.-K.; Han, M. H.; Han, K. H.; Lee, E.-K.; Lebègue, S.; Hwang, Y. J.; Min, B. K.; Kim, H., Cluster Expansion Method for Simulating Realistic Size of Nanoparticle Catalysts with an Application in CO2 Electroreduction. *J. Phys. Chem. C* **2018,** *122* (16), 9245-9254.
52. Tan, T. L.; Wang, L.-L.; Zhang, J.; Johnson, D. D.; Bai, K., Platinum Nanoparticle During Electrochemical Hydrogen Evolution: Adsorbate Distribution, Active Reaction Species, and Size Effect. *ACS Catal.* **2015,** *5* (4), 2376-2383.
53. Mueller, T., Ab initio determination of structure-property relationships in alloy nanoparticles. *Physical Review B* **2012,** *86* (14), 144201.
54. Huang, X.; Zhao, Z.; Cao, L.; Chen, Y.; Zhu, E.; Lin, Z.; Li, M.; Yan, A.; Zettl, A.; Wang, Y. M.; Duan, X.; Mueller, T.; Huang, Y., High-Performance Transition Metal-doped Pt_3Ni Octahedra for Oxygen Reduction Reaction. *Science* **2015,** *348* (6240), 1230-1234.
55. Cao, L.; Mueller, T., Theoretical Insights into the Effects of Oxidation and Mo-Doping on the Structure and Stability of Pt-Ni Nanoparticles *Nano Lett.* **2016,** *16* (12), 7748-7754.
56. Jia, Q.; Zhao, Z.; Cao, L.; Li, J.; Ghoshal, S.; Davies, V.; Stavitski, E.; Attenkofer, K.; Li, M.; Duan, X.; Mukerjee, S.; Mueller, T.; Huang, Y., Roles of Mo Surface Dopants in Enhancing the ORR Performance of Octahedral PtNi Nanoparticles. *Nano Lett.* **2018,** *18* (2), 798-804.
57. Li, C.; Raciti, D.; Pu, T.; Cao, L.; He, C.; Wang, C.; Mueller, T., Improved Prediction of Nanoalloy Structures by the Explicit Inclusion of Adsorbates in Cluster Expansions. *J. Phys. Chem. C* **2018,** *122* (31), 18040-18047.
58. Yuge, K., Concentration effects on segregation behavior of Pt-Rh nanoparticles. *Phys. Rev. B* **2011,** *84* (8), 085451.
59. Wei, S.; Chou, M. Y., First-principles determination of equilibrium crystal shapes for metals at T=0. *Phys. Rev. B* **1994,** *50* (7), 4859-4862.
60. Chepulskii, R. V.; Butler, W. H., Temperature and particle-size dependence of the equilibrium order parameter of FePt alloys. *Physical Review B* **2005,** *72* (13), 134205.
61. Chepulskii, R. V.; Butler, W. H.; van de Walle, A.; Curtarolo, S., Surface segregation in nanoparticles from first principles: The case of FePt. *Scripta Mater.* **2010,** *62* (4), 179-182.
62. Weitzner, S. E.; Dabo, I., Voltage effects on the stability of Pd ensembles in Pd–Au/Au(111) surface alloys. *The Journal of Chemical Physics* **2019,** *150* (4), 041715.
63. Chowdhury, T.; Kim, J.; Sadler, E. C.; Li, C.; Lee, S. W.; Jo, K.; Xu, W.; Gracias, D. H.; Drichko, N. V.; Jariwala, D.; Brintlinger, T. H.; Mueller, T.; Park, H.-G.; Kempa, T. J., Substrate-directed synthesis of MoS2 nanocrystals with tunable dimensionality and optical properties. *Nature Nanotechnology* **2020,** *15* (1), 29-34.
64. Mueller, T.; Ceder, G., Exact expressions for structure selection in cluster expansions. *Physical Review B* **2010,** *82* (18), 184107.

65. Tikhonov, A. N.; Arsenin, V. Y., Solutions of Ill-Posed Problems. *John Wiley & Sons* **1977**.
66. Mueller, T.; Kusne, A. G.; Ramprasad, R., Machine learning in materials science: Recent progress and emerging applications. In *Rev. Comput. Chem.*, 2016; pp 186-273.
67. Mueller, T.; Ceder, G., Bayesian approach to cluster expansions. *Physical Review B* **2009,** *80* (2), 024103.
68. Seko, A.; Koyama, Y.; Tanaka, I., Cluster expansion method for multicomponent systems based on optimal selection of structures for density-functional theory calculations. *Phys. Rev. B* **2009,** *80* (16), 165122.
69. Cockayne, E.; van de Walle, A., Building effective models from sparse but precise data: Application to an alloy cluster expansion model. *Phys. Rev. B* **2010,** *81* (1), 012104.
70. Nelson, L. J.; Hart, G. L. W.; Zhou, F.; Ozoliņš, V., Compressive sensing as a paradigm for building physics models. *Phys. Rev. B* **2013,** *87* (3), 035125.
71. Tibshirani, R., Regression Shrinkage and Selection via the Lasso. *J. R. Statist. Soc. B* **1996,** *58* (1), 267-288.
72. Cao, L.; Li, C.; Mueller, T., The Use of Cluster Expansions To Predict the Structures and Properties of Surfaces and Nanostructured Materials. *Journal of Chemical Information and Modeling* **2018,** *58* (12), 2401-2413.
73. Mueller, T. Computational studies of hydrogen storage materials and the development of related methods. Massachusetts Institute of Technology, Cambridge, MA, 2007.
74. Leong, Z.; Tan, T. L., Robust cluster expansion of multicomponent systems using structured sparsity. *Physical Review B* **2019,** *100* (13), 134108.
75. Cao, L.; Niu, L.; Mueller, T., Computationally generated maps of surface structures and catalytic activities for alloy phase diagrams. *Proceedings of the National Academy of Sciences* **2019,** *116* (44), 22044.
76. Jia, Q.; Zhao, Z.; Cao, L.; Li, J.; Ghoshal, S.; Davies, V.; Stavitski, E.; Attenkofer, K.; Liu, Z.; Li, M.; Duan, X.; Mukerjee, S.; Mueller, T.; Huang, Y., Roles of Mo Surface Dopants in Enhancing the ORR Performance of Octahedral PtNi Nanoparticles. *Nano Lett.* **2018,** *18* (2), 798-804.
77. Tan, T. L.; Wang, L.-L.; Johnson, D. D.; Bai, K., A Comprehensive Search for Stable Pt–Pd Nanoalloy Configurations and Their Use as Tunable Catalysts. *Nano Letters* **2012,** *12* (9), 4875-4880.
78. Cao, L.; Mueller, T., Theoretical Insights into the Effects of Oxidation and Mo-Doping on the Structure and Stability of Pt–Ni Nanoparticles. *Nano Lett.* **2016,** *16* (12), 7748-7754.
79. Huang, X.; Zhao, Z.; Cao, L.; Chen, Y.; Zhu, E.; Lin, Z.; Li, M.; Yan, A.; Zettl, A.; Wang, Y. M.; Duan, X.; Mueller, T.; Huang, Y., High-performance transition metal–doped Pt3Ni octahedra for oxygen reduction reaction. *Science* **2015,** *348* (6240), 1230-1234.
80. Rodriguez, J., Physical and chemical properties of bimetallic surfaces. *Surf. Sci. Rep.* **1996,** *24* (7), 223-287.
81. Ferrando, R.; Jellinek, J.; Johnston, R. L., Nanoalloys: From Theory to Applications of Alloy Clusters and Nanoparticles. *Chem. Rev.* **2008,** *108* (3), 845-910.
82. Hagen, J., Industrial catalysis: a practical approach. 2nd, completely rev. and extended. *Weinheim: Wiley-VCH* **2006,** *xviii*, 507.

83. Kitchin, J. R.; Miller, S. D.; Sholl, D. S., Density functional theory studies of alloys in heterogeneous catalysis. In *Chemical Modelling: Applications and Theory Volume 5*, The Royal Society of Chemistry: 2008; Vol. 5, pp 150-181.
84. Kohn, W.; Sham, L. J., Self-Consistent Equations Including Exchange and Correlation Effects. *Physical Review* **1965,** *140* (4A), A1133-A1138.
85. Kresse, G.; Furthmüller, J., Efficient iterative schemes for ab initio total-energy calculations using a plane-wave basis set. *Physical Review B* **1996,** *54* (16), 11169-11186.
86. Alayoglu, S.; Nilekar, A. U.; Mavrikakis, M.; Eichhorn, B., Ru–Pt core–shell nanoparticles for preferential oxidation of carbon monoxide in hydrogen. *Nature Materials* **2008,** *7*, 333.
87. Lim, D.-H.; Wilcox, J., DFT-Based Study on Oxygen Adsorption on Defective Graphene-Supported Pt Nanoparticles. *J. Phys. Chem. C* **2011,** *115* (46), 22742-22747.
88. Stamenkovic, V.; Mun, B. S.; Mayrhofer, K. J. J.; Ross, P. N.; Markovic, N. M.; Rossmeisl, J.; Greeley, J.; Nørskov, J. K., Changing the Activity of Electrocatalysts for Oxygen Reduction by Tuning the Surface Electronic Structure. *Angew. Chem.* **2006,** *118* (18), 2963-2967.
89. Stamenkovic, V. R.; Fowler, B.; Mun, B. S.; Wang, G.; Ross, P. N.; Lucas, C. A.; Marković, N. M., Improved Oxygen Reduction Activity on Pt3Ni(111) via Increased Surface Site Availability. *Science* **2007,** *315* (5811), 493.
90. Yudanov, I. V.; Genest, A.; Schauermann, S.; Freund, H.-J.; Rösch, N., Size Dependence of the Adsorption Energy of CO on Metal Nanoparticles: A DFT Search for the Minimum Value. *Nano Lett.* **2012,** *12* (4), 2134-2139.
91. Han, B. C.; Miranda, C. R.; Ceder, G., Effect of particle size and surface structure on adsorption of O and OH on platinum nanoparticles: A first-principles study. *Physical Review B* **2008,** *77* (7), 075410.
92. Metropolis, N.; Rosenbluth, A. W.; Rosenbluth, M. N.; Teller, A. H.; Teller, E., Equation of State Calculations by Fast Computing Machines. *The Journal of Chemical Physics* **1953,** *21* (6), 1087-1092.
93. Greeley, J.; Stephens, I. E. L.; Bondarenko, A. S.; Johansson, T. P.; Hansen, H. A.; Jaramillo, T. F.; Rossmeisl, J.; Chorkendorff, I.; Nørskov, J. K., Alloys of platinum and early transition metals as oxygen reduction electrocatalysts. *Nat. Chem.* **2009,** *1* (7), 552-556.
94. Matanović, I.; Garzon, F. H.; Henson, N. J., Theoretical Study of Electrochemical Processes on Pt–Ni Alloys. *J. Phys. Chem. C* **2011,** *115* (21), 10640-10650.
95. Sun, X.; Jiang, K.; Zhang, N.; Guo, S.; Huang, X., Crystalline Control of {111} Bounded Pt3Cu Nanocrystals: Multiply-Twinned Pt3Cu Icosahedra with Enhanced Electrocatalytic Properties. *ACS Nano* **2015,** *9* (7), 7634-7640.
96. Stamenkovic, V. R.; Mun, B. S.; Mayrhofer, K. J. J.; Ross, P. N.; Markovic, N. M., Effect of Surface Composition on Electronic Structure, Stability, and Electrocatalytic Properties of Pt-Transition Metal Alloys: Pt-Skin versus Pt-Skeleton Surfaces. *J. Am. Chem. Soc.* **2006,** *128* (27), 8813-8819.
97. Fowler, B.; Lucas, C. A.; Omer, A.; Wang, G.; Stamenković, V. R.; Marković, N. M., Segregation and stability at Pt3Ni(111) surfaces and Pt75Ni25 nanoparticles. *Electrochim. Acta* **2008,** *53* (21), 6076-6080.
98. Gland, J. L.; Sexton, B. A.; Fisher, G. B., Oxygen interactions with the Pt(111) surface. *Surf. Sci.* **1980,** *95* (2), 587-602.

99. Mani, P.; Srivastava, R.; Strasser, P., Dealloyed Pt−Cu Core−Shell Nanoparticle Electrocatalysts for Use in PEM Fuel Cell Cathodes. *J. Phys. Chem. C* **2008,** *112* (7), 2770-2778.
100. Raciti, D.; Liu, Z.; Chi, M.; Wang, C., Recent Development of Platinum-Based Nanocatalysts for Oxygen Reduction Electrocatalysis. In *Nanomaterials for Fuel Cell Catalysis*, Ozoemena, K. I.; Chen, S., Eds. Springer International Publishing: Cham, 2016; pp 253-280.
101. Yoshio, H.; Akira, M.; Shin-ya, I., Enhanced Evolution of CO and Suppressed Formation of Hydrocarbons in Electroreduction of CO2 at a Copper Electrode Modified with Cadmium. *Chem. Lett.* **1990,** *19* (7), 1231-1234.
102. Watanabe, M.; Shibata, M.; Kato, A.; Azuma, M.; Sakata, T., Design of Alloy Electrocatalysts for CO 2 Reduction: III . The Selective and Reversible Reduction of on Cu Alloy Electrodes. *J. Electrochem. Soc.* **1991,** *138* (11), 3382-3389.
103. Peterson, A. A.; Abild-Pedersen, F.; Studt, F.; Rossmeisl, J.; Norskov, J. K., How copper catalyzes the electroreduction of carbon dioxide into hydrocarbon fuels. *Energy & Environmental Science* **2010,** *3* (9), 1311-1315.
104. Hori, Y.; Murata, A.; Takahashi, R., Formation of hydrocarbons in the electrochemical reduction of carbon dioxide at a copper electrode in aqueous solution. *Journal of the Chemical Society, Faraday Transactions 1: Physical Chemistry in Condensed Phases* **1989,** *85* (8), 2309-2326.
105. Calle-Vallejo, F.; Koper, M. T. M., Theoretical Considerations on the Electroreduction of CO to C2 Species on Cu(100) Electrodes. *Angew. Chem. Int. Ed.* **2013,** *52* (28), 7282-7285.
106. Raciti, D.; Cao, L.; Livi, K. J. T.; Rottmann, P. F.; Tang, X.; Li, C.; Hicks, Z.; Bowen, K. H.; Hemker, K. J.; Mueller, T.; Wang, C., Low-Overpotential Electroreduction of Carbon Monoxide Using Copper Nanowires. *ACS Catal.* **2017**, 4467-4472.
107. Cao, L.; Raciti, D.; Li, C.; Livi, K. J. T.; Rottmann, P. F.; Hemker, K. J.; Mueller, T.; Wang, C., Mechanistic Insights for Low-Overpotential Electroreduction of CO2 to CO on Copper Nanowires. *ACS Catal.* **2017,** *7* (12), 8578-8587.
108. van de Walle, A.; Ceder, G., Automating first-principles phase diagram calculations. *Journal of Phase Equilibria* **2002,** *23* (4), 348.
109. Perdew, J. P.; Burke, K.; Ernzerhof, M., Generalized Gradient Approximation Made Simple. *Phys. Rev. Lett.* **1996,** *77* (18), 3865-3868.
110. Blöchl, P. E., Projector augmented-wave method. *Physical Review B* **1994,** *50* (24), 17953-17979.
111. Wisesa, P.; McGill, K. A.; Mueller, T., Efficient generation of generalized Monkhorst-Pack grids through the use of informatics. *Physical Review B* **2016,** *93* (15), 155109.
112. Methfessel, M.; Paxton, A. T., High-precision sampling for Brillouin-zone integration in metals. *Physical Review B* **1989,** *40* (6), 3616-3621.
113. NIST-JANAF Thermochemical Tables (http://kinetics.nist.gov/janaf/). National Institute of Standards and Technology.
114. Hammer, B.; Hansen, L. B.; Nørskov, J. K., Improved adsorption energetics within density-functional theory using revised Perdew-Burke-Ernzerhof functionals. *Physical Review B* **1999,** *59* (11), 7413-7421.

115. Wang, L.; Maxisch, T.; Ceder, G., Oxidation energies of transition metal oxides within the GGA+U framework. *Physical Review B* **2006,** *73* (19), 195107.
116. Vegard, L., Die Konstitution der Mischkristalle und die Raumfüllung der Atome. *Zeitschrift für Physik* **1921,** *5* (1), 17-26.
117. Leontyev, I. N.; Kuriganova, A. B.; Leontyev, N. G.; Hennet, L.; Rakhmatullin, A.; Smirnova, N. V.; Dmitriev, V., Size dependence of the lattice parameters of carbon supported platinum nanoparticles: X-ray diffraction analysis and theoretical considerations. *RSC Advances* **2014,** *4* (68), 35959-35965.
118. Qi, W. H.; Wang, M. P., Size and shape dependent lattice parameters of metallic nanoparticles. *J. Nanopart. Res.* **2005,** *7* (1), 51-57.
119. Wasserman, H. J.; Vermaak, J. S., On the determination of the surface stress of copper and platinum. *Surf. Sci.* **1972,** *32* (1), 168-174.
120. Stephens, I. E. L.; Bondarenko, A. S.; Perez-Alonso, F. J.; Calle-Vallejo, F.; Bech, L.; Johansson, T. P.; Jepsen, A. K.; Frydendal, R.; Knudsen, B. P.; Rossmeisl, J.; Chorkendorff, I., Tuning the Activity of Pt(111) for Oxygen Electroreduction by Subsurface Alloying. *J. Am. Chem. Soc.* **2011,** *133* (14), 5485-5491.
121. Knudsen, J.; Nilekar, A. U.; Vang, R. T.; Schnadt, J.; Kunkes, E. L.; Dumesic, J. A.; Mavrikakis, M.; Besenbacher, F., A Cu/Pt Near-Surface Alloy for Water−Gas Shift Catalysis. *J. Am. Chem. Soc.* **2007,** *129* (20), 6485-6490.
122. Shan, J.; Zhang, S.; Choksi, T.; Nguyen, L.; Bonifacio, C. S.; Li, Y.; Zhu, W.; Tang, Y.; Zhang, Y.; Yang, J. C.; Greeley, J.; Frenkel, A. I.; Tao, F., Tuning Catalytic Performance through a Single or Sequential Post-Synthesis Reaction(s) in a Gas Phase. *ACS Catal.* **2017,** *7* (1), 191-204.
123. Dutta, I.; Carpenter, M. K.; Balogh, M. P.; Ziegelbauer, J. M.; Moylan, T. E.; Atwan, M. H.; Irish, N. P., Electrochemical and Structural Study of a Chemically Dealloyed PtCu Oxygen Reduction Catalyst. *J. Phys. Chem. C* **2010,** *114* (39), 16309-16320.
124. Ferreira, P. J.; Shao-Horn, Y., Formation Mechanism of Pt Single-Crystal Nanoparticles in Proton Exchange Membrane Fuel Cells. *Electrochem. Solid-State Lett.* **2007,** *10* (3), B60-B63.
125. Liao, H.-G.; Zherebetskyy, D.; Xin, H.; Czarnik, C.; Ercius, P.; Elmlund, H.; Pan, M.; Wang, L.-W.; Zheng, H., Facet development during platinum nanocube growth. *Science* **2014,** *345* (6199), 916.
126. Abe, T.; Sundman, B.; Onodera, H., Thermodynamic assessment of the Cu−Pt system. *Journal of Phase Equilibria and Diffusion* **2006,** *27* (1), 5-13.
127. Liu, T.; Wang, K.; Yuan, Q.; Shen, Z.; Wang, Y.; Zhang, Q.; Wang, X., Monodispersed sub-5.0 nm PtCu nanoalloys as enhanced bifunctional electrocatalysts for oxygen reduction reaction and ethanol oxidation reaction. *Nanoscale* **2017,** *9* (9), 2963-2968.
128. Bele, M.; Jovanovic, P.; Pavlisic, A.; Jozinovic, B.; Zorko, M.; Recnik, A.; Chernyshova, E.; Hocevar, S.; Hodnik, N.; Gaberscek, M., A highly active PtCu3 intermetallic core-shell, multilayered Pt-skin, carbon embedded electrocatalyst produced by a scale-up sol-gel synthesis. *Chem. Commun.* **2014,** *50* (86), 13124-13126.
129. Momma, K.; Izumi, F., VESTA: a three-dimensional visualization system for electronic and structural analysis. *J. Appl. Crystallogr.* **2008,** *41* (3), 653-658.

130. Zucker, R. V.; Chatain, D.; Dahmen, U.; Hagège, S.; Carter, W. C., New software tools for the calculation and display of isolated and attached interfacial-energy minimizing particle shapes. *Journal of Materials Science* **2012,** *47* (24), 8290-8302.
131. Wang, Y.; Cao, L.; Libretto, N. J.; Li, X.; Li, C.; Wan, Y.; He, C.; Lee, J.; Gregg, J.; Zong, H.; Su, D.; Miller, J. T.; Mueller, T.; Wang, C., Ensemble Effect in Bimetallic Electrocatalysts for CO2 Reduction. *J. Am. Chem. Soc.* **2019,** *141* (42), 16635-16642.
132. Han, B. C.; Van der Ven, A.; Ceder, G.; Hwang, B.-J., Surface segregation and ordering of alloy surfaces in the presence of adsorbates. *Physical Review B* **2005,** *72* (20), 205409.
133. Kim, D.; Xie, C.; Becknell, N.; Yu, Y.; Karamad, M.; Chan, K.; Crumlin, E. J.; Nørskov, J. K.; Yang, P., Electrochemical Activation of CO2 through Atomic Ordering Transformations of AuCu Nanoparticles. *J. Am. Chem. Soc.* **2017,** *139* (24), 8329-8336.
134. Tao, F.; Grass, M. E.; Zhang, Y.; Butcher, D. R.; Renzas, J. R.; Liu, Z.; Chung, J. Y.; Mun, B. S.; Salmeron, M.; Somorjai, G. A., Reaction-Driven Restructuring of Rh-Pd and Pt-Pd Core-Shell Nanoparticles. *Science* **2008,** *322* (5903), 932.
135. Huang, J.; Song, Y.; Ma, D.; Zheng, Y.; Chen, M.; Wan, H., The effect of the support on the surface composition of PtCu alloy nanocatalysts: In situ XPS and HS-LEIS studies. *Chinese Journal of Catalysis* **2017,** *38* (7), 1229-1236.
136. Andersson, K. J.; Calle-Vallejo, F.; Rossmeisl, J.; Chorkendorff, I., Adsorption-Driven Surface Segregation of the Less Reactive Alloy Component. *J. Am. Chem. Soc.* **2009,** *131* (6), 2404-2407.
137. Kim, M. H.; Ebner, J. R.; Friedman, R. M.; Vannice, M. A., Determination of Metal Dispersion and Surface Composition in Supported Cu–Pt Catalysts. *J. Catal.* **2002,** *208* (2), 381-392.
138. Nørskov, J. K.; Rossmeisl, J.; Logadottir, A.; Lindqvist, L.; Kitchin, J. R.; Bligaard, T.; Jónsson, H., Origin of the Overpotential for Oxygen Reduction at a Fuel-Cell Cathode. *The Journal of Physical Chemistry B* **2004,** *108* (46), 17886-17892.
139. Callister, W. D.; Rethwisch, D. G., *Materials Science and Engineering: An Introduction, 10th Edition*. Wiley: 2018.
140. Cao, L.; Zhao, Z.; Liu, Z.; Gao, W.; Dai, S.; Gha, J.; Xue, W.; Sun, H.; Duan, X.; Pan, X.; Mueller, T.; Huang, Y., Differential Surface Elemental Distribution Leads to Significantly Enhanced Stability of PtNi-Based ORR Catalysts. *Matter* **2019,** *1* (6), 1567-1580.
141. Sun, D.; Wang, Y.; Livi, K. J. T.; Wang, C.; Luo, R.; Zhang, Z.; Alghamdi, H.; Li, C.; An, F.; Gaskey, B.; Mueller, T.; Hall, A. S., Ordered Intermetallic Pd3Bi Prepared by an Electrochemically Induced Phase Transformation for Oxygen Reduction Electrocatalysis. *ACS Nano* **2019,** *13* (9), 10818-10825.
142. Fang, W.; Chen, J.; Pedevilla, P.; Li, X.-Z.; Richardson, J. O.; Michaelides, A., Origins of fast diffusion of water dimers on surfaces. *Nature Communications* **2020,** *11* (1), 1689.
143. Kawahara, K.; Ohko, Y.; Tatsuma, T.; Fujishima, A., Surface diffusion behavior of photo-generated active species or holes on TiO2 photocatalysts. *PCCP* **2003,** *5* (21), 4764-4766.
144. Kunz, L.; Kuhn, F. M.; Deutschmann, O., Kinetic Monte Carlo simulations of surface reactions on supported nanoparticles: A novel approach and computer code. *The Journal of Chemical Physics* **2015,** *143* (4), 044108.

145. Ong, S. P.; Chevrier, V. L.; Hautier, G.; Jain, A.; Moore, C.; Kim, S.; Ma, X.; Ceder, G., Voltage, stability and diffusion barrier differences between sodium-ion and lithium-ion intercalation materials. *Energy & Environmental Science* **2011,** *4* (9), 3680-3688.
146. Wang, C.; Aoyagi, K.; Wisesa, P.; Mueller, T., Lithium Ion Conduction in Cathode Coating Materials from On-the-Fly Machine Learning. *Chem. Mater.* **2020,** *32* (9), 3741-3752.
147. Islam, M. S.; Fisher, C. A. J., Lithium and sodium battery cathode materials: computational insights into voltage, diffusion and nanostructural properties. *Chem. Soc. Rev.* **2014,** *43* (1), 185-204.
148. Li, W.; Yang, Y.; Zhang, G.; Zhang, Y.-W., Ultrafast and Directional Diffusion of Lithium in Phosphorene for High-Performance Lithium-Ion Battery. *Nano Lett.* **2015,** *15* (3), 1691-1697.
149. Haugsrud, R.; Norby, T., Proton conduction in rare-earth ortho-niobates and ortho-tantalates. *Nature Materials* **2006,** *5* (3), 193-196.
150. Wisesa, P.; Li, C.; Wang, C.; Mueller, T., Materials with the CrVO4 structure type as candidate superprotonic conductors. *RSC Advances* **2019,** *9* (55), 31999-32009.
151. Mitra, C.; Meyer, T.; Lee, H. N.; Reboredo, F. A., Oxygen diffusion pathways in brownmillerite SrCoO2.5: Influence of structure and chemical potential. *The Journal of Chemical Physics* **2014,** *141* (8), 084710.
152. Kreuer, K.-D., Proton Conductivity: Materials and Applications. *Chem. Mater.* **1996,** *8* (3), 610-641.
153. Edmonds, K. W.; Bogusławski, P.; Wang, K. Y.; Campion, R. P.; Novikov, S. N.; Farley, N. R. S.; Gallagher, B. L.; Foxon, C. T.; Sawicki, M.; Dietl, T.; Buongiorno Nardelli, M.; Bernholc, J., Mn Interstitial Diffusion in (Ga,Mn)As. *Phys. Rev. Lett.* **2004,** *92* (3), 037201.
154. Istratov, A. A.; Flink, C.; Hieslmair, H.; Weber, E. R.; Heiser, T., Intrinsic Diffusion Coefficient of Interstitial Copper in Silicon. *Phys. Rev. Lett.* **1998,** *81* (6), 1243-1246.
155. Ceriotti, M.; Cereda, S.; Montalenti, F.; Miglio, L.; Bernasconi, M., Ab initio study of the diffusion and decomposition pathways of SiHx species on Si(100). *Physical Review B* **2009,** *79* (16), 165437.
156. Jung, H. J.; Kim, D.; Kim, S.; Park, J.; Dravid, V. P.; Shin, B., Stability of Halide Perovskite Solar Cell Devices: In Situ Observation of Oxygen Diffusion under Biasing. *Adv. Mater.* **2018,** *30* (39), 1802769.
157. Bortz, A. B.; Kalos, M. H.; Lebowitz, J. L., A new algorithm for Monte Carlo simulation of Ising spin systems. *Journal of Computational Physics* **1975,** *17* (1), 10-18.
158. Kolokathis, P. D.; Theodorou, D. N., On solving the master equation in spatially periodic systems. *The Journal of Chemical Physics* **2012,** *137* (3), 034112.
159. Vineyard, G. H., Frequency factors and isotope effects in solid state rate processes. *J. Phys. Chem. Solids* **1957,** *3* (1), 121-127.
160. Gilmer, G. H., Computer Models of Crystal Growth. *Science* **1980,** *208* (4442), 355-363.
161. Erlebacher, J.; Aziz, M. J.; Karma, A.; Dimitrov, N.; Sieradzki, K., Evolution of nanoporosity in dealloying. *Nature* **2001,** *410* (6827), 450-453.

162. Erlebacher, J., An Atomistic Description of Dealloying: Porosity Evolution, the Critical Potential, and Rate-Limiting Behavior. *J. Electrochem. Soc.* **2004,** *151* (10), C614-C626.
163. Puchala, B.; Lin, S.-k.; Wang, L.; Morgan, D., PEMFC Nanoparticle Catalyst Dealloying from Kinetic Monte Carlo Simulations. *ECS Transactions* **2013,** *50* (2), 1643-1649.
164. Tian, Y.; Jiao, W.; Liu, P.; Song, S.; Lu, Z.; Hirata, A.; Chen, M., Fast coalescence of metallic glass nanoparticles. *Nature Communications* **2019,** *10* (1), 5249.
165. Meakin, P.; Rosso, K. M., Simple kinetic Monte Carlo models for dissolution pitting induced by crystal defects. *The Journal of Chemical Physics* **2008,** *129* (20), 204106.
166. Lim, T. H.; McCarthy, D.; Hendy, S. C.; Stevens, K. J.; Brown, S. A.; Tilley, R. D., Real-Time TEM and Kinetic Monte Carlo Studies of the Coalescence of Decahedral Gold Nanoparticles. *ACS Nano* **2009,** *3* (11), 3809-3813.
167. Li, L.; Plessow, P. N.; Rieger, M.; Sauer, S.; Sánchez-Carrera, R. S.; Schaefer, A.; Abild-Pedersen, F., Modeling the Migration of Platinum Nanoparticles on Surfaces Using a Kinetic Monte Carlo Approach. *J. Phys. Chem. C* **2017,** *121* (8), 4261-4269.
168. Marcus, R. A., On the Theory of Oxidation-Reduction Reactions Involving Electron Transfer. I. *The Journal of Chemical Physics* **1956,** *24* (5), 966-978.
169. Xiao, P.; Henkelman, G., Kinetic Monte Carlo Study of Li Intercalation in LiFePO4. *ACS Nano* **2018,** *12* (1), 844-851.
170. Lindgren, P.; Kastlunger, G.; Peterson, A. A., A challenge to the Delta G~0 interpretation of hydrogen evolution. *arXiv: 1903.09903 [physics. chem-ph]* **2019**.
171. Lu, H.-J.; Zou, N.; Jacobs, R.; Afflerbach, B.; Lu, X.-G.; Morgan, D., Error assessment and optimal cross-validation approaches in machine learning applied to impurity diffusion. *Computational Materials Science* **2019,** *169*, 109075.
172. Messina, L.; Quaglino, A.; Goryaeva, A.; Marinica, M.-C.; Domain, C.; Castin, N.; Bonny, G.; Krause, R., Smart energy models for atomistic simulations using a DFT-driven multifidelity approach. *arXiv: 1808.06935 [physics. chem-ph]* **2018**.
173. Wu, H.; Lorenson, A.; Anderson, B.; Witteman, L.; Wu, H.; Meredig, B.; Morgan, D., Robust FCC solute diffusion predictions from ab-initio machine learning methods. *Computational Materials Science* **2017,** *134*, 160-165.
174. Li, W.; Ando, Y.; Minamitani, E.; Watanabe, S., Study of Li atom diffusion in amorphous Li3PO4 with neural network potential. *The Journal of Chemical Physics* **2017,** *147* (21), 214106.
175. Kondati Natarajan, S.; Behler, J., Self-Diffusion of Surface Defects at Copper–Water Interfaces. *J. Phys. Chem. C* **2017,** *121* (8), 4368-4383.
176. Kong, X.-S.; He, K.-N.; Hou, J.; Zhang, T.; Liu, C. S., Predicting Transition Metal Solute Diffusion in Metals by Merging First-Principles Calculations and Machine Learning. *http://dx.doi.org/10.2139/ssrn.3406950* **2019**.
177. Zeng, Y.; Li, Q.; Bai, K., Prediction of interstitial diffusion activation energies of nitrogen, oxygen, boron and carbon in bcc, fcc, and hcp metals using machine learning. *Computational Materials Science* **2018,** *144*, 232-247.
178. Hernandez, A.; Balasubramanian, A.; Yuan, F.; Mason, S. A. M.; Mueller, T., Fast, accurate, and transferable many-body interatomic potentials by symbolic regression. *npj Computational Materials* **2019,** *5* (1), 112.

179. Henkelman, G.; Jónsson, H., Long time scale kinetic Monte Carlo simulations without lattice approximation and predefined event table. *The Journal of Chemical Physics* **2001,** *115* (21), 9657-9666.
180. Trochet, M.; Mousseau, N.; Béland, L. K.; Henkelman, G., Off-Lattice Kinetic Monte Carlo Methods. *In: Andreoni W., Yip S. (eds) Handbook of Materials Modeling. Springer, Cham.* **2020**.
181. Van der Ven, A.; Aydinol, M. K.; Ceder, G.; Kresse, G.; Hafner, J., First-principles investigation of phase stability in LixCoO2. *Physical Review B* **1998,** *58* (6), 2975-2987.
182. Sadigh, B.; Asta, M.; Ozoliņš, V.; Schmid, A. K.; Bartelt, N. C.; Quong, A. A.; Hwang, R. Q., Short-Range Order and Phase Stability of Surface Alloys: PdAu on Ru(0001). *Phys. Rev. Lett.* **1999,** *83* (7), 1379-1382.
183. Wieckhorst, O.; Müller, S.; Hammer, L.; Heinz, K., First-Principles-Based Surface Phase Diagram of Fully Relaxed Binary Alloy Surfaces. *Phys. Rev. Lett.* **2004,** *92* (19), 195503.
184. Yuge, K., Segregation of Pt28Rh27bimetallic nanoparticles: a first-principles study. *J. Phys.: Condens. Matter* **2010,** *22* (24), 245401.
185. Nyshadham, C.; Rupp, M.; Bekker, B.; Shapeev, A. V.; Mueller, T.; Rosenbrock, C. W.; Csányi, G.; Wingate, D. W.; Hart, G. L. W., Machine-learned multi-system surrogate models for materials prediction. *npj Computational Materials* **2019,** *5* (1), 51.
186. Rehman, T.; Jaipal, M.; Chatterjee, A., A cluster expansion model for predicting activation barrier of atomic processes. *Journal of Computational Physics* **2013,** *243*, 244-259.
187. Cui, C.; Gan, L.; Heggen, M.; Rudi, S.; Strasser, P., Compositional segregation in shaped Pt alloy nanoparticles and their structural behaviour during electrocatalysis. *Nature Materials* **2013,** *12*, 765.
188. Huang, X.; Zhu, E.; Chen, Y.; Li, Y.; Chiu, C.-Y.; Xu, Y.; Lin, Z.; Duan, X.; Huang, Y., A Facile Strategy to Pt3Ni Nanocrystals with Highly Porous Features as an Enhanced Oxygen Reduction Reaction Catalyst. *Adv. Mater.* **2013,** *25* (21), 2974-2979.
189. Li, C.; Nilson, T.; Cao, L.; Mueller, T., Predicting activation energies for vacancy-mediated diffusion in alloys using a transition-state cluster expansion. *arXiv:2009.12474 [physics.chem-ph]* **2020**.
190. Henkelman, G.; Uberuaga, B. P.; Jónsson, H., A climbing image nudged elastic band method for finding saddle points and minimum energy paths. *The Journal of Chemical Physics* **2000,** *113* (22), 9901-9904.
191. Henkelman, G.; Jónsson, H., Improved tangent estimate in the nudged elastic band method for finding minimum energy paths and saddle points. *The Journal of Chemical Physics* **2000,** *113* (22), 9978-9985.
192. Wu, Q.; He, B.; Song, T.; Gao, J.; Shi, S., Cluster expansion method and its application in computational materials science. *Computational Materials Science* **2016,** *125*, 243-254.
193. Lim, J. S.; Molinari, N.; Duanmu, K.; Sautet, P.; Kozinsky, B., Automated Detection and Characterization of Surface Restructuring Events in Bimetallic Catalysts. *J. Phys. Chem. C* **2019,** *123* (26), 16332-16344.
194. Tiwary, Y.; Fichthorn, K. A., Mechanisms of atomic diffusion on the flat, stepped, and faceted surfaces of Al(110). *Physical Review B* **2010,** *81* (19), 195421.

195. Montalenti, F.; Ferrando, R., Leapfrog Diffusion Mechanism for One-Dimensional Chains on Missing-Row Reconstructed Surfaces. *Phys. Rev. Lett.* **1999,** *82* (7), 1498-1501.
196. Zhang, Y.; Ling, C., A strategy to apply machine learning to small datasets in materials science. *npj Computational Materials* **2018,** *4* (1), 25.
197. Schulze, T. P., Efficient kinetic Monte Carlo simulation. *Journal of Computational Physics* **2008,** *227* (4), 2455-2462.
198. Serebrinsky, S. A., Physical time scale in kinetic Monte Carlo simulations of continuous-time Markov chains. *Physical Review E* **2011,** *83* (3), 037701.
199. Cao, L.; Mueller, T., Rational Design of Pt3Ni Surface Structures for the Oxygen Reduction Reaction. *J. Phys. Chem. C* **2015,** *119* (31), 17735-17747.
200. Wolpert, D. H., Stacked generalization. *Neural Networks* **1992,** *5* (2), 241-259.
201. Hartung, J.; Knapp, G.; Sinha, B. K., *Statistical meta-analysis with applications*. John Wiley & Sons: 2008.
202. Cui, C.; Gan, L.; Heggen, M.; Rudi, S.; Strasser, P., Compositional segregation in shaped Pt alloy nanoparticles and their structural behaviour during electrocatalysis. *Nature Materials* **2013,** *12* (8), 765-771.
203. Gorbatov, O. I.; Gornostyrev, Y. N.; Korzhavyi, P. A., Many-body mechanism of Guinier-Preston zones stabilization in Al–Cu alloys. *Scripta Mater.* **2017,** *138*, 130-133.
204. Whipple, D. T.; Kenis, P. J. A., Prospects of CO_2 Utilization via Direct Heterogeneous Electrochemical Reduction. *J. Phys. Chem. Lett.* **2010,** *1* (24), 3451-3458.
205. Olah, G. A.; Prakash, G. K. S.; Goeppert, A., Anthropogenic Chemical Carbon Cycle for a Sustainable Future. *J. Am. Chem. Soc.* **2011,** *133* (33), 12881-12898.
206. Chen, Y. H.; Li, C. W.; Kanan, M. W., Aqueous CO_2 Reduction at Very Low Overpotential on Oxide-Derived Au Nanoparticles. *J. Am. Chem. Soc.* **2012,** *134* (49), 19969-19972.
207. Feng, X. F.; Jiang, K. L.; Fan, S. S.; Kanan, M. W., Grain-Boundary-Dependent CO_2 Electroreduction Activity. *J. Am. Chem. Soc.* **2015,** *137* (14), 4606-4609.
208. Zhu, W.; Michalsky, R.; Metin, Ö.; Lv, H.; Guo, S.; Wright, C. J.; Sun, X.; Peterson, A. A.; Sun, S., Monodisperse Au Nanoparticles for Selective Electrocatalytic Reduction of CO2 to CO. *J. Am. Chem. Soc.* **2013,** *135* (45), 16833-16836.
209. Zhu, W.; Zhang, Y.-J.; Zhang, H.; Lv, H.; Li, Q.; Michalsky, R.; Peterson, A. A.; Sun, S., Active and Selective Conversion of CO2 to CO on Ultrathin Au Nanowires. *J. Am. Chem. Soc.* **2014,** *136* (46), 16132-16135.
210. Mariano, R. G.; McKelvey, K.; White, H. S.; Kanan, M. W., Selective increase in CO2 electroreduction activity at grain-boundary surface terminations. *Science* **2017,** *358* (6367), 1187.
211. Zhao, S.; Jin, R. X.; Jin, R. C., Opportunities and Challenges in CO_2 Reduction by Gold- and Silver-Based Electrocatalysts: From Bulk Metals to Nanoparticles and Atomically Precise Nanoclusters. *ACS Energy Lett.* **2018,** *3* (2), 452-462.
212. Mistry, H.; Reske, R.; Zeng, Z. H.; Zhao, Z. J.; Greeley, J.; Strasser, P.; Roldan Cuenya, B., Exceptional Size-Dependent Activity Enhancement in the Electroreduction of CO_2 over Au Nanoparticles. *J. Am. Chem. Soc.* **2014,** *136* (47), 16473-16476.
213. Verma, S.; Hamasaki, Y.; Kim, C.; Huang, W. X.; Lu, S.; Jhong, H. R. M.; Gewirth, A. A.; Fujigaya, T.; Nakashima, N.; Kenis, P. J. A., Insights into the Low Overpotential Electroreduction of CO_2 to CO on a Supported Gold Catalyst in an Alkaline Flow Electrolyzer. *ACS Energy Lett.* **2018,** *3* (1), 193-198.

214. Verma, S.; Kim, B.; Jhong, H.; Ma, S. C.; Kenis, P. J. A., A Gross-Margin Model for Defining Technoeconomic Benchmarks in the Electroreduction of CO_2. *Chemsuschem* **2016,** *9* (15), 1972-1979.
215. Jouny, M.; Luc, W.; Jiao, F., General Techno-Economic Analysis of CO_2 Electrolysis Systems. *Ind. Eng. Chem.* **2018,** *57* (6), 2165-2177.
216. Bushuyev, O. S.; De Luna, P.; Dinh, C. T.; Tao, L.; Saur, G.; van de Lagemaat, J.; Kelley, S. O.; Sargent, E. H., What Should We Make with CO_2 and How Can We Make It? *Joule* **2018,** *2* (5), 825-832.
217. Lee, H.-E.; Yang, K. D.; Yoon, S. M.; Ahn, H.-Y.; Lee, Y. Y.; Chang, H.; Jeong, D. H.; Lee, Y.-S.; Kim, M. Y.; Nam, K. T., Concave Rhombic Dodecahedral Au Nanocatalyst with Multiple High-Index Facets for CO_2 Reduction. *ACS Nano* **2015,** *9* (8), 8384-8393.
218. Mezzavilla, S.; Horch, S.; Stephens, I. E. L.; Seger, B.; Chorkendorff, I., Structure Sensitivity in the Electrocatalytic Reduction of CO_2 with Gold Catalysts. *Angew. Chem. Int. Ed.* **2019,** *58* (12), 3774-3778.
219. Wuttig, A.; Yaguchi, M.; Motobayashi, K.; Osawa, M.; Surendranath, Y., Inhibited proton transfer enhances Au-catalyzed CO2-to-fuels selectivity. *Proceedings of the National Academy of Sciences* **2016,** *113* (32), E4585.
220. Zhang, B. A.; Ozel, T.; Elias, J. S.; Costentin, C.; Nocera, D. G., Interplay of Homogeneous Reactions, Mass Transport, and Kinetics in Determining Selectivity of the Reduction of CO2 on Gold Electrodes. *ACS Central Science* **2019,** *5* (6), 1097-1105.
221. Dunwell, M.; Luc, W.; Yan, Y.; Jiao, F.; Xu, B., Understanding Surface-Mediated Electrochemical Reactions: CO2 Reduction and Beyond. *ACS Catalysis* **2018**, 8121-8129.
222. Ringe, S.; Morales-Guio, C. G.; Chen, L. D.; Fields, M.; Jaramillo, T. F.; Hahn, C.; Chan, K., Double layer charging driven carbon dioxide adsorption limits the rate of electrochemical carbon dioxide reduction on Gold. *Nature Communications* **2020,** *11* (1), 33.
223. Fan, Z.; Zhang, H., Crystal Phase-Controlled Synthesis, Properties and Applications of Noble Metal Nanomaterials. *Chem. Soc. Rev.* **2016,** *45*, 63.
224. Fan, Z. X.; Zhang, H., Template Synthesis of Noble Metal Nanocrystals with Unusual Crystal Structures and Their Catalytic Applications. *Acc. Chem. Res.* **2016,** *49*, 2841.
225. Cheng, H.; Yang, N.; Lu, Q.; Zhang, Z.; Zhang, H., Syntheses and Properties of Metal Nanomaterials with Novel Crystal Phases. *Adv. Mater.* **2018,** *30* (26), 1707189.
226. Wang, Y.; Li, C.; Fan, Z.; Chen, Y.; Li, X.; Cao, L.; Wang, L.; Su, D.; Zhang, H.; Mueller, T.; Wang, C., Undercoordinated Active Sites on 4H Gold Nanostructures for CO2 Reduction. *Nano Lett.* **2020**.
227. Perdew, J. P.; Ruzsinszky, A.; Csonka, G. I.; Vydrov, O. A.; Scuseria, G. E.; Constantin, L. A.; Zhou, X.; Burke, K., Restoring the Density-Gradient Expansion for Exchange in Solids and Surfaces. *Phys. Rev. Lett.* **2008,** *100* (13), 136406.
228. Grimme, S.; Antony, J.; Ehrlich, S.; Krieg, H., A consistent and accurate ab initio parametrization of density functional dispersion correction (DFT-D) for the 94 elements H-Pu. *The Journal of Chemical Physics* **2010,** *132* (15), 154104.
229. Mathew, K.; Sundararaman, R.; Letchworth-Weaver, K.; Arias, T. A.; Hennig, R. G., Implicit solvation model for density-functional study of nanocrystal surfaces and reaction pathways. *The Journal of Chemical Physics* **2014,** *140* (8), 084106.

230. Fishman, M.; Zhuang, H. L.; Mathew, K.; Dirschka, W.; Hennig, R. G., Accuracy of exchange-correlation functionals and effect of solvation on the surface energy of copper. *Physical Review B* **2013,** *87* (24), 245402.
231. Kim, J.; Samano, E.; Koel, B. E., CO Adsorption and Reaction on Clean and Oxygen-Covered Au(211) Surfaces. *The Journal of Physical Chemistry B* **2006,** *110* (35), 17512-17517.
232. Leiva, E., Recent developments in the theory of metal upd. *Electrochimica Acta* **1996,** *41* (14), 2185-2206.
233. Weitzner, S. E.; Dabo, I., Voltage-dependent cluster expansion for electrified solid-liquid interfaces: Application to the electrochemical deposition of transition metals. *Physical Review B* **2017,** *96* (20), 205134.
234. Yu, Y.; Cui, F.; Sun, J.; Yang, P., Atomic Structure of Ultrathin Gold Nanowires. *Nano Lett.* **2016,** *16* (5), 3078-3084.
235. Fan, Z.; Bosman, M.; Huang, X.; Huang, D.; Yu, Y.; Ong, K. P.; Akimov, Y. A.; Wu, L.; Li, B.; Wu, J.; Huang, Y.; Liu, Q.; Eng Png, C.; Lip Gan, C.; Yang, P.; Zhang, H., Stabilization of 4H hexagonal phase in gold nanoribbons. *Nat. Commun.* **2015,** *6* (1), 7684.
236. Hernández, J.; Solla-Gullón, J.; Herrero, E., Gold nanoparticles synthesized in a water-in-oil microemulsion: electrochemical characterization and effect of the surface structure on the oxygen reduction reaction. *J. Electroanal. Chem.* **2004,** *574* (1), 185-196.
237. Herrero, E.; Buller, L. J.; Abruña, H. D., Underpotential Deposition at Single Crystal Surfaces of Au, Pt, Ag and Other Materials. *Chem. Rev.* **2001,** *101* (7), 1897-1930.
238. Federico, C. V.; I., M. J.; M., G. L. J.; Philippe, S.; David, L., Fast Prediction of Adsorption Properties for Platinum Nanocatalysts with Generalized Coordination Numbers. *Angew. Chem. Int. Ed.* **2014,** *53* (32), 8316-8319.
239. Calle-Vallejo, F.; Tymoczko, J.; Colic, V.; Vu, Q. H.; Pohl, M. D.; Morgenstern, K.; Loffreda, D.; Sautet, P.; Schuhmann, W.; Bandarenka, A. S., Finding optimal surface sites on heterogeneous catalysts by counting nearest neighbors. *Science* **2015,** *350* (6257), 185-189.
240. Li, H.; Li, Y.; Koper, M. T. M.; Calle-Vallejo, F., Bond-Making and Breaking between Carbon, Nitrogen, and Oxygen in Electrocatalysis. *J. Am. Chem. Soc.* **2014,** *136* (44), 15694-15701.
241. Calle-Vallejo, F.; Koper, M. T. M.; Bandarenka, A. S., Tailoring the catalytic activity of electrodes with monolayer amounts of foreign metals. *Chem. Soc. Rev.* **2013,** *42* (12), 5210-5230.
242. Kleis, J.; Greeley, J.; Romero, N. A.; Morozov, V. A.; Falsig, H.; Larsen, A. H.; Lu, J.; Mortensen, J. J.; Dułak, M.; Thygesen, K. S.; Nørskov, J. K.; Jacobsen, K. W., Finite Size Effects in Chemical Bonding: From Small Clusters to Solids. *Catal. Lett.* **2011,** *141* (8), 1067-1071.
243. Hansen, H. A.; Varley, J. B.; Peterson, A. A.; Nørskov, J. K., Understanding Trends in the Electrocatalytic Activity of Metals and Enzymes for CO2 Reduction to CO. *The Journal of Physical Chemistry Letters* **2013,** *4* (3), 388-392.
244. Cheng, T.; Huang, Y.; Xiao, H.; Goddard, W. A., Predicted Structures of the Active Sites Responsible for the Improved Reduction of Carbon Dioxide by Gold Nanoparticles. *The Journal of Physical Chemistry Letters* **2017,** *8* (14), 3317-3320.

245. Durand, W. J.; Peterson, A. A.; Studt, F.; Abild-Pedersen, F.; Nørskov, J. K., Structure effects on the energetics of the electrochemical reduction of CO2 by copper surfaces. *Surf. Sci.* **2011,** *605* (15), 1354-1359.
246. Liu, X.; Xiao, J.; Peng, H.; Hong, X.; Chan, K.; Nørskov, J. K., Understanding trends in electrochemical carbon dioxide reduction rates. *Nature Communications* **2017,** *8*, 15438.
247. Shi, C.; Chan, K.; Yoo, J. S.; Nørskov, J. K., Barriers of Electrochemical CO2 Reduction on Transition Metals. *Organic Process Research & Development* **2016,** *20* (8), 1424-1430.
248. Chernyshova, I. V.; Somasundaran, P.; Ponnurangam, S., On the origin of the elusive first intermediate of CO2 electroreduction. *Proceedings of the National Academy of Sciences* **2018,** *115* (40), E9261.
249. Liu, C.; Cundari, T. R.; Wilson, A. K., CO2 Reduction on Transition Metal (Fe, Co, Ni, and Cu) Surfaces: In Comparison with Homogeneous Catalysis. *J. Phys. Chem. C* **2012,** *116* (9), 5681-5688.
250. Hagman, B.; Posada-Borbón, A.; Schaefer, A.; Shipilin, M.; Zhang, C.; Merte, L. R.; Hellman, A.; Lundgren, E.; Grönbeck, H.; Gustafson, J., Steps Control the Dissociation of CO2 on Cu(100). *J. Am. Chem. Soc.* **2018,** *140* (40), 12974-12979.
251. Back, S.; Yeom, M. S.; Jung, Y., Understanding the Effects of Au Morphology on CO2 Electrocatalysis. *J. Phys. Chem. C* **2018,** *122* (8), 4274-4280.
252. Kirubakaran, A.; Jain, S.; Nema, R. K., A review on fuel cell technologies and power electronic interface. *Renewable and Sustainable Energy Reviews* **2009,** *13* (9), 2430-2440.
253. Marković, N. M.; Grgur, B. N.; Ross, P. N., Temperature-dependent hydrogen electrochemistry on platinum low-index single-crystal surfaces in acid solutions. *The Journal of Physical Chemistry B* **1997,** *101* (27), 5405-5413.
254. Nørskov, J. K.; Bligaard, T.; Logadottir, A.; Kitchin, J. R.; Chen, J. G.; Pandelov, S.; Stimming, U., Trends in the exchange current for hydrogen evolution. *J. Electrochem. Soc.* **2005,** *152* (3), J23-J26.
255. Kibsgaard, J.; Tsai, C.; Chan, K.; Benck, J. D.; Norskov, J. K.; Abild-Pedersen, F.; Jaramillo, T. F., Designing an improved transition metal phosphide catalyst for hydrogen evolution using experimental and theoretical trends. *Energy & Environmental Science* **2015,** *8* (10), 3022-3029.
256. Popczun, E. J.; Read, C. G.; Roske, C. W.; Lewis, N. S.; Schaak, R. E., Highly active electrocatalysis of the hydrogen evolution reaction by cobalt phosphide nanoparticles. *Angew. Chem.* **2014,** *126* (21), 5531-5534.
257. Popczun, E. J.; McKone, J. R.; Read, C. G.; Biacchi, A. J.; Wiltrout, A. M.; Lewis, N. S.; Schaak, R. E., Nanostructured nickel phosphide as an electrocatalyst for the hydrogen evolution reaction. *J. Am. Chem. Soc* **2013,** *135* (25), 9267-9270.
258. Zheng, Y.; Jiao, Y.; Jaroniec, M.; Qiao, S. Z., Advancing the Electrochemistry of the Hydrogen-Evolution Reaction through Combining Experiment and Theory. *Angew. Chem. Int. Ed.* **2015,** *54* (1), 52-65.
259. Hansen, M. H.; Stern, L.-A.; Feng, L.; Rossmeisl, J.; Hu, X., Widely available active sites on Ni 2 P for electrochemical hydrogen evolution–insights from first principles calculations. *PCCP* **2015,** *17* (16), 10823-10829.

260. Laursen, A. B.; Patraju, K. R.; Whitaker, M. J.; Retuerto, M.; Sarkar, T.; Yao, N.; Ramanujachary, K. V.; Greenblatt, M.; Dismukes, G. C., Nanocrystalline Ni5P4: a hydrogen evolution electrocatalyst of exceptional efficiency in both alkaline and acidic media. *Energy & Environmental Science* **2015,** *8* (3), 1027-1034.
261. Yang, X.; Lu, A.-Y.; Zhu, Y.; Min, S.; Hedhili, M. N.; Han, Y.; Huang, K.-W.; Li, L.-J., Rugae-like FeP nanocrystal assembly on a carbon cloth: an exceptionally efficient and stable cathode for hydrogen evolution. *Nanoscale* **2015,** *7* (25), 10974-10981.
262. Tian, J.; Liu, Q.; Liang, Y.; Xing, Z.; Asiri, A. M.; Sun, X., FeP Nanoparticles Film Grown on Carbon Cloth: An Ultrahighly Active 3D Hydrogen Evolution Cathode in Both Acidic and Neutral Solutions. *ACS Applied Materials & Interfaces* **2014,** *6* (23), 20579-20584.
263. Parsons, R., The rate of electrolytic hydrogen evolution and the heat of adsorption of hydrogen. *Transactions of the Faraday Society* **1958,** *54* (0), 1053-1063.
264. Greeley, J.; Jaramillo, T. F.; Bonde, J.; Chorkendorff, I.; Norskov, J. K., Computational high-throughput screening of electrocatalytic materials for hydrogen evolution. *Nat Mater* **2006,** *5* (11), 909-913.
265. Laursen, A. B.; Wexler, R. B.; Whitaker, M. J.; Izett, E. J.; Calvinho, K. U. D.; Hwang, S.; Rucker, R.; Wang, H.; Li, J.; Garfunkel, E.; Greenblatt, M.; Rappe, A. M.; Dismukes, G. C., Climbing the Volcano of Electrocatalytic Activity while Avoiding Catalyst Corrosion: Ni3P, a Hydrogen Evolution Electrocatalyst Stable in Both Acid and Alkali. *ACS Catal.* **2018,** *8* (5), 4408-4419.
266. Wexler, R. B.; Martirez, J. M. P.; Rappe, A. M., Active Role of Phosphorus in the Hydrogen Evolving Activity of Nickel Phosphide (0001) Surfaces. *ACS Catal.* **2017,** *7* (11), 7718-7725.
267. Tang, C.; Gan, L.; Zhang, R.; Lu, W.; Jiang, X.; Asiri, A. M.; Sun, X.; Wang, J.; Chen, L., Ternary FexCo1–xP Nanowire Array as a Robust Hydrogen Evolution Reaction Electrocatalyst with Pt-like Activity: Experimental and Theoretical Insight. *Nano Lett.* **2016,** *16* (10), 6617-6621.
268. Skúlason, E.; Tripkovic, V.; Björketun, M. E.; Gudmundsdottir, S.; Karlberg, G.; Rossmeisl, J.; Bligaard, T.; Jónsson, H.; Nørskov, J. K., Modeling the electrochemical hydrogen oxidation and evolution reactions on the basis of density functional theory calculations. *J. Phys. Chem. C* **2010,** *114* (42), 18182-18197.
269. Tsai, C.; Chan, K.; Nørskov, J. K.; Abild-Pedersen, F., Rational design of MoS 2 catalysts: tuning the structure and activity via transition metal doping. *Catalysis Science & Technology* **2015,** *5* (1), 246-253.
270. Shao, Y.; Shi, X.; Pan, H., Electronic, Magnetic, and Catalytic Properties of Thermodynamically Stable Two-Dimensional Transition-Metal Phosphides. *Chem. Mater.* **2017,** *29* (20), 8892-8900.
271. Anantharaj, S.; Ede, S. R.; Sakthikumar, K.; Karthick, K.; Mishra, S.; Kundu, S., Recent Trends and Perspectives in Electrochemical Water Splitting with an Emphasis on Sulfide, Selenide, and Phosphide Catalysts of Fe, Co, and Ni: A Review. *ACS Catal.* **2016,** *6* (12), 8069-8097.
272. Li, C.; Gao, H.; Wan, W.; Mueller, T., Mechanisms for hydrogen evolution on transition metal phosphide catalysts and a comparison to Pt(111). *PCCP* **2019,** *21* (44), 24489-24498.

273. Wu, C.; Schmidt, D. J.; Wolverton, C.; Schneider, W. F., Accurate coverage-dependence incorporated into first-principles kinetic models: Catalytic NO oxidation on Pt (111). *J. Catal.* **2012,** *286*, 88-94.
274. Gómez, R.; Orts, J. M.; Álvarez-Ruiz, B.; Feliu, J. M., Effect of Temperature on Hydrogen Adsorption on Pt(111), Pt(110), and Pt(100) Electrodes in 0.1 M HClO4. *The Journal of Physical Chemistry B* **2004,** *108* (1), 228-238.
275. Atkins, P. W., *Physical chemistry*. Oxford University Press: Oxford; Melbourne; Tokyo, 1998.
276. Rossmeisl, J.; Skúlason, E.; Björketun, M. E.; Tripkovic, V.; Nørskov, J. K., Modeling the electrified solid–liquid interface. *Chem. Phys. Lett.* **2008,** *466* (1), 68-71.
277. Trasatti, S., The absolute electrode potential: an explanatory note (Recommendations 1986). In *Pure Appl. Chem.*, 1986; Vol. 58, p 955.
278. Randles, J. E. B., The real hydration energies of ions. *Transactions of the Faraday Society* **1956,** *52* (0), 1573-1581.
279. Chan, K.; Nørskov, J. K., Electrochemical Barriers Made Simple. *The Journal of Physical Chemistry Letters* **2015,** *6* (14), 2663-2668.
280. Bronsted, J. N., Acid and Basic Catalysis. *Chem. Rev.* **1928,** *5* (3), 231-338.
281. Evans, M. G.; Polanyi, M., Inertia and driving force of chemical reactions. *Transactions of the Faraday Society* **1938,** *34* (0), 11-24.
282. Nørskov, J. K.; Bligaard, T.; Logadottir, A.; Bahn, S.; Hansen, L. B.; Bollinger, M.; Bengaard, H.; Hammer, B.; Sljivancanin, Z.; Mavrikakis, M.; Xu, Y.; Dahl, S.; Jacobsen, C. J. H., Universality in Heterogeneous Catalysis. *J. Catal.* **2002,** *209* (2), 275-278.
283. Skulason, E.; Karlberg, G. S.; Rossmeisl, J.; Bligaard, T.; Greeley, J.; Jonsson, H.; Norskov, J. K., Density functional theory calculations for the hydrogen evolution reaction in an electrochemical double layer on the Pt(111) electrode. *PCCP* **2007,** *9* (25), 3241-3250.
284. Marković, N. M.; Schmidt, T. J.; Grgur, B. N.; Gasteiger, H. A.; Behm, R. J.; Ross, P. N., Effect of Temperature on Surface Processes at the Pt(111)−Liquid Interface: Hydrogen Adsorption, Oxide Formation, and CO Oxidation. *The Journal of Physical Chemistry B* **1999,** *103* (40), 8568-8577.
285. Conway, B. E.; Angerstein-Kozlowska, H.; Dhar, H. P., On selection of standard states in adsorption isotherms. *Electrochim. Acta* **1974,** *19* (8), 455-460.
286. Marković, N. M.; Ross, P. N., Surface science studies of model fuel cell electrocatalysts. *Surf. Sci. Rep.* **2002,** *45* (4), 117-229.
287. Ramaker, D. E.; Roth, C., Nature of the Intermediate Binding Sites in Hydrogen Oxidation/Evolution over Pt in Alkaline and Acidic Media. *ChemElectroChem* **2015,** *2* (10), 1582-1594.
288. Aurenhammer, F., Voronoi diagrams—a survey of a fundamental geometric data structure. *ACM Comput. Surv.* **1991,** *23* (3), 345-405.
289. Magdić Košiček, K.; Kvastek, K.; Horvat-Radošević, V., Hydrogen evolution on Pt and polyaniline modified Pt electrodes—a comparative electrochemical impedance spectroscopy study. *J. Solid State Electrochem.* **2016,** *20* (11), 3003-3013.
290. Lindgren, P.; Kastlunger, G.; Peterson, A. A., A Challenge to the G ∼ 0 Interpretation of Hydrogen Evolution. *ACS Catal.* **2020,** *10* (1), 121-128.

291. Shinagawa, T.; Garcia-Esparza, A. T.; Takanabe, K., Insight on Tafel slopes from a microkinetic analysis of aqueous electrocatalysis for energy conversion. *Scientific Reports* **2015,** *5*, 13801.
292. Kahyarian, A.; Brown, B.; Nesic, S., Mechanism of the Hydrogen Evolution Reaction in Mildly Acidic Environments on Gold. *J. Electrochem. Soc.* **2017,** *164* (6), H365-H374.
293. Subramanian, N. P.; Greszler, T. A.; Zhang, J.; Gu, W.; Makharia, R., Pt-Oxide Coverage-Dependent Oxygen Reduction Reaction (ORR) Kinetics. *J. Electrochem. Soc.* **2012,** *159* (5), B531-B540.
294. Yang, L.; Qi, H.; Zhang, C.; Sun, X., An efficient bifunctional electrocatalyst for water splitting based on cobalt phosphide. *Nanotechnology* **2016,** *27* (23), 23LT01.
295. Schipper, D. E.; Zhao, Z.; Thirumalai, H.; Leitner, A. P.; Donaldson, S. L.; Kumar, A.; Qin, F.; Wang, Z.; Grabow, L. C.; Bao, J.; Whitmire, K. H., Effects of Catalyst Phase on the Hydrogen Evolution Reaction of Water Splitting: Preparation of Phase-Pure Films of FeP, Fe2P, and Fe3P and Their Relative Catalytic Activities. *Chem. Mater.* **2018,** *30* (10), 3588-3598.
296. Hu, H.; Zhang, Q.; Luo, F.; Guo, L.; Qu, K.; Yang, Z.; Xiao, S.; Xu, Z.; Cai, W.; Cheng, H., Fe@Fe2P Core-Shell Nanorods Encapsulated in Nitrogen Doped Carbon Nanotubes as Robust and Stable Electrocatalyst Toward Hydrogen Evolution. *ChemElectroChem* **2019,** *6* (5), 1413-1418.
297. Yang, J.; Ouyang, Y.; Zhang, H.; Xu, H.; Zhang, Y.; Wang, Y., Novel Fe2P/graphitized carbon yolk/shell octahedra for high-efficiency hydrogen production and lithium storage. *Journal of Materials Chemistry A* **2016,** *4* (25), 9923-9930.
298. Liang, Y.; Liu, Q.; Asiri, A. M.; Sun, X.; Luo, Y., Self-Supported FeP Nanorod Arrays: A Cost-Effective 3D Hydrogen Evolution Cathode with High Catalytic Activity. *ACS Catal.* **2014,** *4* (11), 4065-4069.
299. Zhang, Y.; Gao, L.; Hensen, E. J. M.; Hofmann, J. P., Evaluating the Stability of Co2P Electrocatalysts in the Hydrogen Evolution Reaction for Both Acidic and Alkaline Electrolytes. *ACS Energy Letters* **2018,** *3* (6), 1360-1365.
300. Callejas, J. F.; Read, C. G.; Popczun, E. J.; McEnaney, J. M.; Schaak, R. E., Nanostructured Co2P Electrocatalyst for the Hydrogen Evolution Reaction and Direct Comparison with Morphologically Equivalent CoP. *Chem. Mater.* **2015,** *27* (10), 3769-3774.
301. Pan, Y.; Lin, Y.; Chen, Y.; Liu, Y.; Liu, C., Cobalt phosphide-based electrocatalysts: synthesis and phase catalytic activity comparison for hydrogen evolution. *Journal of Materials Chemistry A* **2016,** *4* (13), 4745-4754.
302. Zhu, Y.-P.; Liu, Y.-P.; Ren, T.-Z.; Yuan, Z.-Y., Self-Supported Cobalt Phosphide Mesoporous Nanorod Arrays: A Flexible and Bifunctional Electrode for Highly Active Electrocatalytic Water Reduction and Oxidation. *Adv. Funct. Mater.* **2015,** *25* (47), 7337-7347.
303. Ledezma-Yanez, I.; Wallace, W. D. Z.; Sebastián-Pascual, P.; Climent, V.; Feliu, J. M.; Koper, M. T. M., Interfacial water reorganization as a pH-dependent descriptor of the hydrogen evolution rate on platinum electrodes. *Nature Energy* **2017,** *2* (4), 17031.
304. Han, A.; Jin, S.; Chen, H.; Ji, H.; Sun, Z.; Du, P., A robust hydrogen evolution catalyst based on crystalline nickel phosphide nanoflakes on three-dimensional

graphene/nickel foam: high performance for electrocatalytic hydrogen production from pH 0–14. *Journal of Materials Chemistry A* **2015,** *3* (5), 1941-1946.
305. Jiang, P.; Liu, Q.; Sun, X., NiP2 nanosheet arrays supported on carbon cloth: an efficient 3D hydrogen evolution cathode in both acidic and alkaline solutions. *Nanoscale* **2014,** *6* (22), 13440-13445.
306. Abghoui, Y.; Skúlason, E., Hydrogen Evolution Reaction Catalyzed by Transition-Metal Nitrides. *J. Phys. Chem. C* **2017,** *121* (43), 24036-24045.
307. Kastlunger, G.; Lindgren, P.; Peterson, A. A., Controlled-Potential Simulation of Elementary Electrochemical Reactions: Proton Discharge on Metal Surfaces. *J. Phys. Chem. C* **2018,** *122* (24), 12771-12781.
308. Limmer, D. T.; Willard, A. P.; Madden, P.; Chandler, D., Hydration of metal surfaces can be dynamically heterogeneous and hydrophobic. *Proceedings of the National Academy of Sciences* **2013,** *110* (11), 4200-4205.
309. Hansen, H. A.; Viswanathan, V.; Nørskov, J. K., Unifying Kinetic and Thermodynamic Analysis of 2 e– and 4 e– Reduction of Oxygen on Metal Surfaces. *J. Phys. Chem. C* **2014,** *118* (13), 6706-6718.
310. Dybeck, E. C.; Plaisance, C. P.; Neurock, M., Generalized Temporal Acceleration Scheme for Kinetic Monte Carlo Simulations of Surface Catalytic Processes by Scaling the Rates of Fast Reactions. *Journal of Chemical Theory and Computation* **2017,** *13* (4), 1525-1538.
311. Conway, B. E.; Barber, J.; Morin, S., Comparative evaluation of surface structure specificity of kinetics of UPD and OPD of H at single-crystal Pt electrodes. *Electrochim. Acta* **1998,** *44* (6), 1109-1125.
312. Kobayashi, S.; Tryk, D. A.; Uchida, H., Enhancement of hydrogen evolution activity on Pt-skin/Pt3Co [(111), (100), and (110)] single crystal electrodes. *Electrochem. Commun.* **2020,** *110*, 106615.
313. van der Niet, M. J. T. C.; Garcia-Araez, N.; Hernández, J.; Feliu, J. M.; Koper, M. T. M., Water dissociation on well-defined platinum surfaces: The electrochemical perspective. *Catal. Today* **2013,** *202*, 105-113.
314. McCrum, I. T.; Chen, X.; Schwarz, K. A.; Janik, M. J.; Koper, M. T. M., Effect of Step Density and Orientation on the Apparent pH Dependence of Hydrogen and Hydroxide Adsorption on Stepped Platinum Surfaces. *J. Phys. Chem. C* **2018,** *122* (29), 16756-16764.
315. Kristoffersen, H. H.; Vegge, T.; Hansen, H. A., OH formation and H2 adsorption at the liquid water–Pt(111) interface. *Chemical Science* **2018,** *9* (34), 6912-6921.
316. Ryu, J.; Surendranath, Y., Tracking Electrical Fields at the Pt/H2O Interface during Hydrogen Catalysis. *J. Am. Chem. Soc.* **2019,** *141* (39), 15524-15531.
317. Van den Bossche, M.; Skúlason, E.; Rose-Petruck, C.; Jónsson, H., Assessment of Constant-Potential Implicit Solvation Calculations of Electrochemical Energy Barriers for H2 Evolution on Pt. *J. Phys. Chem. C* **2019,** *123* (7), 4116-4124.
318. He, Z.-D.; Chen, Y.-X.; Juarez, F.; Santos, E.; Schmickler, W., An Unusual Exchange Mechanism in the Tafel Reaction on Pt(110)-(1×1) Surfaces. *ChemElectroChem* **2019,** *6* (13), 3279-3284.
319. Tidswell, I. M.; Marković, N. M.; Ross, P. N., Potential dependent surface relaxation of the Pt(001)/electrolyte interface. *Phys. Rev. Lett.* **1993,** *71* (10), 1601-1604.

Vita

Chenyang Li was born in October 1992 in Shijiazhuang, China. In 2015 he received his B.S. degrees from The Pennsylvania State University (*cum laude*) and Harbin Institute of Technology. In the same year he joined the Mueller group at The Johns Hopkins University. Under the guidance of Professor Tim Mueller, he has implemented the cluster expansion method with a machine learning approach, to further the understanding structure-property relationships in various material systems with a focus on electrocatalysts. He has first- and co-first authored works published or under review in J. Phys. Chem. C, Nano Lett., Phys. Chem. Chem. Phys., Phys. Rev. Mater., and other publications in ACS Catal., ACS Nano, J. Am. Chem. Soc., J. Chem. Inf. Model., Nat. Nanotechnol., and RSC Adv.